The Journal of Applied Research on Science and Technology (JARST) is an international open-access journal dedicated to disseminating high-quality scientific and technological research. It provides a platform for academics, professionals, and industrial practitioners to exchange knowledge, promote innovation, and strengthen academic and research collaborations at both national and international levels. All submissions must be original, unpublished, and not under consideration elsewhere. The authors bear full responsibility for the accuracy, originality, and integrity of their work.

Aims and Scope

The Journal of Applied Research on Science and Technology (JARST) aims to disseminate high-quality research and innovative ideas in science and technology, fostering academic and industrial collaboration at both national and international levels.

The scope of the journal covers General Engineering, Materials Science, Agricultural and Biological Sciences, Computer Science, and Mathematics, with particular emphasis on research that integrates fundamental understanding with practical applications.

JARST publishes original research and review articles that contribute to scientific advancement and sustainable development. All accepted articles are published online immediately and freely accessible worldwide without restriction.

Review Process

1. Evaluation by the Editor-in-Chief

The Editor-in-Chief will see whether the topic and theme of the article are appropriate and congruent with the stipulated objectives and format of the Journal. Plagiarism and benefits relating to theory and business contribution will also be investigated. The submitted paper may be returned to the author for preliminary revising or, if the aforesaid criteria are not met, rejected.

2. Evaluation by Review

All submitted manuscripts must be reviewed by at least two expert reviewers in the related fields. Reviewers will evaluate the quality of submitted article for publication via the double-blinded review system.

3. Evaluates the Reviews

The Editor-in-Chief make decision for article publication based on the external readers' evaluation. The said decision is either accepting the article for publication, rejecting it, or resending it back to the author for further elaborating revision.

Period of Issued Journal

The Journal of Applied Research on Science and Technology (JARST) will be 3 issues/year, as follows:

1st issue: January - April
2nd issue: May - August
3rd issue: September - December

Advisory Board

Editorial Note

The Journal of Applied Research on Science and Technology (JARST) is an academic journal published by the Institute of Research and Development, Rajamangala University of Technology Thanyaburi (RMUTT). The journal aims to disseminate high-quality research and innovative ideas in the fields of General Engineering, Materials Science, Agricultural and Biological Sciences, Computer Science, and Mathematics, serving as a platform for researchers, academics, faculty members, and students at both national and international levels.

This issue presents ten research articles encompassing a diverse range of topics, such as The study of the impact of water channel obstructions in the lower Mun River on flooding, Physicochemical, textural, and antioxidant properties of Pandan Leaf Extract (PLE)-fortified gummy jelly, Analysis and improvement of PCB manufacturing efficiency using discrete-event simulation: An electrical industry use case, Prediction of the fatigue life of elevator wire rope using the Grey model GM (1,1), The relationship between compressive strength and expansion of alkali–silica reaction and/or delayed ettringite formation with the use of fly ash, Sustainable composite foam development: Crosslinked tapioca starch with corn husk sheet reinforcement and chitosan biocoating, Leveraging blockchain for enhancing electronic data interoperability in Thailand's port community system: Barriers and strategic enablers, Analysis of plowing patterns and their effect on the efficiency of land preparation following rice harvest, Evaluation of cylinder-shaped solar dryers on natural convection heat transfer, and A unified adaptive pure pursuit speed controller with EKF sensor fusion for real-world Ackermann mobile robots. These articles collectively contribute to the dissemination of knowledge across the physical and life sciences, providing valuable insights for future applications and developments.

Lastly, the editorial team extends its sincere appreciation to all contributors, reviewers, and supporters whose efforts have made this publication possible. We look forward to your continued cooperation and support in advancing the mission of JARST in the years to come.

Editorial Team

Contents

The Study of the impact of water channel obstructions in the lower Mun River on flooding

Supaporn Thongtem[1], Watchara Ongchotiyakul[2] and Chaiyapong Thepprasit[1*]

[1]Department of Irrigation Engineering, Faculty of Engineering at Kamphaeng Saen, Kasetsart University Kamphaeng Saen Campus, Nakhon Pathom 73140, THAILAND

[2]Paragon Engineering Consultants Co., LTD., Bangkok 10230, THAILAND

*Corresponding author: plase4401@hotmail.com

ABSTRACT

In 2022, Ubon Ratchathani Province experienced severe flooding that caused extensive damage to local communities. Local public opinion attributed the severity of this event to flow obstructions in the Mun River, particularly Kaeng Saphue and the Pak Mun Dam. These structures have raised concerns regarding their potential impacts on flood hydraulics. To explore this idea, this study will look at how these barriers affect flooding downstream using the HEC-RAS 2D hydrodynamic model. The simulation domain covers the river's reaches from the confluence of the Chi and Mun Rivers to the point where the Mun River flows into the Mekong River. The 2022 flood hydrograph was used to simulate flood extent and water levels under scenarios with and without the obstructions, including four different cases. Model calibration and validation were performed using data from 2019 and 2022, yielding high accuracy with R^2 values of 0.964 and 0.978, and RMSE values of 0.14 and 0.057, respectively. The study found that the water level at station M.7 was 116.50 m MSL in both the scenario with Kaeng Saphue and the Pak Mun Dam (OB.1) and the scenario without the Pak Mun Dam (OB.3), indicating no difference between these two cases. In contrast, removal of Kaeng Saphue (OB.2) reduced the water level to 116.15 m MSL, and removal of both obstructions (OB.4) further lowered it to 115.92 m MSL. These results indicate that Kaeng Saphue plays a significant role in raising water levels at station M.7, while the Pak Mun Dam has a secondary effect. When Kaeng Saphue is removed, the Pak Mun Dam becomes the primary obstruction contributing to upstream water level increases. This highlights the hydraulic influence of both natural and man-made obstructions in exacerbating flood impacts along the Mun River.

Keywords: HEC-RAS 2D model, Mun River flood 2022, Channel obstruction, Kaeng Saphue rapid, Pak Mun Dam

INTRODUCTION

Ubon Ratchathani Province experiences the problem of the Mun River overflowing its banks and flooding low-lying areas along it almost every year. This is due to the province's location at the confluence of the Mun and Chi Rivers, which are major river basins. Persistent heavy rainfall in these basins results in a substantial inflow of water into low-lying areas adjacent to the river, affecting residential communities, economic zones, and critical transportation routes. The Mun River, the only river that drains into the Mekong River, exacerbates this situation due to its limited drainage capacity.

The Mun River in the lower reaches of Phibun Mangsahan District is characterized by numerous islands and rapids throughout much of its length. In particular, Kaeng Saphue is a large natural rock rapid that forms a raised rocky and soil formation, almost completely obstructing the cross-section of the river and significantly impeding water flow. The average rock elevation of Kaeng Saphue is 106.25 m MSL, approximately 5.57 m above the normal water level. Water levels at Kaeng Saphue fluctuate irregularly with alternating heights. Due to this characteristic, Kaeng Saphue functions like a water retention dam, causing elevated water levels and reducing flow velocity. During the flood season, Kaeng Saphue acts as a major obstacle to water discharge, slowing the drainage of the Mun River into the Mekong River and worsening flooding in low-lying areas [1, 2], especially in Warin Chamrap and Ubon Ratchathani Municipalities.

Additionally, the Pak Mun Dam is located at Ban Huahew, Khong Chiam District, Ubon Ratchathani Province, approximately 6 kilometers upstream from the confluence of the Mun River and the Mekong River. This water diversion dam, constructed from compacted concrete, stands 17 meters high and extends 300 meters in length, featuring a crest 6 meters wide at an elevation of 111.0 m MSL. The dam's water drainage system consists of eight channels, each equipped with a radial gate measuring 22.5 meters wide and 14.75 meters high, allowing a maximum discharge capacity

of 18,500 cubic meters per second. The Pak Mun Dam provides numerous benefits, including stabilizing electricity production in the Northeast Region, supplying water for a 150-kilometer irrigation system upstream, supporting the Khong-Chi-Mun Project, establishing a fish breeding center to promote fisheries development, and serving as a tourist attraction [3]. However, the Pak Mun Dam is often cited as an obstacle to water drainage in the Mekong River. Since the dam was built to block the river's original width of approximately 300 meters, only 180 meters of the river can be drained through its eight gates, each 22.5 meters wide. This limited drainage capacity has been identified as a contributing factor to flooding in Ubon Ratchathani Province [4, 5].

The 2022 flood was triggered by a strong monsoon trough passing through the northeastern region and by Tropical Depression Noru, which entered Thailand near Khong Chiam District, Ubon Ratchathani Province, on the evening of September 28, 2022. At that time, it remained a depression. The storm then moved across Amnat Charoen, Yasothon, Roi Et, Maha Sarakham, and Khon Kaen Provinces, before weakening into a low-pressure cell over Chaiyaphum Province on the evening of September 29, 2022. The influence of the storm brought heavy to very heavy rainfall to the affected and surrounding areas, with particularly intense rainfall recorded in many parts of Ubon Ratchathani Province. This caused the water levels in the Mun River and its tributaries to rise continuously, leading to widespread overflow along nearly the entire river. At Station M.7 in Warin Chamrap District, the highest water level was recorded at 116.51 m MSL, with a peak discharge of 6,071 m³/s. As a result, regularly inundated low-lying areas experienced severe flooding, particularly in Warin Chamrap District, where flood levels rose above 4 meters. The flooding extended into the Ubon Ratchathani urban area, an important economic hub for both the province and the broader region located at the edge of the flooded zone. Many public utilities and almost all major access routes into Ubon Ratchathani City were severely flooded, including the Seri Prachathipatai 200 Years Bridge, the western bypass (Highway No. 231), and Highways No. 226 and 23. The only remaining main access route was the eastern bypass (Highway No. 231), which connects Warin Chamrap District to Ubon Ratchathani City [6, 7].

This research reviews relevant studies on flood volume analysis, flood simulation, and the impact of flow obstructions. Previous studies include the following: For instance, a study conducted in 2019 employed the InfoWorks-ICM model to simulate flooding in the Mun River in Ubon Ratchathani Province, with a focus on Mueang District. The study found that the river's roughness coefficient ranged from 0.03 to 0.065. The calibration results were accurate and reliable, making the model suitable for various applications [2].

Another study on flood prevention guidelines in Ubon Ratchathani Province, particularly in the lower Mun River Basin, reported that the river's roughness coefficient ranged from 0.028 to 0.045 [8]. Additionally, a study on the effects of flow obstructions on river flooding found that such obstructions can cause higher-than-normal flood levels and increased upstream inundation distances [9]. Several studies have explored approaches to mitigating flood problems in rivers and streams: A study on flood alleviation in small streams found that structural measures alone could not fully resolve flood issues. Researchers found that the most effective approach to reducing flood levels was to improve the cross-sections of bridges and culverts [10]. A working group investigating flood conditions and solutions in Mueang District, Ubon Ratchathani, proposed multiple drainage strategies for the Mun River. These included diverting floodwater through a natural canal to the Lam Dom Yai River, excavating a shortcut canal to bypass rapids, and improving islands and rapids in the downstream section. The results indicated that improving islands and rapids yielded the greatest reduction in flood levels-by approximately 162 to 169 cm [11]. A study examining the impact of flooding on built-up areas and infrastructure in Nan City found that raising land levels in flood-prone areas exacerbated flooding. Elevated land obstructed drainage, resulting in higher and longer-lasting floodwater levels [12]. The Marine Department conducted a detailed dredging design study for the Mun River, covering its course from Chok Chai District in Nakhon Ratchasima to its confluence with the Mekong River. Areas with environmental conservation restrictions were excluded. The study found that maximum flood levels could be reduced by an average of approximately 90 cm. In Mueang Ubon Ratchathani and Warin Chamrap Districts, flood levels decreased by 51–59 cm, while the greatest reduction-up to 99 cm-was recorded in Phibun Mangsahan District [13]. Another study assessed the impact of floodplain woodland on flood flows. Results showed that establishing woodland in floodplain areas significantly reduces downstream flood risk. Increased hydraulic roughness from vegetation slows flood velocities, raises upstream water levels, and enhances flood storage capacity. These combined effects help attenuate flood peaks and reduce flood intensity, offering a natural method for flood mitigation [14]. Lastly, a study in the Yellow River Basin examined the influence of multiple cross-river structures on flood discharge in mountain rivers. It found that removing weirs reduced maximum backwater levels by approximately 1.09 to 1.14 meters. Lowering weir crest elevations also decreased upstream water levels but did not substantially improve flood discharge capacity. Conversely, bridges, particularly those with piers, significantly affected flood dynamics. Submerged slab and arch bridges contributed to upstream backwater effects, with slab bridges having a more pronounced

impact. The number of bridge openings and pier thickness were found to be directly correlated with flow obstruction and the river's flood discharge capacity [15].

The objective of this research is to analyze the impact of flow obstructions in the lower Mun River, specifically Kaeng Saphue and the Pak Mun Dam, on flood levels in Ubon Ratchathani Province. This was accomplished using the HEC-RAS 2D model to simulate the 2022 flood event. The study compared scenarios with and without these obstructions to determine the extent to which they contribute to overflow flooding from the Mun River. A 2D model was selected for its ability to accurately capture inundation both within the river channel and in overbank areas. The model's accuracy was enhanced by updating the Digital Elevation Model (DEM) with newly surveyed cross-sectional data from 2020 and 2024, including detailed topographic information about Kaeng Saphue. Additionally, mesh sizes of 5 to 10 meters were applied in areas with significant elevation variation, such as dikes, flow paths, and uneven riverbeds, to improve simulation precision.
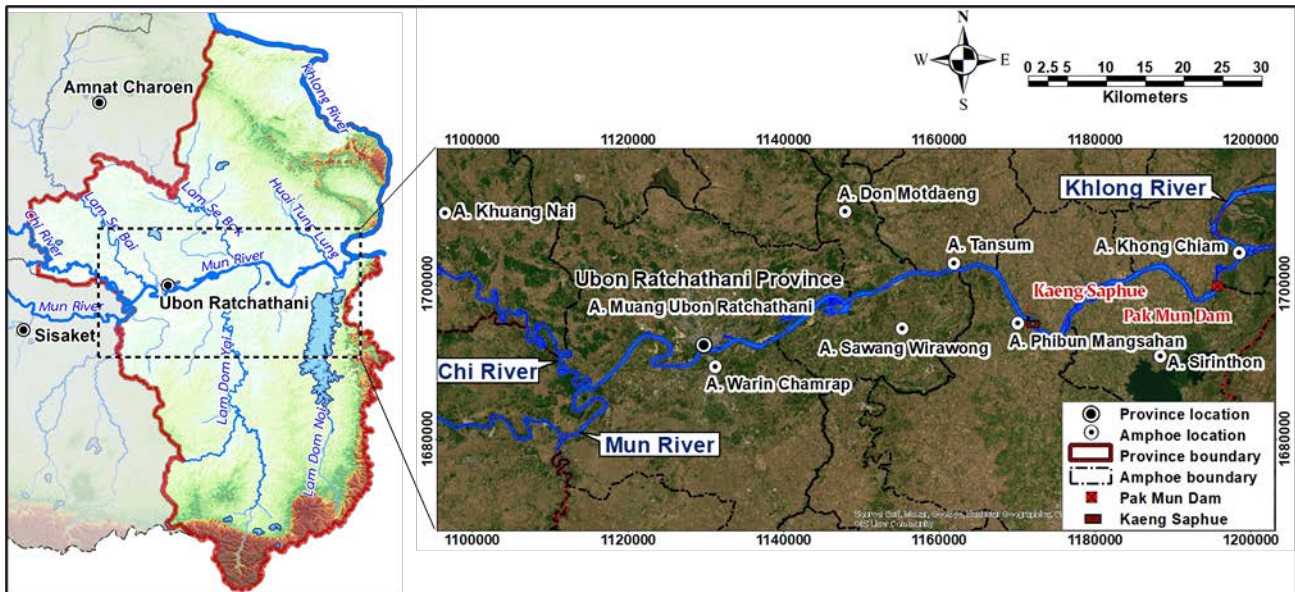
Figure 1 Study area along the Mun River in Ubon Ratchathani Province.

MATERIALS AND METHODS

The study area encompasses the Mun River and its adjacent floodplains in Ubon Ratchathani Province, located in the lower Mun River Basin. It extends from the confluence with the Chi River at UTM Zone 48N 469269 E, 1678548 N to its junction with the Mekong River at UTM Zone 47N 1199499 E, 1703776 N, covering a distance of approximately 116 kilometers. The area includes nine districts situated along and impacted by the Mun River: Khueang Nai, Mueang Ubon Ratchathani, Warin Chamrap, Sawang Wirawong, Don Mod Daeng, Tan Sum, Phibun Mangsahan, Sirindhorn, and Khong Chiam (Figure 1).

The steps for hydraulic analysis with the HEC-RAS 2D model involve gathering data, building the model, adjusting and checking the model, and using the model for case study analysis, as explained below.

1. Data collection

Data collection included gathering existing information from government agencies, such as river shapes, Digital Elevation Models (DEMs), weather and water data, land use details, and anything that blocks water flow (Table 1).

2. HEC-RAS model setup

This study utilized the HEC-RAS model version 6.4.1, developed by the Hydrologic Engineering Center (HEC) for the U.S. Army Corps of Engineers. The model analyzes flow in both one-dimensional (1D) and two-dimensional (2D) domains, supporting steady and unsteady flow calculations for water surface profiles, combined 1D and 2D hydrodynamics, and spatial mapping of parameters such as depth, water surface elevation, and velocity [16]. The 2D model simulates changing flow by using the shallow water (Saint-Venant) equations, which explain how mass is conserved and how momentum works in both the x and y directions, considering factors like gravity, pressure, friction, and forces from movement. It calculates water depth and velocity at each cell in a computational mesh, enabling accurate simulation over complex terrain.

HEC-RAS 2D uses a method that divides space into small sections, like squares, rectangles, or triangles, to solve equations on a grid that isn't perfectly regular. The model supports complex boundary conditions, internal structures, and terrain features, making it highly suitable for simulating floods in riverine channels and overbank areas [16, 17].

Table 1 Data inputs for the HEC-RAS 2D model.

Type of Data	Details	Source
River Network	Mun and Chi Rivers, including tributaries Huai Khayung, Huai Pub, Lam Dom Yai, Lam Dom Noi, Lam Sebai, Lam Sebok, Huai Tung Lung	Office of National Water Resources (ONWR), Royal Irrigation Department (RID)
Longitudinal Profiles	Longitudinal profiles of Mun and Chi Rivers	ONWR, RID
River Cross-Sections	Cross-sectional data of the Mun and Chi Rivers, including major tributaries and cross-sections near Pak Mun Dam	ONWR, RID, EGAT
Digital Elevation Model (DEM)	1:4,000 scale with 5×5 meter grid resolution representing off-river surface elevation	Land Development Department
Meteorological Data	Daily evaporation from Yasothon, Si Sa Ket, and Ubon Ratchathani weather stations and rainfall data	Meteorological Department
Hydrological Data	Runoff from gauging stations E.20A, M.182, M.170, M.176, M.157, M.32, M.69, 020139; water level and rating curves at M.7 and Sirindhorn Dam discharge data	RID, DWR, EGAT
Land Use Data	Used for selection of Manning's roughness coefficient (n)	Land Development Department
Flow Obstruction Data	2024 survey of Kaeng Saphue by RID; river cross-sections of Pak Mun Dam area (pre-construction and headworks)	RID, EGAT

$$\frac{\partial h}{\partial t} + \frac{\partial (hu)}{\partial x} + \frac{\partial (hv)}{\partial y} = q \tag{1}$$

$$\frac{\partial V}{\partial t} + (V.\nabla)V + f_c k \times V = -g\nabla z_s + \frac{1}{h}\nabla.(v_t h\nabla V) - \frac{\tau_b}{\rho R} + \frac{\tau_s}{\rho h} \tag{2}$$

Where,

t = time
h = water depth
u and v = velocity components in the and directions respectively
q = source/sink flux term (source > 0, sink < 0)
g = gravitational acceleration
z_s = water surface elevation
R = hydraulic radius
ρ = water density
f_c = Coriolis parameter
V = velocity vector

k = unit vector in the vertical direction
v_t = the eddy viscosity tensor
τ_b = bottom shear stress vector
τ_s = wind surface stress vector
∇ = gradient operator given by $\partial/\partial x$, $\partial/\partial y$

The HEC-RAS model set up for this research is divided into 5 main parts: data verification, terrain generation, 2D flow area generation, Manning's roughness coefficients assignment, boundary condition application, and flow obstruction sections import, as detailed below (Figure 2).
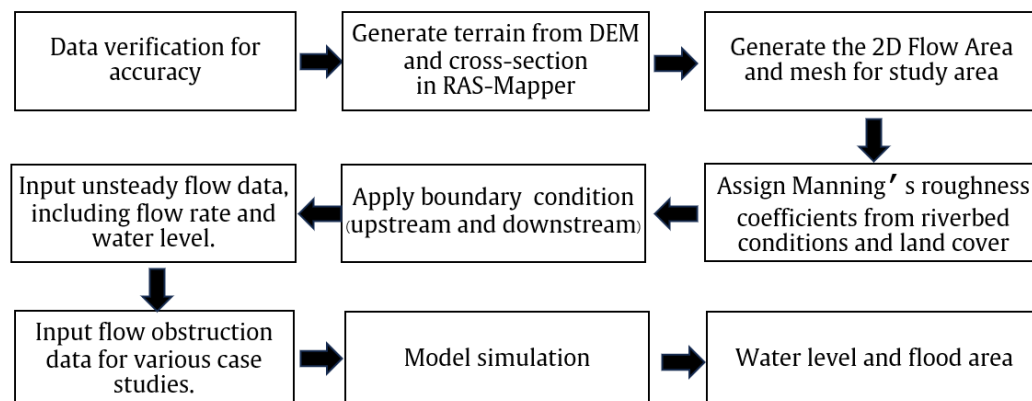
Figure 2 HEC-RAS 2D model development diagram.

2.1 The accuracy of rainfall data was verified using the Double Mass Curve method by plotting the cumulative rainfall of the index station against that of nearby stations. The consistency of streamflow data was assessed through cross-checking with data from adjacent stations. Additionally, the accuracy of the Digital Elevation Model (DEM) was verified by comparing elevation values with topographic survey data.

2. 2 Initial terrain data was derived from the Digital Elevation Model (DEM) provided by the Land Development Department. To improve the accuracy of the river areas, survey results of river cross-sections, gathered from the Office of National Water Resources and the Royal Irrigation Department, were used to make a more detailed DEM just for the river sections (Figure 3). This refined river DEM was then integrated with the original Land Development Department DEM to produce a new, adjusted DEM. This final DEM, featuring refined elevation values, served as the primary elevation data for the entire study area.
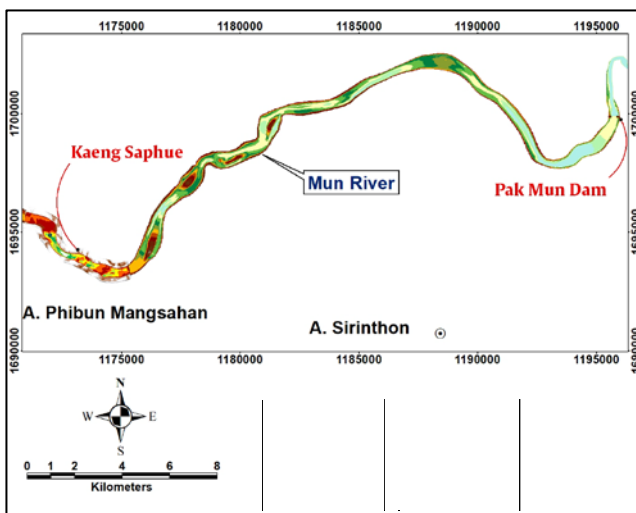
Figure 3 DEM from Kaeng Sapue to Pak Mun Dam.

2.3 The boundary conditions for flow simulation (2D Flow Areas) were defined to cover the study area, consistent with the research objectives and collected data. The mesh size within the 2D flow areas was determined based on the computational elements. While a smaller mesh yields more accurate results, it significantly increases computation time. Conversely, a larger mesh reduces calculation time but at the expense of accuracy. Thus, the strategy involved initiating with a coarser mesh and progressively refining its size to achieve greater detail in areas of interest or critical importance. For this research, mesh sizes ranged from 5x5 meters to 100x100 meters.

2.4 Accurate assignment of Manning's roughness coefficients (n) is crucial for precise calculations water surface elevation calculations. Initial determination of Manning's n values was based on experimental recommendations for various river conditions [17]. The Mun River is characterized by meanders, potholes, and areas with vegetation and rock covers. As a result, the recommended Manning's n values for these conditions typically range from 0.033 to 0.045 [18]. A review of previous research on similar river types has also found values in the broader range of 0.028 to 0.065 [2, 8]. For areas outside the river channel, the Manning's n values were determined based on recommended values according to land use types, as shown in Table 2.

2.5 The boundary conditions applied in the model consisted of upstream inflow and downstream outflow conditions. Upstream inflow conditions were based on water volume data gathered from seven measuring stations (E.20A, M.182, M.32, M.157, M.170, M.69, M.110) and flow data from Sirindhorn Dam. Additionally, the runoff from sub-basins within the 2D Flow Areas was incorporated as lateral inflow (side flow). The downstream condition utilized water level data from gauging station 020139, located on the Mekong River at Khong Chiam District.

Table 2 The roughness coefficient (Manning's n).

Type of channel	Minimum	Normal	Maximum
1. Main Channel			
a. clean, straight, full stage, no rifts or deep pools, more stones and weeds	0.030	0.035	0.040
b. clean, winding, some pools and shoals	0.033	0.040	0.045
c. same as above, but some weeds and stones	0.035	0.045	0.050
2. Flood plains			
a. Light brush and tree in summer	0.04	0.06	0.08
b. Developed, high intensity	0.12	0.16	0.20
c. Developed, medium intensity	0.08	0.12	0.16
d. Developed, low intensity	0.06	0.09	0.12

3. Model calibration and validation

HEC-RAS model calibration and validation aim to identify the appropriate model parameters. We selected the Manning's n value. The friction value for open channel flow is represented by the Manning's roughness coefficient. We selected the Manning's n value based on the characteristics of the study area. This selection involved comparing the area's properties with recommended ranges from existing manuals [17] and iteratively testing the value with the model until an appropriate fit was achieved. The model was changed and verified for accuracy using statistical methods, particularly the Coefficient of Determination (R²) and the Root Mean Square Error (RMSE), as shown in Equations (4) and (5). This process aimed to ensure the model's fidelity to real-world conditions.

$$R^2 = \left\{ \frac{\sum_{i=1}^{N}(Q_{Oi}-\bar{Q}_O)\times(Q_{Si}-\bar{Q}_S)}{\left[\sum_{i=1}^{N}(Q_{Oi}-\bar{Q}_O)^2\times\sum_{i=1}^{N}(Q_{Si}-\bar{Q}_S)^2\right]^{0.5}} \right\} \quad (4)$$

$$RMSE = \left\{ \frac{\sum_{i=1}^{N}(Q_{Oi}-Q_{Si})^2}{N} \right\}^{0.5} \quad (5)$$

When,

N = Number of data
Q_O = Observed water level at any time
$\bar{Q}_O$ = Average observed water level
Q_S = Modeled water level at any time
$\bar{Q}_S$ = Average modeled water level

This study utilized water level data from the M.7 gauging station on the Mun River (Seri Prachathipatai Bridge, Ubon Ratchathani Province) for model calibration (August-October 2019) and validation (August-November 2022). These periods included both flood events and intervals when the Royal Irrigation Department had suspended regulator gate operations, ensuring that water levels and volumes were unaffected by gate-related management. The accuracy of calibration and validation was then assessed using statistical metrics: the Coefficient of determination (R²) and the root mean square error (RMSE). An R² value greater than 0.6 and an RMSE value close to zero typically indicate a strong positive correlation between observed and modeled water levels. Therefore, the selected roughness coefficient was considered acceptable [19, 21].

4. Study of flow obstruction impacts

The downstream section of the Mun River, particularly in Phibun Mangsahan District, is characterized by numerous rapids of varying sizes along almost its entire length, which obstruct water flow. Kaeng Saphue, a major rapid, spans the entire width of the Mun River. Further downstream lies the Pak Mun Dam. These features raise suspicions that the dam obstructs the waterway and contributes to severe flooding in Ubon Ratchathani Province [4, 5]. Consequently, the researcher aims to investigate the impact of flow obstructions in the Mun River, focusing on the identified primary problem areas: Kaeng Saphue and the Pak Mun Dam. The study divides the analysis of flow obstructions into four distinct cases (Figure 4).
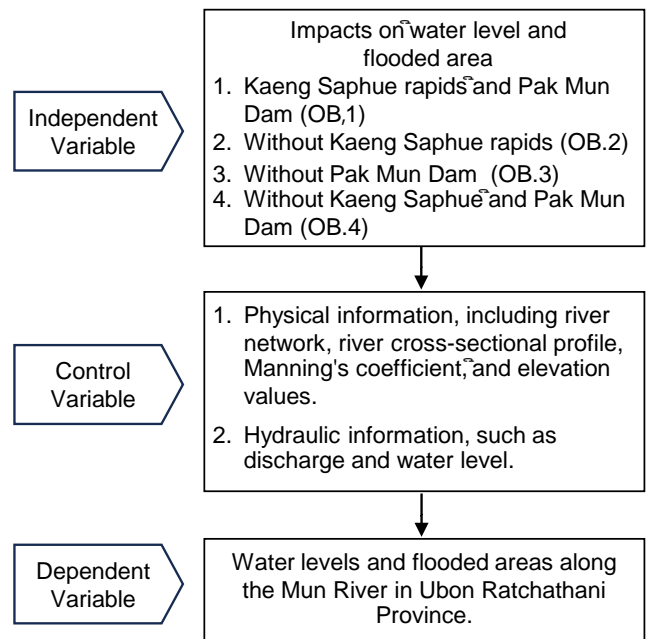
Figure 4 Conceptual framework in research.
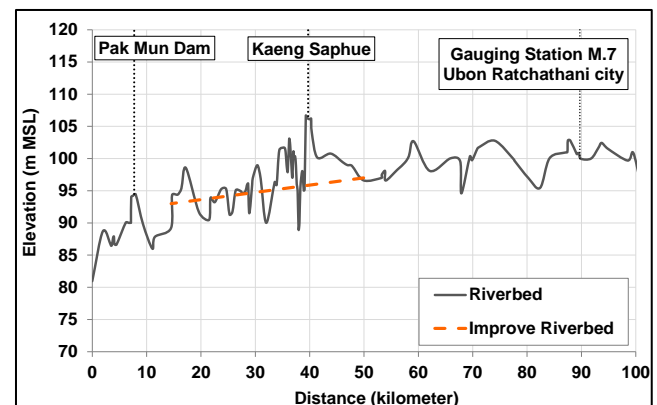
Figure 5 Longitudinal profile of riverbed before and after improvement at Kaeng Sapue.
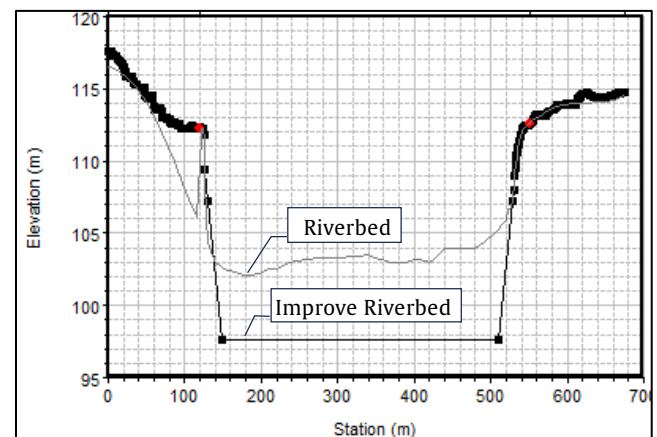
Figure 6 Riverbed cross-section before and after improvement at Kaeng Sapue.
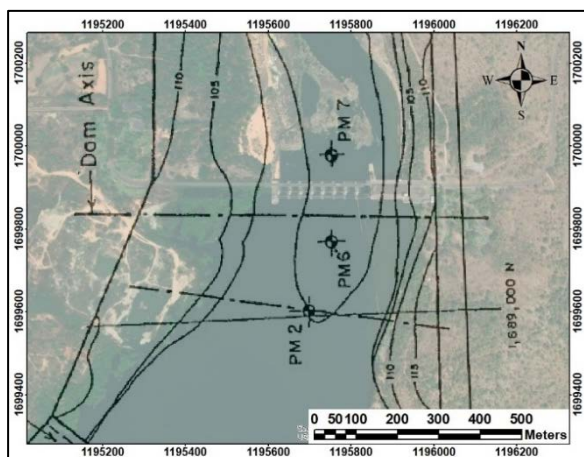
Before and after images of the Pak Mun Dam
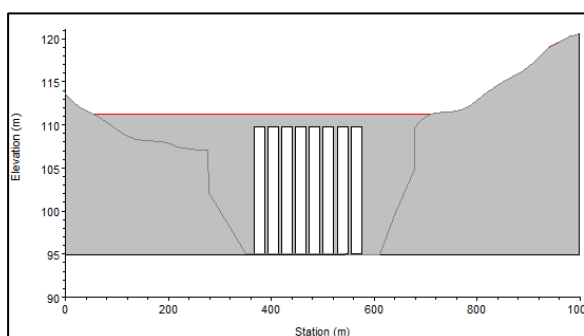
Figure 7 River cross-section after Pak Mun Dam construction.
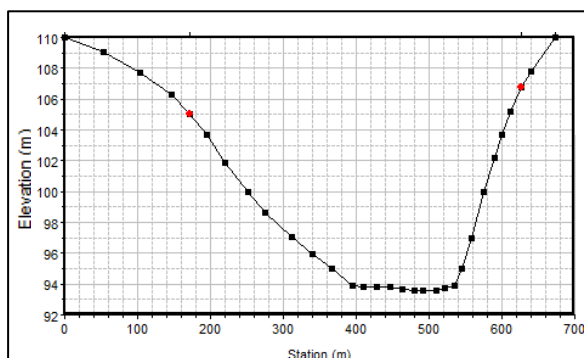
Figure 8 River cross-section before Pak Mun Dam construction.

The study case was set as the independent variable for analyzing the impact of flow obstructions across all four cases, while the same control variables were consistently applied. Physical data for the study area included the river network, river cross-sections (excluding the Kaeng Saphue and Pak Mun Dam areas), and elevation data. Hydrological data comprised flow discharge and water levels. The dependent variables obtained from this analysis were the resulting water levels and flooded areas along the Mun River in Ubon Ratchathani Province.

The HEC-RAS model was applied to simulate the effects of flow obstructions on water levels and flooded areas. The study area covered the Mun River from the M.182 gauging station (Kanthararom District, Sisaket Province) and the Chi River from the E.20A

gauging station (Maha Chanachai District, Yasothon Province), extending downstream to the Mekong River at Khong Chiam District, Ubon Ratchathani Province. The 2022 flood hydrograph was used as input for the inundation simulation.

These cases comprise:

4.1 Impact with Kaeng Saphue and the Pak Mun Dam present (current condition) (OB.1): This case assumes the existing morphology of both Kaeng Saphue and the Pak Mun Dam in the Mun River remains unchanged. (Figures 5 to 7).

4.2 Impact without Kaeng Saphue (OB.2): Derived from Case 1, this case involves removing Kaeng Saphue by improving the riverbed slope at Kaeng Saphue. We achieved this by using the normal water level value before and at the end of Kaeng Saphue, which led to an approximate riverbed slope of 1:12,000. (Figures 5 and 6).

4.3 Impact without the Pak Mun Dam (OB.3): This case, based on Case 1, looks at what happens if the Pak Mun Dam is taken away, meaning the Mun River in that area will go back to its original shape before the dam was built (Figure 8).

4.4 Impact without both the Pak Mun Dam and Kaeng Saphue (OB.4): This case combines the improvements from Case 2 (riverbed slope at Kaeng Saphue) and the original river cross-section in the Pak Mun Dam area as in Case 3.

RESULTS AND DISCUSSION

1. HEC-RAS model calibration and validation results

Prior to calibrating the Manning's roughness coefficient, a sensitivity analysis was performed by varying the n value within a range of ±5% to ±20%. The results showed that the maximum water level varied by no more than 0.15 meters (Figure 9), indicating that the model is relatively insensitive to small changes in roughness within this range.
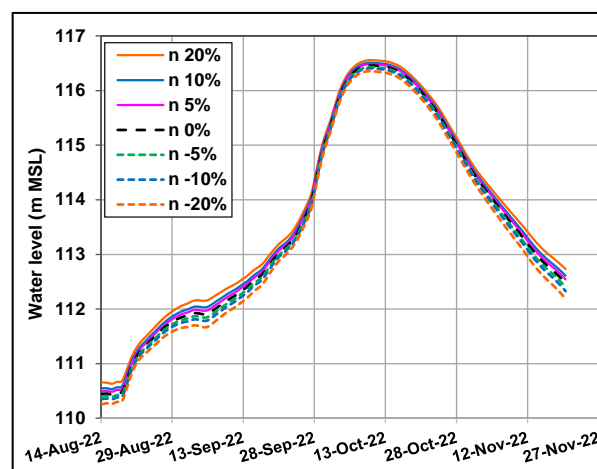
Figure 9 Sensitivity analysis results for Manning's roughness coefficient at M.7.
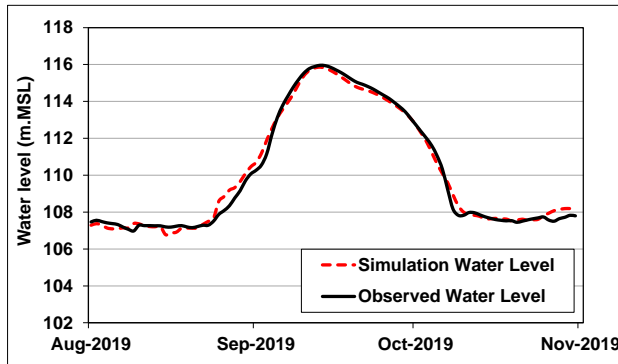
Figure 10 Comparison of observed and simulated water levels for calibration at M.7.
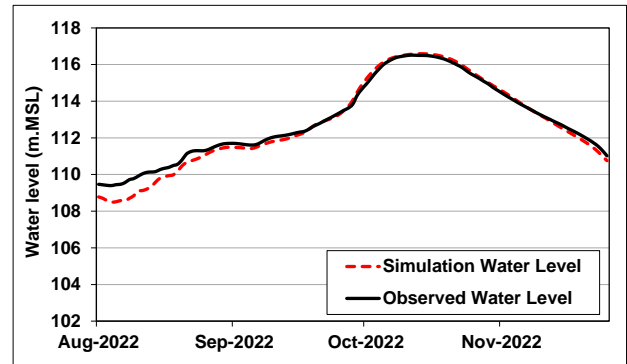
Figure 11 Comparison of observed and simulated water levels for validation at M.7.
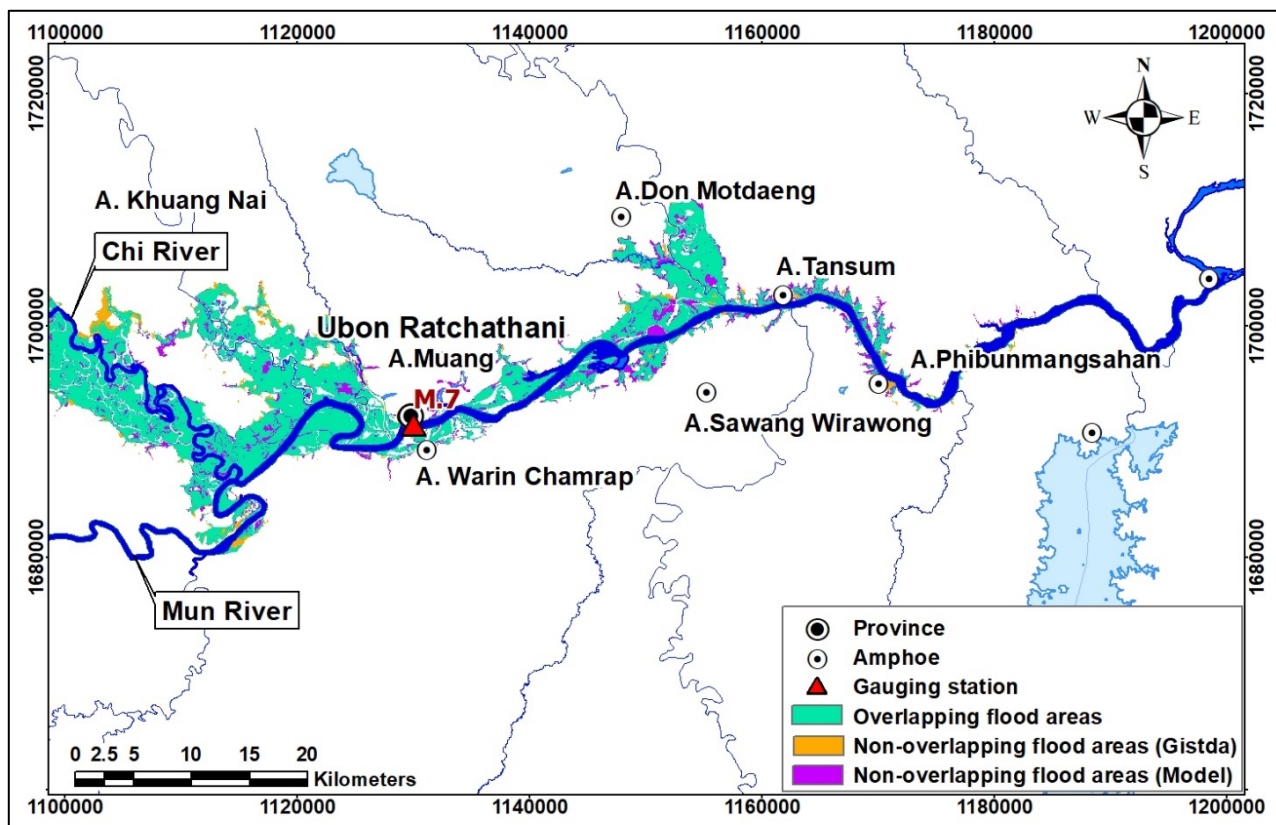
Figure 12 Spatial overlap between modeled inundation and GISTDA flood mapping.

Model calibration used 2019 water level data from the Mun River at gauging station M.7. The calibrated Manning's roughness coefficients (n) were 0.040 for normal river sections and 0.045 for rapids (Figure 10), yielding $R^2 = 0.964$ and RMSE = 0.140 m.

Model validation employed 2022 water level data (Figure 11), resulting in $R^2 = 0.978$ and RMSE = 0.057 m. These values met acceptance criteria ($R^2 > 0.6$, RMSE close to 0).

A comparison of the model-simulated flooded area with satellite imagery from GISTDA for the 2022 flood event in Ubon Ratchathani Province showed a strong agreement. The model predicted an inundated area of 483.58 sq.km., while GISTDA reported 441.40 sq.km., with an overlapping area of 408.44 sq.km., accounting for 92.53% of the GISTDA-derived flooded area (Figure 12). Discrepancies are mainly due to differences in flood extent interpretation: GISTDA excludes water bodies and wetlands, whereas the model removes only major channels and reservoirs. Additionally, limited gauging data in some areas, such as near Kaeng Saphue, may contribute to differences in simulated flood extents.

2. Results of the application of HEC-RAS model in studying the impact of flow obstructions.

The study of the four cases during the 2022 flood showed that obstacles in the water flow raised water levels much higher than in situations without these obstacles (Figures 13 and 14). The observed elevation differences extended approximately 114 kilometers along the Mun River, leading to inundation in areas from Khueang Nai District to Phibun Mangsahan District.
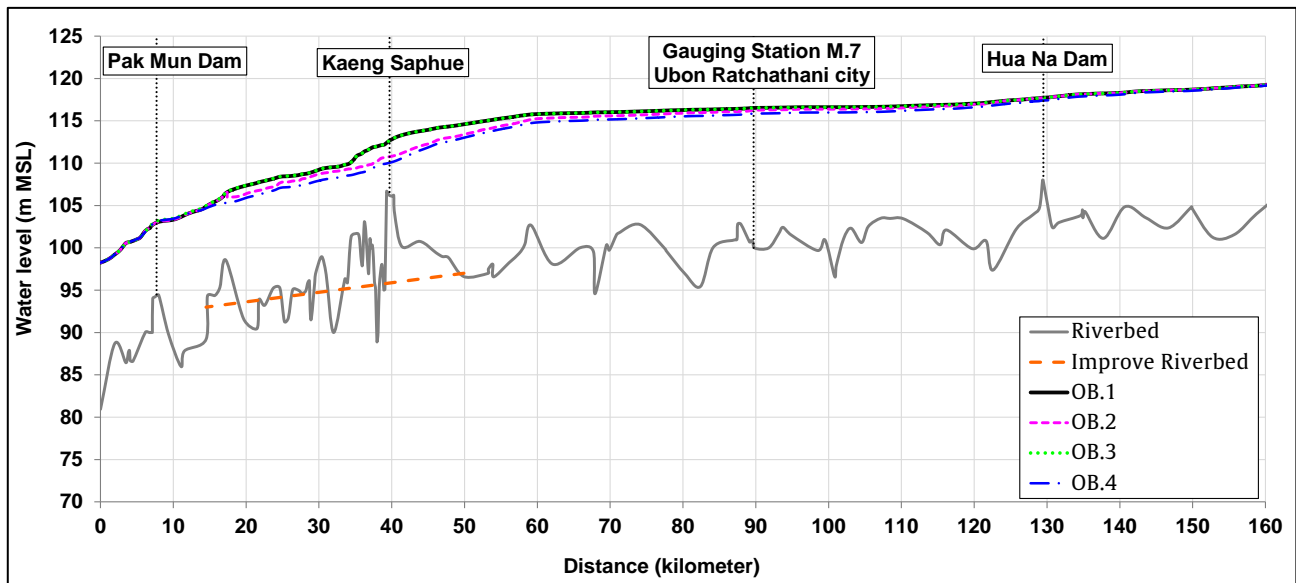
Figure 13 Simulated water levels in the Mun River under various cases.
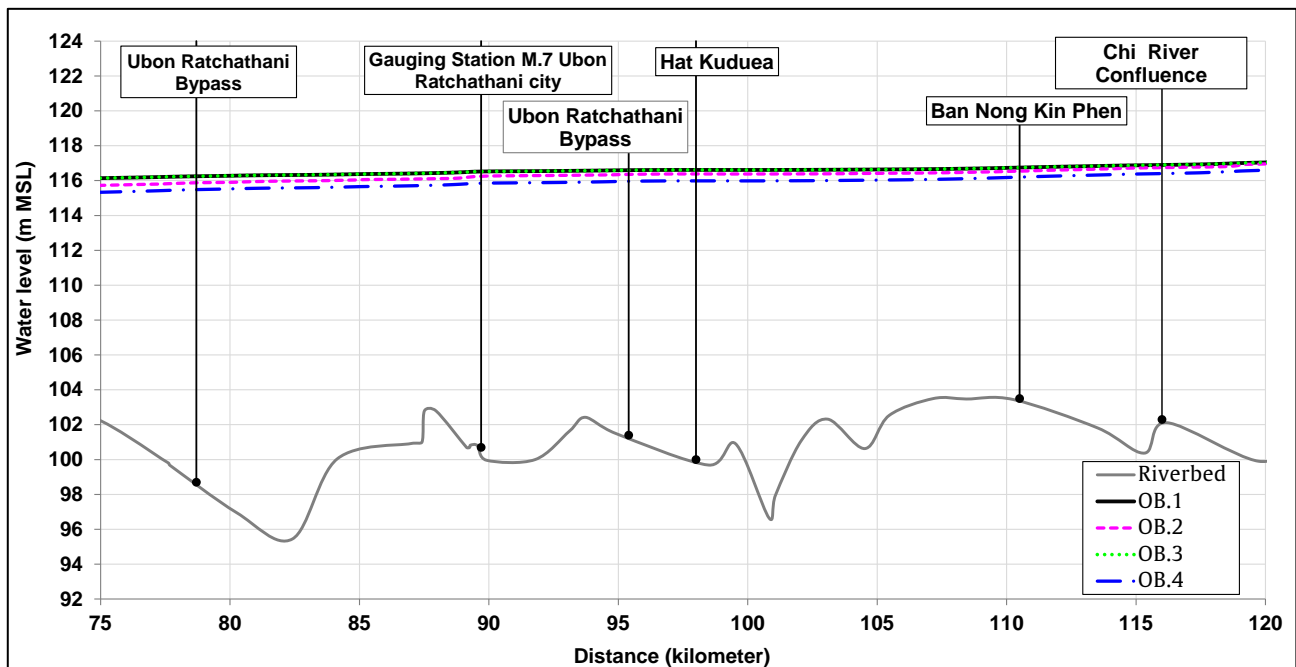
Figure 14 Simulated water levels in the Mun River under various cases (A focus on Ubon Ratchathani City).

2.1 With Kaeng Saphue and Pak Mun Dam (OB.1): This case, representing the current condition, yielded the highest water level at 116.50 m MSL. The flooded area from the overflowing Mun River in Ubon Ratchathani Province was 483.58 sq.km., with a flood duration of 75 days.

2.2 Without Kaeng Saphue (OB.2): Removing Kaeng Saphue resulted in a peak water level of 116.15 m MSL at station M.7. The flooded area decreased to 463.07 sq.km. with a flood duration of 64 days.

2.3 Without Pak Mun Dam (OB.3): This case, surprisingly, showed the same peak water level at station M.7 as the current condition (116.50 m MSL). The flooded area decreased to 483.58 sq.km. with a flood duration of 75 days.

2.4 Without both Kaeng Saphue and Pak Mun Dam (OB.4): The case without both obstructions yielded the lowest peak water level at station M.7, recorded at 115.92 m MSL. The flooded area decreased to 445.06 sq.km. with a flood duration of 60 days.

The water levels at station M.7 for all four study cases are presented in Figure 15, while the corresponding flooded areas are detailed in Table 3. The study results revealed that both the current condition (OB.1), which includes Kaeng Saphue and the Pak Mun Dam, and the case without the Pak Mun Dam (OB.3) resulted in the same peak water level of 116.50 m MSL at station M.7.

In the case without Kaeng Saphue (OB.2), the water level at station M.7 was reduced to 116.15 m MSL (a reduction of 0.35 meters). When both the Pak

Mun Dam and Kaeng Saphue were removed (OB.4), the water level at gauging station M.7 further decreased to 115.92 m MSL (a reduction of 0.58 meters). These findings align with previous studies on flood prevention in the lower Mun River basin, which indicate that improving rapids can effectively reduce water levels [11, 13].

The study's findings indicate that Kaeng Saphue is currently the primary obstruction to flow. Specifically, the presence of Kaeng Saphue consistently caused water levels to rise. Conversely, the absence of the Pak Mun Dam alone did not significantly impact the water level when Kaeng Saphue was present. However, if Kaeng Saphue was removed while the Pak Mun Dam remained, the water level still rose when compared to the scenario where both were absent. This further reinforces Kaeng Saphue's dominant role. Regarding the Pak Mun Dam, which is situated downstream of Kaeng Saphue, its riverbed level is approximately 12.0 meters lower, and its highest water level is about 3.0 meters lower than the riverbed level at Kaeng Saphue.

Critically, no backwater effect from the Pak Mun Dam was observed upstream, confirming that the Pak Mun Dam has no impact on the current flood level.
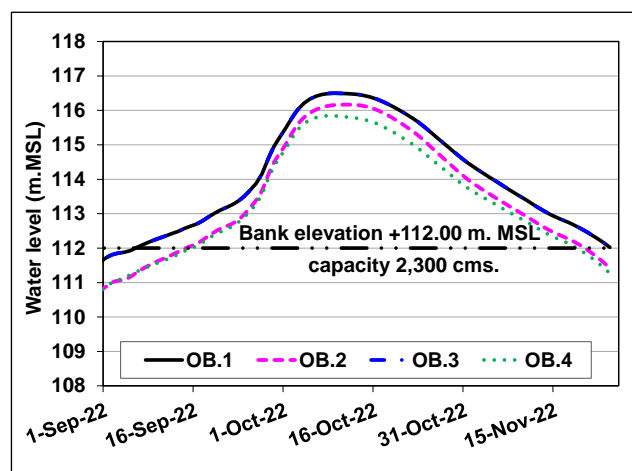
Figure 15 Water Levels at Gauging Station M.7 for Each Case.

Table 3 Effects of flow obstructions on flooding in the 2022 simulation.

Case study	Peak discharge (m³/s)	Peak water level (m MSL)	Duration of flooding (days)	Flooded area extent (km²)
OB.1 (Present)	6,166	116.50	75	483.58
OB.2	6,166	116.15	67	463.07
Percent (%)		(-0.30%)	(-10.67%)	(-4.24%)
OB.3	6,166	116.50	75	483.58
Percent (%)		(0.00%)	(0.00%)	(0.00%)
OB.4	6,166	115.92	60	445.06
Percent (%)		(-0.50%)	(-20.00%)	(-7.97%)

Despite the removal of flow obstructions, the model indicated that overflow and flooding persisted in the area. This is because the volume of floodwater still exceeded the river's capacity. Therefore, improving only Kaeng Saphue would not fully resolve the flooding issue. This observation is consistent with prior research [10], which found that while removing obstructions like weirs and culverts reduced flood length and levels, it did not eliminate flooding entirely.

CONCLUSIONS

Flooding affects the Mun River Basin due to a combination of contributing factors. This study focuses on analyzing the impact of hydraulic obstructions on the severe flooding event in 2022, which was the most significant after the historical flood of 1978. The results indicate that although flow obstructions such as Kaeng Saphue and the Pak Mun Dam are not the primary causes of flooding, excessive rainfall exceeding the river's capacity remains the dominant

factor. Nonetheless, these obstructions play a role in impeding the drainage of water into the Mekong River, leading to elevated flood levels, expanded inundation areas, and prolonged flood durations.

The downstream section of the Mun River in Phibun Mangsahan District exhibits an uneven riverbed topography, characterized by numerous potholes and rapids. This irregular geomorphology increases the roughness coefficient compared to rivers with uniform slopes, thereby reducing water flow velocity and efficiency. Therefore, any improvements or dredging activities on the downstream Mun River should ideally extend along the entire river segment, reaching its confluence with the Mekong River to effectively mitigate flooding.

However, such interventions often face environmental constraints, particularly regarding their impact on local livelihoods and traditional fishing practices. The Mun River's diverse physical characteristics contribute significantly to the rich

biodiversity of fish species in the region. Moreover, Kaeng Saphue remains an important tourist attraction in Phibun Mangsahan District, especially during April, when many visitors come for leisure and sightseeing. Therefore, this study proposes an approach that integrates engineering needs with the conservation of natural and social values. It emphasizes designing projects with ecological sensitivity; for example, the concept of improving the river channel without fully occupying the cross-section is an intriguing approach, but it must be implemented continuously along the entire river length to ensure uninterrupted flow. This approach also includes community and stakeholder participation, long-term monitoring and evaluation after construction, promotion of ecotourism, support for community economies related to biodiversity, and the establishment of joint committees involving government agencies, academic institutions, and local communities. Such collaboration will help ensure the long-term success of projects, reduce conflicts, and prevent post-implementation failures.

Regarding water resource management in the Mun River Basin and Ubon Ratchathani Province, relevant agencies have continuously addressed flood and drought challenges over time. While some issues have been resolved, many still require further attention. Flood mitigation efforts remain ongoing, with active community involvement and feedback.

Currently, the Office of the National Water Resources has developed a water chart for the Mun River Basin. This plan provides guidelines and recommendations for land use in flood-prone areas to avoid obstructing water flow. Significant flood mitigation projects include the Ubon Ratchathani Province Flood Prevention and Mitigation Project, as well as initiatives addressing flood and drought in the lower Chi-Sebai-Sebok and lower Mun River Basins. These projects involve constructing bypass channels around Yasothon and Ubon Ratchathani cities. Completed feasibility studies indicate a high readiness level for implementation. Once constructed, these projects are expected to protect Ubon Ratchathani city effectively from floods with a recurrence interval of 5 to 10 years.

ACKNOWLEDGEMENT

REFERENCES

1. Office of the National Water Resources. Summary of flood management lessons learned in Ubon Ratchathani Province in 2019 [Internet]. 2019. [cited 2025 Jan 16]. Available From: https://shorturl.asia/pJdYW.

2. Boonlert S, Sriworamas K, Sriworamas R. Flooding simulation in the Mun River Ubonratchathani Province of the year 2019 using Infoworks-ICM : In case study from Mueang Ubonratchathani District to the Estuary of the Mun river. Proceedings of the 27th National Convention on Civil Engineering; 2022 Aug 24-26; Chiang Rai, Thailand. p. 1-8.

3. Electricity Generating Authority of Thailand. Pak Mun Dam [Internet]. [cited 2025 Jan 16]. Available From: https://www.egat.co.th/home/pak-mun-dm.

4. Is it possible to demolish the Pak Mun Dam to remove obstacles in the waterway [Internet]. Thai PBS; 2022 [cited 2025 Jan 16]. Available From: https://www.thaipbs.or.th/news/content/320464.

5. Dismantle the Pak Mun Dam, restore the Mun River, and solve Ubon Ratchathani 's recurrent flood crisis (1)[Internet]. Prachatai; 2022 [cited 2025 Jan 16]. Available From: https://prachatai.com/journal/2019/10/84861.

6. Ubon Ratchathani flood: National Highway 231 at risk of collapse, heavy vehicles over 50 Tons prohibited [Internet]. Thai PBS; 2022 [cited 2025 Jan 16]. Available From: https://www.thaipbs.or.th/news/content/320506.

7. Update on Ubon Ratchathani flood 2022: Mun River water levels and impassable routes [Internet]. Thansettakij 2022 [cited 2025 Jan 16]. Available From: https://www.thansettakij.com/news/general-news/543706.

8. Methat J, Jirawat K. The study of prevention of flood in Ubon Ratchathani Province in lower Mun River Basin. JSTKU. 2022;2:73-85.

9. Pongpan K, Chuchoke A, Surachai A, Pornyamol N, Wichai N. The study of the effect of channel obstacles on stream flooding. JEDT. 2022;10:80-9.

10. Pongpan K, Surachai A, Nattakarn K, Natdanai K, Tawan T. The solutions of overbank flow to mitigate the effects of flooding for small streams. MUTNB. 2024;34:1-14.

11. Methat J. The study flood of prevention of Ubon Ratchathani Province in lower Mun River Basin [Thesis]. Bangkok: Kasetsart University; 2013.

12. Wisut S. Impacts of floods on built-up areas and infrastructure in Nan city [Thesis]. Bangkok: Chulalongkorn University; 2012.

13. Marine Department. Master Plan and Action Plan Report for the Detailed Design Study of the

Dredging of Major Rivers: The Chi River, Mun River, Loei River, and Songkhram River. Bangkok: 2017.

14. Thomas H, Nisbet TR. An assessment of the impact of floodplain woodland on flood flows. Water Environ J. 2006;21:2-13.

15. Jianyong H, Hui S, Jinxin Z, Zhenzhu M, Yuzhou Z, Wei H. Influence of multi-cross structures on the flood discharge capacity of Mountain Rivers in the Yellow River Basin. WATER. 2023;15-8.

16. US Army Corp of Engineers. HEC-RAS River Analysis System: User's Manual Version 6.0. 2021.

17. US Army Corp of Engineers. HEC-RAS River Analysis System: Hydraulics Reference Manual Version 6.0. 2021.

18. Chow VT. Open-channel hydraulics. New York: McGraw-Hill; 1959.

19. Paweena C, Preeyaphorn K. Flow estimation using Hec-Ras model a case study of Lam Takong river basin. Technical Education Journal : KMUTNB. 2020;11:1-111.

20. Punchika M. Flood modelling in the middle Chao Phraya River Basin using HEC-RAS model [Thesis]. Bangkok: Chulalongkorn University; 2022.

21. Wisuwat T, Supapap P. Flood mitigation study in Nam Loei River Basin using river basin modelling. In: The 3rd National Convention on Water Resources Engineering; 2009 Aug 6-7; Nakhon Nayok.

Physicochemical, textural, and antioxidant properties of Pandan Leaf Extract (PLE)-fortified gummy jelly

Natnirin Booranasakawee[1*], Sinee Siricoon[2], Nowwapan Donrung[1] and Thongkorn Ploypetchara[1]

[1]Expert Centre of Innovative Health Food (InnoFood), Thailand Institute of Scientific and Technological Research (TISTR), Klong Ha, Klong Luang, Pathum Thani, THAILAND

[2]Expert Centre of Innovative Herbal Products (InnoHerb), Thailand Institute of Scientific and Technological Research (TISTR), Klong Ha, Klong Luang, Pathum Thani, THAILAND

*Corresponding author: krittalak.p@gmail.com, krittalak@tistr.or.th

ABSTRACT

The presented study focuses on fortifying pandan leaf extract (PLE) into a gummy product. The PLE preparation using two carrier agents, Tween 80 (P3) and black sesame oil (P4), was applied before adding to gummy processing. Then, the PLE-fortified gummy optimization was conducted by varying the PLE concentration at 1.0% (F1), 1.5% (F2), and 2.0% (F3) by weight. Their physicochemical properties were measured by textural by Texture Profile Analysis (TPA), and *In-vitro* biochemical properties of PLE-fortified gummy were analyzed. Results of the first experiment showed that there are significant differences in pH value, total soluble solids, and color attributes, with the black sesame oil-based formulation exhibiting higher lightness (L* value) and yellowness (b* value) values (p <0.05). The result of the TPA analysis showed that the PLE-fortified gummy with black sesame oil formulation had higher hardness and chewiness than the PLE-fortified gummy with Tween 80 formulation (p <0.05). For the second experiment, the physicochemical results demonstrated that total soluble solids, acidity, and color values increased when PLE-extract concentration was added (p<0.05). Regarding increasing PLE-extract levels, the texture of gummy jelly showed a decrease in hardness and gumminess while springiness increased (p <0.05). Antioxidant properties, including free radical scavenging activity by DPPH and ABTS assays, supported the potential health benefits of pandan leaf extract in gummy jelly. This study suggests that black sesame oil is a suitable carrier for preparing pandan leaf extract for gummy production. Therefore, the PLE-fortified gummy can be produced as a functional confectionery product, paving the way for future applications in health-oriented gummy formulations.

Keywords: Gummy, Pandan leaf extract, Physicochemical properties, Phenolic compound

INTRODUCTION

Gummy jelly, classified as a gelled confectionery, constitutes a significant portion of the candy market in Thailand, accounting for approximately half of the total market share. Their increasing popularity can be attributed to consumer preferences for chewable confections [1]. Gummy jelly is a form of dried jelly highly favored among children, adolescents, and working adults due to their appealing shapes, vibrant colors, and balanced sweet-and-sour taste. These products possess a chewy, elastic texture that enhances the overall sensory experience during consumption [2, 3].

Gummy jelly typically comprises gelling agents (hydrocolloid compounds) - such as gelatin, carrageenan, or agar - combined with sweeteners like granulated sugar, glucose, or alternative sugar substitutes in carefully controlled proportions [2], making them a high-energy food product. This mixture is prepared under acidic conditions facilitated by organic acids, such as citric or malic acid. Additional ingredients may include fruit and vegetable powders, milk proteins, cereals, or herbal extracts. The formulation allows for the addition of coloring and flavoring agents. The ingredients are thoroughly mixed and heated during processing until a suitable viscosity is achieved. Then, the melted mixture is formed into molds of different sizes and/or shapes. The drying step aims to reduce the moisture content of the product and increase its solid content. Generally, the drying period ranges from 24 h to more [4]. Some gummies undergo further processing, such as coating or drying with sugar or starch, to ensure a optimize chewy texture and prevent stickiness [4]. The gummy texture can be measured by texture profile analysis (TPA), in which the deformation of different descriptors is under force, distance, and time deformation. TPA is a suitable technique for following the deformation of viscoelastic materials.

Moreover, the change in texture may be affected by the ingredient changes [4].

There has been an increasing trend toward developing confectionery products, especially gummies fortified with various functional ingredients. This innovation is motivated by the convenience of gummy consumption, ease of transport, and the ability to mask the bitter taste of vitamins or herbal extracts with the inherent sweetness and acidity of the product. Furthermore, the attractive presentation of gummies enhances consumer compliance compared to traditional pill or tablet formats. Pandan leaf extract (PLE) is derived from *Pandanus amaryllifolius* and is widely recognized for its unique aroma, antioxidant properties, and bioactive compounds, including phenolics and flavonoids. These bioactive components have been associated with various health benefits, such as anti-inflammatory and antioxidant effects, which may contribute to improved well-being. Pandan leaf extracts have been investigated for their antioxidant capacity and their potential inhibitory effects on xanthine oxidase (XO), an enzyme pivotal in purine metabolism that catalyzes the oxidation of hypoxanthine to xanthine and subsequently to uric acid [5, 6].

Nowadays, the adult and elderly group of consumers is increasingly seeking food products that promote health and well-being, such as those with antioxidant, anti-inflammatory, or uric acid-lowering properties. The previously research related studies demonstrate leaf extracts impact on gel-liked texture [7- 9]. The incorporation of pandan leaf extract (PLE) rich in phenolics and flavonoids-may be particularly beneficial for this group, as it offers potential health benefits including oxidative stress reduction and xanthine oxidase inhibition, which may contribute to better management of conditions such as hyperuricemia or gout. Currently, there is no research publication specifically on the incorporation of PLE into gummy products. A study of PLE on preserving salted duck eggs showed that an increasing amount of PLE, its texture become chewier in gel-based product [10]. This study also aims to evaluate the effects of PLE incorporation in gummy formulations, focusing on the impact of different carrier agents and varying extract concentrations on their physicochemical, texture, and antioxidant properties. The findings of this study will provide insights into the potential application of PLE in functional products for adults and elderly people.

MATERIALS AND METHODS

Pandan leaf extract preparation

The fresh Pandan (*Pandanus amaryllifolius*) leaves were purchased from an organic local farm in Thailand. They were washed with tap water, cut into small pieces, and dried using a hot air dryer at 50-55°C

for 18-20 hr. After that, they were finely ground into a powder (4-6% of moisture content). The PLE was performed using the maceration technique according to the process of Sithisam-ang et al. 2023 [11]. Briefly, ground Pandan leaf powder (18 kg) was dissolved into a 95% ethanol solution (food grade). The mixture was continuously stirred for 1 hr. and followed by a filter press machine. The residue was then re-extracted to two additional extraction cycles under the same conditions. The combined ethanolic extract from all three rounds was subsequently concentrated by solvent evaporation under vacuum conditions. The viscous PLE-extract (1.63 kg, Figure 1) is a semi-liquid phase with a dark green color containing 2.79 to 7.49 mg/kg of 2-Acetyl-1-Pyrroline (2AP). The extract was kept at -20°C until further use.

Figure 1 Pandan leaf extract.

Gummy production

The preparation of gummy fortified with pandan leaf extract was conducted as following: PLE was premixed with different carrier agents to facilitate its incorporation into the gummy jelly formulation. The 1 portion (by weight) of PLE was stirred with the 1 portion (by weight) of either Tween 80 (P1) or Black sesame oil (P2) for 20-30 min to ensure uniform dispersion. The selected carrier agent was added at a concentration of 0.50% of the total gummy formulation weight.

In the secondly experiment, it was focused on evaluating the effect of varying levels of PLE incorporation using black sesame oil as the carrier agent. The pre-mixed PLE-black sesame oil combination (1:1 w/w) was added to the gummy formulation at three different concentrations by weight: 1.0% (F1), 1.5% (F2), and 2.0% (F3), respectively, in comparison with a control (0.5% PLE-carrier mixture).

The PLE-carrier mixtures were then mixed with a standard gummy jelly base comprising 30% granulated sugar, 20% glucose syrup, 0.5% citric acid, 0.5% pectin, 8% gelatin 250 bloom, including 500 ppm of sodium benzoate and 200 ppm of potassium sorbate at 70-80°C. After that, the mixture was formed in molds into a rectangular shape and placed at 25-30°C for 2-4 hr.

Physico-chemical properties analysis

The sample was chopped and blended to analyze the moisture content using a moisture analyzer (IR-35, Denver instrument, USA). The water activity (a_w) was

also measured using a water activity analyzer (4 TE, Agua lab, UK).

The gummy sample (5 g) was vortexed with 20 mL of distilled water and homogenized at 5000 rpm for 30 sec. A clear sample solution was taken for measurement. The total soluble solid (TSS) content and pH value were conducted using a digital hand-held pocket refractometer (PAL-1 and PAL-3, Atago, Japan) and a pH meter (Seven easy, Mettler Toledo, Switzerland), respectively.

The titrimetric method No.986.13 [12] was used to analyze total titratable acidity (TTA) using an auto-titrator (DL53, Mettler-Toledo, Switzerland). Each data was calculated and reported as the percentage of citric acid content.

The measurement of color value was followed using a Minolta chromameter (CR-400, Konica Minolta, Japan). The chromameter was calibrated by a white color standard plate (Y=92.50, x=0.3165, y=0.3329) using the light source of Illuminant D_{65} 2° observer. The colorimetric data was operated as a CIE Lab scale in triplicated measurement and displayed the average data in forms of L* value (Lightness, 0-100), a* value ((-) green to (+) red), and b* value ((-) blue to (+) yellow) value.

Texture qualities analysis

Texture parameters were conducted by measuring the texture profile analysis (TPA) with a Texture Analyzer (TA500, Lloyd instrument, UK). The gummy sample was compressed twice with a cylinder prob (SMS P/25, 25 mm. diameter) and a 5-kg load cell. A probe penetrated to a depth of 50% distance at a 30.0 mm./min test speed and a 0.05 N trigger point. Ten pieces of gummy sample were evaluated for each treatment. The hardness was expressed as the maximum force (N) achieved at the first bite. Springiness related to the height that the gummy recovers during the time that elapses between the end of the first bite and the start of the second bite, unit was mm. Cohesiveness was calculated as ratio of area of second compression cycle to that of area of first compression cycle. Gumminess is defined as the multiplication of product hardness and cohesiveness and chewiness is defined as the product of hardness x cohesiveness x springiness.

Antioxidant properties analysis

The total polyphenol content (TPC) of the samples was determined using the Folin-Ciocalteu method, modified from Miliauskas et al. 2004 [13]. A standard gallic acid solution with working solutions at 10-100 mg/mL was prepared through serial dilution. The 50 µL of the sample extract was diluted with 0.95 mL of distilled water, mixed using a vortex mixer, and combined with 1 mL of the sample solution, 5 mL of 10% Folin-Ciocalteu reagent, and 4 mL of 7.5% sodium carbonate solution. After incubation at 30°C for 30 min, absorbance was measured using the U2900 UV/Vis spectrophotometer (Hitachi, Japan) at 760 nm. A calibration curve was generated using gallic acid standards, and TPC was expressed as mg gallic acid equivalent (GAE) per g of sample.

The ferric-reducing antioxidant power (FRAP) assay, adapted from Kang et al. (2010) [14], was used to assess the reducing capacity of the sample. The 0.5 mL of sample extract, standard Fe (II) solution (0-0.5 mM), or ethanol (as a blank) was added into the 2.5 mL of FRAP reagent. It was mixed and placed in the darkness at 37°C for 10 min. The spectrophotometer absorbance at 593 nm was measured. The ferric reducing capacity of each extracted sample was determined by comparing its absorbance with the standard curve and expressed as µM Fe (II)/g of sample.

The antioxidant activity of the sample extracts was assessed using the 2,2-diphenyl-1-picrylhydrazyl (DPPH) radical scavenging assay adapted from Wong and Chye (2009) [15]. A 0.2 mL aliquot of the sample extract or distilled water (blank) was mixed in a test tube, followed by 2.0 mL of 0.1 mM DPPH-methanolic solution. The mixture was shaken thoroughly and placed in the darkness at room temperature for 30 minutes. The absorbance at 517 nm was measured using a spectrophotometer. The percentage of DPPH radical inhibition was computed in comparison with a blank.

The antioxidant activity of the sample extracts was evaluated using the ABTS radical scavenging assay, following the method of Wojdylo et al. (2007) [16]. The diluted $ABTS^+$ solution (2.0 mL) was mixed with the sample extract (0.2 mL) and incubated for 6 mins before absorbance measurement at 734 nm. The percentage inhibition of its antioxidant capacity was calculated.

Statistical analysis

Data were analyzed using both the independent sample T-test and analysis of variance (ANOVA). The T-test was applied to compare means between two independent groups with the addition of different carrier agents. For multiple group comparisons, a completely randomized design (CRD) was employed with ANOVA to evaluate the effects of various levels of pandan leaf extract used in gummy jelly. The results were presented as mean and standard deviation. Mean separation was performed using Duncan's New Multiple Range Test (DMRT) at the 95% confidence level. All statistical analyses were performed using SPSS version 18.

RESULTS AND DISCUSSION

Pandan leaf extract (Figure 1) is characterized as a semi-solid, viscous resin and poor water solubility. The ethanolic pandan leaf extract contains lipophilic bioactive compounds that exhibit low solubility in water, posing challenges for their uniform incorporation

into hydrophilic gummy jelly matrices. In a preliminary study aimed at identifying an appropriate pandan leaf extract preparation, different carrier agents, Tween 80 and black sesame oil, improved the miscibility of the otherwise viscous and semi-solid ethanolic extract. Moreover, the combination of PLE with other ingredients such as glycerin, maltitol syrup, and gelatin affected the solubility of the extracts and its functional integration into the gummy jelly product.

In this experiment, carrier agent refers to a substance used to facilitate the incorporation, dispersion, stabilization, or controlled release of PLE active compounds. Therefore, the first experiment investigated the use of different carrier agents, specifically Tween 80 and black sesame oil, to facilitate the incorporation

of pandan leaf extract into gummy formulations at a minimum concentration of a minimum concentration 0.5% by weight, as illustrated in Figure 2.
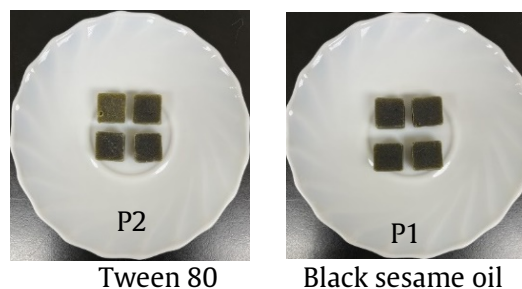
Tween 80   Black sesame oil
Figure 2 Gummy fortified with pandan leaf extract mixed with different carrier agents.

Table 1 Physicochemical properties of the PLE-fortified gummy using different carrier agents.

Physicochemical properties	P1	P2
Water activity (a_w) ns	0.73 ±0.01	0.74 ±0.01
pH value ns	4.18 ±0.02	4.18 ±0.02
Total soluble solids (°Brix)	76.54 ±1.60[a]	75.43 ±1.53[b]
Total acidity as citric acid (%)	1.57 ±0.04[a]	1.26 ±0.02[b]
Color:		
L* value	15.94 ±0.91[b]	26.8 3±0.88[a]
a* value	1.97 ±0.18[a]	1.15 ±0.22[b]
b* value	2.98 ±0.64[b]	8.46 ±1.68[a]

Note: [a-b]Different superscript letters in the same row are significantly different according to independent sample T-test at $p < 0.05$.
[ns]no significant difference values ($p \geq 0.05$).

Table 2 Texture properties of the PLE-fortified gummy using different carrier agents.

Texture properties (TPA)	P1	P2
Hardness (N)	90.75 ±25.45[b]	97.77 ±13.03[a]
Adhesiveness (N.mm)	0.26 ±0.14[b]	0.32 ±0.20[a]
Springiness ns	0.94 ±0.04	0.97 ±0.04
Gumminess (N) ns	48.62 ±13.80	47.25 ±9.26
Chewiness (N)	41.82 ±10.70[b]	45.82 ±9.03[a]
Stringiness (mm)	0.66 ±0.08[a]	0.25 ±0.11[b]

Note: [a-b]Different superscript letters in the same row are significantly different according to the independent sample T-test at $p < 0.05$.
[ns]no significant difference values ($p \geq 0.05$).

The chemical and physical characteristics of both formulations are presented in Table 1. The results indicated that the two formulations of gummy exhibited similar pH values, ranging from 4.18 to 4.19, with water activity levels between 0.733 and 0.742, and total soluble solids measuring between 75.43°Brix and 76.54°Brix. The physicochemical properties of gummy formulations fortified with pandan leaf extract (PLE) were significantly influenced by the type of carrier agent used. Similarly, the report that the commercial

gummies contained a high moisture and varied in widely water activity between 0.51-0.79 [17, 18].

In terms of color value, the incorporation of black sesame oil as a carrier agent resulted in significantly higher lightness (L*) and yellowness (b*) values compared to using Tween 80 ($p < 0.05$). The differences in pH value and total soluble solids between two formulations were relatively minor; however, total acidity was significantly lower in the black sesame oil-based formulation ($p < 0.05$). It might be Tween 80 was more effective in improving solubility and

integrating the PLE within the gummy jelly matrix, possibly due to its amphiphilic composition, which aids in emulsification and dispersion.

In terms of texture parameters, as assessed by Texture Profile Analysis (TPA) (as shown in Table 2), gummy formulas utilizing Tween 80 and black sesame oil as carrier agents revealed significant differences in textural attributes such as hardness, chewiness, adhesiveness, and stringiness ($p < 0.05$). The hardness of the gummy formulation incorporating black sesame oil was exceptionally high compared to that of the formulation using Tween 80. It could be due to the slight polarity of Tween 80. However, due to the low fortification level of PLE at 0.5%, no significant effects in adhesiveness and springiness were observed.

Studies have demonstrated that incorporating oils and emulsifiers into gummy formulations can improve the integration and stability of hydrophobic compounds. For instance, research on oil-in-water emulsions prepared with sesame oil and protein isolates showed that stable emulsions with suitable rheological properties could be formulated, highlighting the emulsifying capabilities of sesame oil. Additionally, using emulsifiers in confectionery has been shown to aid in emulsifying fats in products like caramel, fudge, and toffee, suggesting a similar potential in gummy formulations. While direct studies on black sesame oil in gummy products are limited, the findings indicate that lipid-based composition could similarly aid emulsification and dispersion within gummy matrices [19].

Table 3 shows the antioxidant properties of PLE-fortified gummies regarding total phenolic content (TPC), ferric reducing antioxidant power (FRAP), and DPPH and ABTS free radical scavenging assays. The results were found that the PLE-fortified gummy formulation with Tween 80 had a higher TPC than that of the formulation using black sesame oil, but the latter exhibited greater FRAP values ($p < 0.05$). This discrepancy suggests that while Tween 80 may enhance efficient phenolic solubility (as the report of Skrypnik & Novikov (2020) [20], who demonstrated significantly increased phenolic recovery from apple pomace at 0.5-1.0% Tween 80), black sesame oil exhibits a more favorable medium for antioxidant activity (as a previously report of Bopitiya & Madhujith (2013) [21], that showed vigorous antioxidant activity with high total phenolic content and significant DPPH and ABTS radical scavenging activities. Regarding the biochemical compound of pandan leaf extracts and black sesame oil, which possess notable antioxidant properties, gummy fortified with PLE was also found to have significant antioxidant activity.

Table 3 Biochemical properties of the PLE-fortified gummy using different carrier agents.

Biochemical properties	P1	P2
Total phenolic content (μg GAE/g sample)	177.42 ±20.07[a]	109.22 ±4.53[b]
FRAP (μM Fe^{2+}/g sample)	766.02 ±26.37[b]	1180.19 ±191.83[a]
DPPH* (%Inhibition) [ns]	37.72 ±0.55[a]	26.75 ±0.60[b]
ABTS* (%Inhibition)	18.34 ±0.05[a]	9.54 ±0.20[b]

Note: [a-b]Different superscript letters in the same row are significantly different according to the independent sample T-test at $P < 0.05$.

[ns]no significant difference values ($p \geq 0.05$).

Tween 80 (polysorbate 80), a nonionic surfactant, is commonly used in food systems to emulsify hydrophobic substances due to its ability to reduce interfacial tension and enhance the dispersion of lipophilic compounds in hydrophilic matrices [22]. It effectively disperses ethanolic extracts in aqueous environments by lowering interfacial tension, thus promoting the homogeneous distribution of the extract throughout the gummy matrix. In contrast, black sesame oil serves as a natural lipid-based carrier and is also suitable for solubilizing hydrophobic plant compounds. Its rich content of unsaturated fatty acids and antioxidant compounds makes it an excellent natural carrier that may contribute to both the nutritional value and positively influence the sensory flavor and texture of the finally gummy jelly [23]. However, using Tween 80 as a carrier agent may impart a slightly bitter and astringent taste to products, as indicated by its characteristic properties -the interaction of Tween 80 with salivary proteins and mucous membranes, leading to a puckering mouthfeel. Due to the use of Tween 80, its surfactant properties may disrupt the lipid-protein balance in saliva, causing a similar tactile sensation. Additionally, residual surfactant on the tongue may interfere with taste perception or enhance bitter notes, especially at higher concentrations [24]. Moreover, other agents such as sugars, fat, and oil frequently used to mask astringency, which is linked with plants extract. They may inhibit the interactions between salivary proteins and tannin compound or other astringents [24].

These findings suggest that the use of black sesame oil enhanced color parameters. At the same time, Tween 80 was more effective in improving solubility and integrating the PLE within the gummy jelly matrix, possibly due to its amphiphilic composition,

which aids in emulsification and dispersion. Consequently, the P2 formulation, which uses black sesame oil as the PLE-carrier agent for gummy processing, was selected for the second experiment, in which the concentration of pandan leaf extract incorporated into the product was varied between 1.00% and 2.00%.

The study investigated the incorporation of pandan leaf extract into gummy formulations by mixing 1 portion of pandan leaf extract with 1 portion of black sesame oil by weight and adding this mixture to the product at concentrations of 1.0% (F1), 1.5% (F2), and 2.0% (F3) by weight, respectively in comparison with a control gummy formulation. Representative product images are presented in Figure 3, and the chemical-physical characteristics are detailed in Table 4. The experimental results indicated that the three gummy formulations exhibited water activity (a_W) values between 0.74 and 0.75, total soluble solids ranging from 76.54°Brix to 79.22°Brix, and pH values between 4.20 and 4.25. Total acidity levels were within the range of 0.52% to 0.68%, showing minimal variation among the formulations. While statistical analysis indicated slight differences in lightness (L* value) and yellowness (b* value) among

the formulations, particularly with lower values observed in F1 compared to F2 and F3 with a decreasing trend of PLE, ($p < 0.05$), these variations were not visually distinguishable. This suggests that higher amounts of pandan leaf extract contribute to a slightly darker product color.
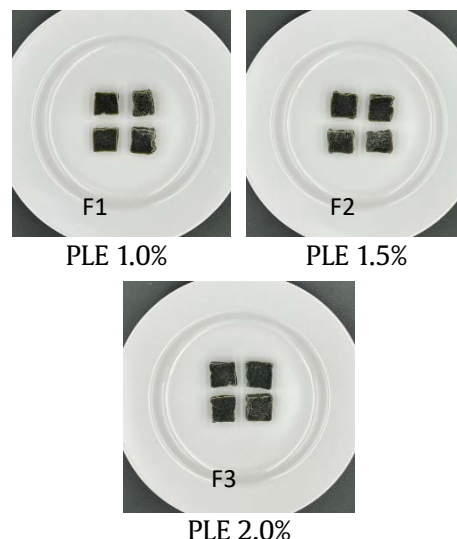
Figure 3 Gummy fortified with different amounts of pandan leaf extract.

Table 4 Physicochemical properties of gummy fortified with pandan leaf extract at different amounts.

Physicochemical properties	F1	F2	F3
Water activity (a_W) ns	0.74 ± 0.01	0.74 ± 0.01	0.75 ± 0.02
pH value ns	4.20 ±0.01	4.25 ±0.01	4.20 ±0.01
Total soluble solids (°Brix)	79.01 ±0.05[a]	79.22 ±0.00[a]	76.83 ±2.05[b]
Total acidity as citric acid (%)	0.68 ±0.01[a]	0.52 ±0.00[c]	0.63 ±0.01[b]
Color:			
L* value	40.23 ± 0.41[b]	41.13 ± 0.56[a]	41.53 ± 0.30[a]
a* value	3.51 ± 0.05[a]	3.41 ± 0.05[b]	3.34 ± 0.06[c]
b* value	-1.99 ±0.18[a]	-1.93 ± 0.07[a]	-1.63 ± 0.17[b]

Note: [a-c]Different superscript letters in the same row are significantly different according to Duncan's new multiple range test at $p < 0.05$.
ns no significant difference values ($p \geq 0.05$).

Table 5 Texture properties of gummy fortified with pandan leaf extract at different amounts.

Texture properties (TPA)	F1	F2	F3
Hardness (N)	121.15 ±25.66[a]	60.85 ±8.61[b]	70.25 ±5.76[b]
Adhesiveness (N.mm) ns	0.22 ±0.13	0.28 ±0.09	0.16 ±0.11
Springiness	0.89 ±0.08[b]	0.93 ±0.04[ab]	0.98 ±0.03[a]
Gumminess (N)	52.18 ±19.05[a]	29.03 ±4.48[b]	30.34 ±7.71[b]
Chewiness (N)	46.68 ±13.66[a]	27.54 ±3.57[b]	29.52 ±6.96[b]
Stringiness (mm)	1.00 ±0.39[a]	0.75 ±0.23[b]	0.44 ±0.13[b]

Note: [a-b]Different superscript letters in the same row are significantly different according to Duncan's new multiple range test at $p < 0.05$.
ns no significant difference values ($p \geq 0.05$).

The analysis of textural attributes in gummy formulations, conducted through Texture Profile Analysis (TPA), revealed that increasing the concentration of pandan leaf extract from 1.0% to 2.0% resulted in statistically significant differences ($p < 0.05$) in parameters such as hardness, springiness, gumminess, chewiness, and stringiness. Specifically, there was a trend of decreasing hardness and gumminess, while springiness increased, leading to a reduction in chewiness. Notably, the variations in pandan leaf extract concentration did not significantly affect the adhesiveness of the gummies, as detailed in Table 5. These findings align with previous research indicating that the incorporation of plant extracts can influence the textural properties of gummy candies, affecting parameters such as hardness and springiness. Similarly, the report by Charoen et al. (2015) [9] supports this result. The addition of herbal extracts to gelatin-based gummy formulations altered the gel network structure, resulting in changes to mechanical properties including reduced hardness and increased elasticity. This effect is likely due to interactions between phytochemical compounds in the extracts and the gelatin matrix, which may interfere with protein crosslinking and water distribution, thus modifying the gummy's texture.

Regarding the biochemical compound of pandan leaf extracts, which possess notable antioxidant properties, gummy fortified with *Pandanus amaryllifolius* extract was found to have significant antioxidant activity, as shown in Table 6. While the PLE concentration increased, antioxidant activity in DPPH and ABTS assays also improved ($p < 0.05$). Notably, the highest concentration (2.0%) exhibited significantly enhanced DPPH and ABTS radical scavenging abilities ($p < 0.05$), confirming the presence of potent bioactive compounds in the extract, especially flavonoids and phenolic compounds. The PLE had a total phenolic content (TPC) 126.76 ±1.45 mg GAE/g sample and exhibited 57.01 ±4.23% of ABTS free radical scavenging inhibitory activity (Do not shown in this report). This result showed the potential of pandan leaf extracts as functional ingredients in food products, owing to their rich phytochemical profile and associated health benefits. While direct studies on PLE-infused gummy confections are scarce, successfully incorporating other herbal extracts into gummies suggests a promising avenue for future research and product development.

The incorporation of PLE into gummy formulations presents a promising avenue for functional food development. The findings indicate that black sesame oil is a preferable carrier agent due to its superior impact on color, texture, and antioxidant retention. Additionally, increasing PLE concentration enhances bioactivity, though it may alter textural attributes.

Table 6 Biochemical properties of gummy fortified with pandan leaf extract at different amounts.

Biochemical properties	F1	F2	F3
Total phenolic content (μg GAE/g sample)	283.00±67.21[b]	268.54±68.67[b]	356.97±89.74[a]
FRAP (μM Fe^{2+}/g sample)	357.80±0.50[c]	431.00±0.25[b]	508.53±0.85[a]
DPPH* (%Inhibition)	34.39±0.80[c]	39.02±0.34[b]	51.97±0.74[a]
ABTS* (%Inhibition)	6.98±0.55[c]	19.04±0.63[b]	22.72±0.76[a]

Note: [a-c]Different superscript letters in the same row are significantly different according to Duncan's new multiple range test at $p < 0.05$.

CONCLUSIONS

This study explored the development and characterization of PLE-fortified gummy formulations, focusing on their physicochemical, textural, and antioxidant properties. The incorporation of PLE using black sesame oil as a carrier agent led to a more desirable texture and color, and compared to Tween 80, resulted in a more favorable texture, color, and antioxidant power in terms of FRAP. The increasing PLE concentration between 1.0%-2.0% influenced the gummy's structural integrity, reducing hardness and gumminess while increasing springiness. Furthermore, antioxidant assays confirmed the potential bioactive benefits of PLE-black sesame oil, particularly at higher concentrations, suggesting its suitability as a functional ingredient in confectionery products. However, the study's claim of success is limited by the absence of sensory evaluation, a critical step for assessing consumer acceptability and ensuring the success of the product in the market.

Additionally, the results of this study not only demonstrate a predictable cause–effect relationship between PLE concentration and antioxidant capacity but also highlighting the potential applications of these finding. A greater emphasis on the potential degradation or transformation of PLE components during processing, along with comparison with a control (without PLE), would have provided more insightful conclusions. The findings of this research provide a foundation for future innovations in health-oriented gummies, emphasizing the potential application of PLE as a natural antioxidant source in functional food development.

REFERENCES

1. Euromonitor International. Sugar Confectionery in Thailand [Internet]. 2024 Aug. Available from: https://www.euromonitor.com/sugar-confectionery-in-thailand/report.

2. Burey P, Bhandari BR, Rutgers RPG, Halley PJ, Torley PJ. Confectionery gels: a review on formulation, rheological and structural aspects. Int J Food Prop. 2009;12:176-210.

3. Marfil PHM, Anhê ACBM, Telis VRN. Texture and microstructure of gelatin/corn starch-based gummy confections. Food Biophys [Internet]. 2012;7:236-43. Available from: https://doi.org/10.1007/s11483-012-9262-3.

4. Delgado P, Bañón S. Determining the minimum drying time of gummy confections based on their mechanical properties. CyTA J Food [Internet]. 2015;13(3):329-35. Available from: https://doi.org/10.1080/19476337.2014.974676.

5. Quyen NTC, Quyen NTN, Nhan LTH, Toan TQ. Antioxidant activity, total phenolics and flavonoids contents of *Pandanus amaryllifolius* (Roxb). IOP Conf Ser Mater Sci Eng [Internet]. 2020;991:012019. Available from: https://doi.org/10.1088/1757-899X/991/1/012019.

6. Prasad MP, Rajkumar V. Xanthine oxidase inhibitory activity of *Pandanus amaryllifolius* leaf extracts. Int J Pharm Sci Res. 2014;5(10):4372-5.

7. Thilavech T, Sutiyaporn A, Kanchnadumkerng P, Sata VH, Parichatikanond W, Charoenwiwattanakij P, et al. Development of gummy jelly incorporated with *Lysiphyllum strychnifolium* leaf extract and its antioxidant and α-glucosidase inhibitory activities. Nat Life Sci Commun [Internet]. 2023;22(2):e2023019. Available from: https://doi.org/10.12982/NLSC.2023.019.

8. Aiello F, Caputo P, Rossi CO, Restuccia D, Spizzirri UG. Formulation of antioxidant gummies based on gelatin enriched with citrus fruit peels extract. Foods [Internet]. 2024;13:320. Available from: https://doi.org/10.3390/foods1302032.

9. Charoen R, Savedboworn W, Phuditcharn-chnakun S, Khuntaweetap T. Development of antioxidant gummy jelly candy supplemented with *Psidium guajava* leaf extract. KMUTNB Int J Appl Sci Technol [Internet]. 2015;8(2):145-51. Available from: https://doi.org/10.14416/j.ijast.2015.02.002.

10. Aprita IR, Letis ZM, Kemalawaty M, Anwar Ch, Sukinem, Irmayanti. Effectiveness of Pandan wangi (*Pandanus amaryllifolius)* leaf extract on the quality of preserving salted duck eggs. Jurnal Pertanian Terapan of Jurnal Roce (Agroscience) [Internet]. 2024;1(2):196-208. Available from: https://jurnal.rocewisdomaceh.com/index.php/roce.

11. Sithisam-ang D, Wanlapa S, Wachirasiri K, Kamprungdet S, Nanudorn J, Hankhunto D, et al. Development of technology for the production of plant and wastes from fish processing extracts to strengthen the bone and joint system for the pre- and aging society in semi-industrial level. Project report no. 6718101082. Thailand Institute of Scientific and Technological Research; 2023.

12. AOAC International. Official Methods of Analysis. 17th ed. Gaithersburg, MD: Association of Analytical Communities; 2000.

13. Miliauskas G, Venskutonis PR, Van Beek TA. Screening of radical scavenging activity of some medicinal and aromatic plant extracts. Food Chem [Internet]. 2004;85:231-7. Available from: https://doi.org/10.1016/j.foodchem.2003.05.007.

14. Kang OL, Yong PF, Ma'aruf AG, Osman H, Nazaruddin R. Physicochemical and antioxidant studies on oven-dried, freeze-dried and spray-dried agaro-oligosaccharide powders. Int Food Res J. 2014;21(6):2363-7.

15. Wong JY, Chye FY. Antioxidant properties of selected tropical wild edible mushrooms. J Food Compos Anal. 2009;22:269-77.

16. Wojdylo A, Oszmianski J, Czemerys R. Antioxidant activity and phenolic compounds in 32 selected herbs. Food Chem. 2007;105:940-9.

17. Wills D. Water activity and its importance in making candy. The Manufacturing Confectioner. 1998;71-4.

18. Barbosa-Cánovas GV, Fontana AT Jr, Schmidt SJ, Labuza TP. Water activity in foods: Fundamental and applications. In: Technology & Engineering. Wiley Publisher; 2020. p. 640.

19. Brewer DR, Franco JM, Garcia-Zapateiro LA. Rheological properties of oil-in-water emulsions prepared with oil and protein isolates from sesame (*Sesamum indicum*). Food Sci Technol (Campinas) [Internet]. 2016;36(1):64-9. Available from: https://doi.org/10.1590 /1678-457X.6761.

20. Skrypnik L, Novikova A. Response surface modeling and optimization of polyphenols extraction from apple pomace based on nonionic emulsifier. Agronomy [Internet]. 2020;10(92): Available from: https://doi:10.3390/agronomy10010092.

21. Bopitiya D, Madhujith T. Antioxidant activity and total phenolic content of sesame (*Sesamun indicum* L.) seed oil. Tropical Agriculture Research. 2013; 24(3):296-302.

22. Jafari SM, He Y, Bhandari B. Nano-emulsion production by sonication and micro fluidization- a comparison. Int J Food Prop. 2008;11(4):731-42.

23. Pathak N, Rai AK, Kumari R, Bhat KV. Value addition in sesame: A perspective on bioactive components for enhancing utility and profitability. Pharmacogn Rev. 2014;8(16):147-55.

24. Pires MA, Pastrana LM, Fucinos P, Areu CS, Oliveira SM. Sensorial Perception of Astringency: Oral Mechanisms and Current Analysis Methods. Food [Internet]. 2020;9(8):1124. Available from: https://doi:10.3390/foods9081124.

Analysis and improvement of PCB manufacturing efficiency using discrete-event simulation: An electrical industry use case

Sookjai Promprasansuk[1]*, Wirote Ritthong[1] and Suparatchai Vorarat[2]

[1]Department of Mechanical Engineering, Faculty of Engineering and Technology, Shinawatra University, Pathum Thani 12160, THAILAND

[2]College of Engineering and Technology, Dhurakij Pundit University, Bangkok 10210, THAILAND

*Corresponding author: sookjai.p@siu.ac.th

ABSTRACT

The production of Printed Circuit Boards (PCBs) manufacturing is a complex process where companies must constantly balance minimizing costs, ensuring the stringent quality standards demanded by modern electronics, and accelerating production timelines to meet market demands. Discrete Event Simulation (DES) allows manufacturers to create dynamic digital models of their production lines, enabling them to visualize material flows, accurately identify operational bottlenecks, and thoroughly evaluate the potential impact of process changes in a virtual setting. This study improvement project focused on enhancing the lead welding process, likely-through robotic automation-to improve speed and consistency. The comprehensive financial analysis revealed that an initial investment outlay of 1.5 million baht, anticipated over a 5-year operational period, is projected to yield substantial financial returns. Specifically, the project is expected to generate a considerable annual net cash flow, after tax, of 1.98 million baht. Employing a standard corporate discount rate of 10% to appropriately reflect the time value of money and investment risk, the evaluation yielded compelling metrics indicative of strong profitability. The project features a remarkably short discounted payback period of only 10 months, signifying swift recovery of the initial capital invested. Furthermore, it generates a strong positive net present value (NPV) of 1.15 million baht, confirming that the present value of anticipated future earnings significantly outweighs the initial and ongoing costs. The investment's attractiveness is further underscored by an exceptionally high internal rate of return (IRR) of 87% and a robust modified internal rate of return (MIRR) of 61%, which provides a more realistic measure of profitability by accounting for the reinvestment rate of cash flows. This significant outperformance strongly confirms the project's substantial economic value, providing compelling justification for management to confidently proceed with the investment as a strategically sound decision poised to enhance operational efficiency and long-term profitability.

Keywords: Discreate-Event simulation, PCB manufacturing, MIRR, SMT-Line

INTRODUCTION

Discrete Event Simulation (DES) has become a widely recognized industrial analysis tool, particularly valuable in manufacturing for creating detailed production process models. It helps identify weaknesses and improvement opportunities in both resource allocation and operational cost reduction [1, 2]. Modern DES software like FlexSim offers diverse applications spanning from assembly line improvements to transportation management [3-5]. Case studies demonstrate DES's significant role in transforming production systems. Zhang and Liu [3] successfully employed FlexSim to enhance production scheduling, while Jiang and Zhang [4] applied it to flexible assembly lines. Liu and Wang [5] implemented it for transportation planning, showcasing the tool's adaptability [6]. DES applications extend beyond manufacturing, proving useful in healthcare system planning [7] and the automotive industries [6]. Its effectiveness stems from handling system complexity, with Pace [8] detailing crucial simulation accuracy factors. Recent advances in multi-level simulation, particularly Digital Twin applications, have significantly boosted DES's predictive capabilities [9]. Combining DES with automation brings substantial benefits to electronics manufacturing. Lee and Kim [10] found automation increases output while reducing errors, though Garcia et al. [11] caution that thorough financial analysis remains essential. This research focuses on applying DES to enhance PCB manufacturing efficiency by integrating knowledge from flexible production systems [2-6] production scheduling [3] and automation [10, 11] to develop practical industrial solutions. The study results show that investing in automation systems for PCB soldering processes not only leads to increased

production efficiency and reduced operating costs, but also proves to be highly economically viable based on standard economic investment evaluation criteria, reinforcing the importance of comprehensive financial analysis in business decision-making.

MATERIALS AND METHODS

Manufacturing simulation software that allows manufacturers to simulate production processes and analyze their performance. This program can help manufacturers identify bottlenecks in production processes and find solutions to improve efficiency. The analysis and improvement of printed circuit board (PCB) production efficiency with FlexSim software version 19.1 can be done in the following steps:

1. Collect data about the entire production process, from raw materials to finished products. This data includes information about machinery, equipment, labor, and production steps as shown in Figure 1.

2. Create a model of the production process as illustrated in Figure 3.

3. Analyze the model of the production process and find solutions to improve efficiency as summarized.

4. based on the findings shown in Table 5.

From Figure 1 as shown flowchart within the SMT process (Surface Mount Technology) process is a method of assembling electronic components onto a printed circuit board (PCB). The process begins with the input of the workpiece into the system. The workpiece is then inspected to ensure that it is free of defects. The next step is the soldering process. In this step, the solder paste is applied to the PCB and the components are placed in their correct position. The PCB is then passed through a reflow oven, which melts the solder and bonds the components to the PCB. After the soldering process, the PCB is trimmed to remove any excess solder. The PCB is then cleaned and inspected again. The next step is the assembly process. In this step, the components that were not soldered in the SMT process are added to the PCB. These components include connectors, switches, and other devices. The assembly process is followed by the welding and wiring process. In this step, the components that require welding or wiring are connected to each other. The next step is the transformer installation process. In this step, the transformer is installed on the PCB and the final step the screw and nut installation process. In this step, the screws and nuts are installed to secure the components to the PCB.

From Figure 2. As shown the manual soldering process is a method of assembling electronic components onto a printed circuit board (PCB) by hand. The process is typically used for small-scale production or for components that are too large or complex to be soldered by machine.
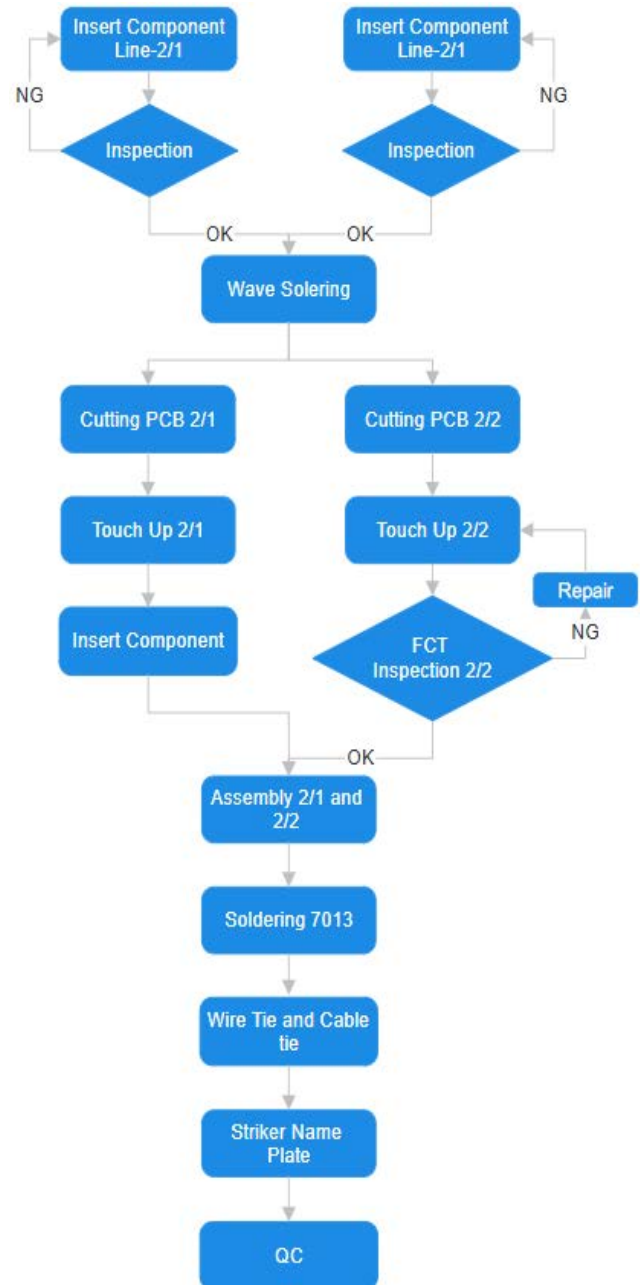

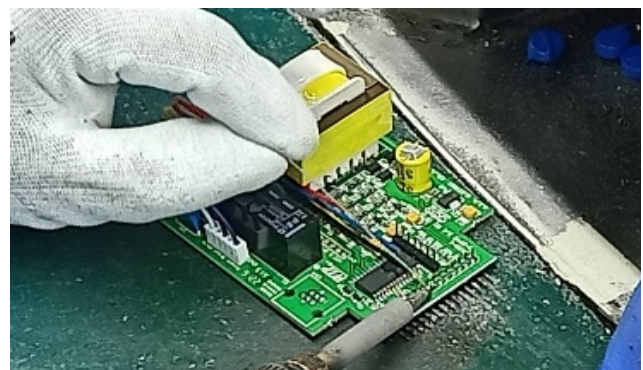**Figure 1** Flowchart within the SMT process.

Figure 2 Welding process using manual labors.

This research uses FlexSim version 19.1 manufacturing simulation software, a tool that allows manufacturers to dynamically model manufacturing processes and analyze their performance. This software

plays an important role in identifying bottlenecks in the manufacturing process and proposing solutions to improve efficiency. It is noted that using FlexSim version 19.1 software, the steps to analyze and improve the efficiency of printed circuit board (PCB) manufacturing are detailed as follows. First, comprehensive data on the entire PCB manufacturing process, from raw material input to finished products, is collected. These data are an important input parameters for the model, including: Machine and equipment data: production capacity, rotational speed, setup time, processing time, breakdown rate, and maintenance time; Labor data: the number of employees working at each station, work capacity, and work schedule; Manufacturing process data: production steps (as shown in Figure 1), cycle time, transportation time, and inter-station storage space; Quality data: defect or defect rate at each step (e.g., 64% quality rate in the manual soldering process as shown in Table 1); Cost data: labor cost, machine cost and the associated investment costs (as shown in Table 3 and Table 5). All of this information is essential to create a model that reflects the reality of the original production system before introducing improvements. Then, a detailed digital model of the PCB manufacturing process was created in the FlexSim environment (as shown in Figure 3). This step is the heart of the process, covering: Layout: Arrange the model of machines, workstations, buffers and conveyor systems to match the actual factory layout; Process Logic: Program or set the logic of each workstation, workpiece movement, process decisions and various working conditions, such as detailed simulation of the SMT process (workpiece feeding, inspection, soldering, cutting, cleaning, assembly, welding, transformer installation, screw and nut installation, labeling and quality control);

Parameter Input: Input the data collected in Step 1 into the model so that the model can work under the actual conditions of the original system. Then, when the model is completely created and configured, a simulation is performed to evaluate the performance of the current system and identify areas for improvement. This process includes running a Simulation: Simulate the operation of the production line under the current conditions for a specified period of time to collect performance data. Current Status Assessment: Analysis of the performance data of the manual soldering process before improvement (as shown in Table 1) showed relatively low efficiency, such as output of 471 pieces/day and quality rate of 64%, Solution Determination: Based on the analysis of bottlenecks and desired goals (as shown in Table 2), improvement solutions were developed, such as introducing a robotic automation system for the solder soldering process. Finally, the improvement approach obtained from the analysis was simulated to assess the potential impact before the actual investment. Post-improvement simulation: Create a new simulation model that reflects the proposed change, such as introducing 3 machines and 1 worker in the welding process (as shown in Table 3). Performance comparison: Compare the simulation results between the original system and the improved system by considering key indicators such as reduction in number of workers, cycle time, daily output, and cost (as shown in Table 4 Financial cost analysis: Conduct a comprehensive financial analysis (as shown in Table 5 and Table 6) using criteria such as net present value (NPV), internal rate of return (IRR), adjusted internal rate of return (MIRR), and discounted payback period to confirm the attractiveness of the investment and make a decision recommendation.
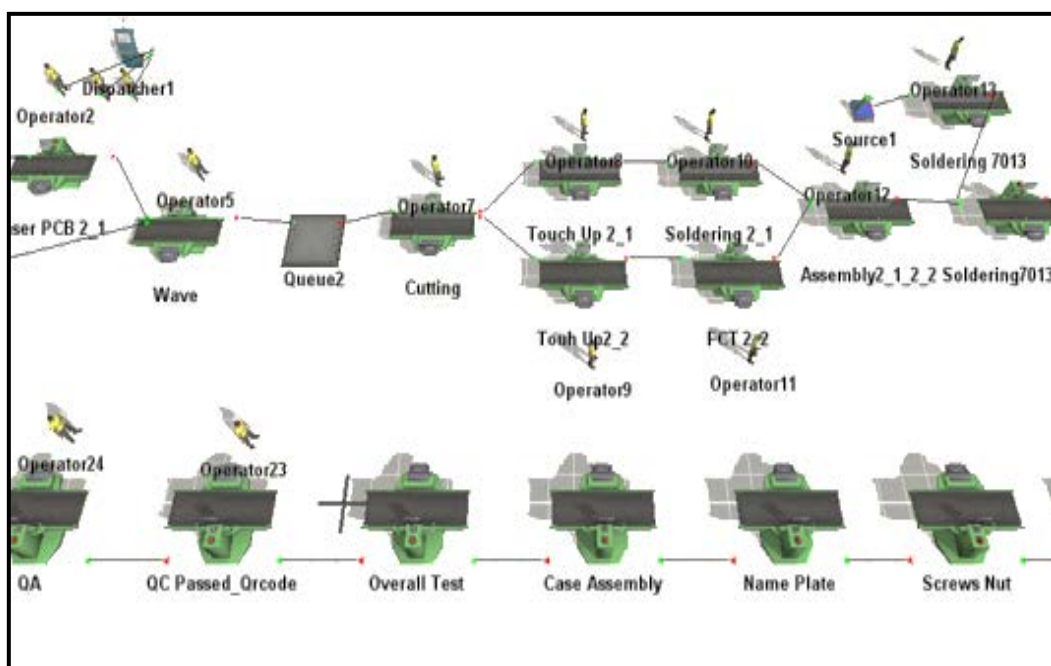
Figure 3 Show an analysis with FlexSim Platform.

Table 1 Manual soldering process: Before improvement.
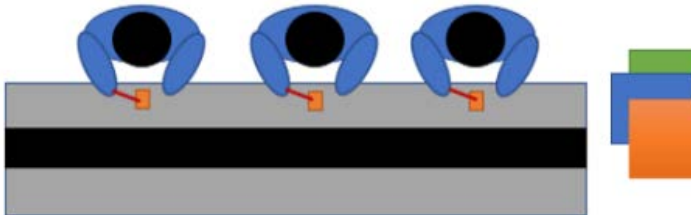
Before: Manual soldering process	
Number of workers	3
OEE	-
Cycle Time (second/pieces)	61.1
Takt Time	-
Capacity / Day (pieces)	741
Productivity (pieces)	471
Quality Rate (%)	64
Lay Out :	
Labor costs (1 employee 15,000 baht/person/month)	30,000-45,000

Table 2 Problems that need to be fixed and improved 5 topics.

Problems that need to be fixed and improved	
Labor	Reduce production costs (reduce workers)
Production capacity	Increase productivity
Quality	-
Technology	Welding robots are used in the production process.
Executive vision	Reduce bottlenecks

Table 3 An automated approach designed for entrepreneurs to make investment decisions.

Directions: Add 3 machines and 1 worker (to control the work)	
Number of workers	1
Number of machines (machine)	3
Cycle time (minute)	12.83
Productivity	797 pieces or 107.56%
Labor costs (15,000 baht/month/person)	15,000 baht/month, 180,000 baht/year
Machinery costs (500,000 baht/machine)	1,500,000 baht/year (excluding maintenance costs for the first year and maintenance cost 10 percent/year: approximately 150,000 baht)
Total net for first 1 year	1,680,000 baht/year
Investment cost (8 baht/circuit board)	6,376 baht/day, 127,520/month or 1,530,240 baht/year
Payback period	About 1 year 2 months

Table 4 Comparison table before and after improvements.

Comparison table before and after improvements		
	Before	After
Number of workers	3 persons	1 person + 3 machine
Cycle time	95 minutes	91 minutes
Productivity	64 %	107.56 %
Number of pieces/days	471	797
Machinery costs	–	1,500,000 baht
Labor costs	540,000 baht/year	180,000 baht/year
Labor cost + machinery	540,000 baht/year	1,680,000 baht/year
Investment cost	904,320 baht/year	1,530,240 baht/year
Profit/loss per year	364,320 baht/year	-149,760 baht/year
Estimates for the first year		
Payback period	7.17 month	1 year 2 months
There is no burden on machinery costs.		
Labor costs	540,000 baht/year	180,000 baht/year
Machine maintenance costs	–	150,000 baht/year
Labor/machinery costs	540,000 baht/year	330,000 baht/year
Investment cost	904,320 baht/year	1,530,240 baht/year
Profit/loss per year	364,320 baht/year	1,185,240 baht/year
Payback period	7.17 months	2.6 months

Table 5 Numerical data for deciding on investment in production improvement projects.

Project	Numerical data
Investment value	1,500,000 baht
Investment period	5 years
The cost of money or the minimum rate of return desired to be earned.	10%
NPV (Net Present Value)	11,514,525 baht
IRR (Internal Rate of Return)	87%
MIRR (Modify Internal Rate of Return)	61%
DPB (Discount Payback Period)	10 months

Table 6 Payback period calculation table

Payback Period Year	Cash Flow (baht)	Cumulative Cash Flow (baht)
0	(1,500,000)	(1,500,000)
1	1,800,338.20	300,338
2	1,636,671.09	1,937,009
3	1,487,882.81	3,424,892
4	1,352,620.74	4,777,513
5	1,229,655.21	6,007,168

RESULTS AND DISCUSSION

The results of the analysis are as follows: From Table 2 Show the primary challenges to be addressed are increasing production efficiency, reducing costs, and maintaining quality standards. This can be accomplished by integrating technology into the production process and optimizing various operational aspects. Aligning with management's vision, these

improvements will help alleviate production bottlenecks. From Table 3 Show an automated approach to manufacturing, designed to improve efficiency and reduce costs by introducing 3 machines and 1 worker to oversee the process, offers the following improvements are reduced labor is significantly reduced to just 1, leading to lower labor costs and increased productivity by the cycle time has been reduced to 12.83 minutes per piece, resulting in a productivity increase of 107.56% get output increases to 797 pieces. Whereas the initial investment in machinery is higher, amounting to 1.5 million baht. However, this is offset by reduced labor costs and increased productivity the estimated payback period for the investment is approximately 1 year and 2 months. Table 4, a comparison is shown between the manual soldering process before and after implementing automation. The workforce has been significantly reduced from 3 workers to 1, leading to significant labor cost savings. The cycle time has decreased from 95 minutes to 91 minutes, resulting in a significant productivity boost of 107.56%. The daily output has increased from 471 pieces to 797 pieces. However, the initial investment in machinery has increased the overall cost. While the initial investment is higher, the long-term benefits outweigh the costs. The automated process offers a faster payback period of 1 year and 2 months compared to the previous 7.17 months. From Table 5 This table presents quantitative data used to make investment decisions for production improvement projects. Investment Value: 1, 5 m baht the total amount of money required to invest in this project. Investment Period 5 years. The estimated timeframe for the return on investment. Cost of Money or minimum desired rate of return 10% the minimum expected rate of return from this investment. NPV (Net Present Value) 1.15 m baht. The net present value of the project, indicating its overall profitability. A positive NPV suggests a worthwhile investment. IRR (Internal Rate of Return) 87%. The internal rate of return of the project, which is the rate at which the net present value of the project becomes zero. The higher the IRR, the more attractive the investment. MIRR (Modified Internal Rate of Return) 61% An adjusted version of IRR that considers the reinvestment rate of cash flows. DPB (Discount Payback Period) 10 months. The time it takes for the project to recover its initial investment, considering the time value of money. From Table 6 Payback Period Calculation. This table shows the cash flow generated each year of the investment project and the cumulative cash flow. It is used to calculate the payback period of the project. In year 0, there is an initial investment of 1,500,000 baht, resulting in a negative cumulative cash flow. Subsequently, in years 1, 2, 3, 4, and 5, there is a continuous inflow of cash, causing the cumulative cash flow to gradually increase until it becomes positive. Based on the table, the project can within 1 year, as the cumulative cash flow becomes positive in the first year. This means that the initial investment in year 0 has been recovered.

The automation of the soldering process was a clear success, increasing productivity by 107% (from 471 to 797 pieces/day), reducing production time from 95 to 91 minutes/piece, and reducing the number of workers from 3 to 1. Despite the initial investment of 1.5 million baht, the project was able to achieve payback, within 1 year and 2 months and provided a satisfactory financial return (NPV of 1.15 million baht, IRR 87%), in line with the company's goal of increasing efficiency, reducing costs, and maintaining quality standards. This investment has proven to be worthwhile in the long run and can serve as a model for the development of other production processes.

CONCLUSIONS

The manual soldering process, as outlined in Table 1, was inefficient, labor-intensive, and prone to quality issues. The low productivity and high labor costs were significant concerns. To address these challenges, an automated approach was proposed. As detailed in Table 3, this approach involves introducing three machines and one worker to oversee the process. This automation significantly reduces labor costs, increases productivity, and improves product quality. The initial investment, though substantial, is offset by the long-term benefits. The financial analysis in Table 5 indicates a strong positive NPV, high IRR, and a short payback period, making the investment highly attractive. Table 6 further confirms the rapid payback period, with the initial investment recovered within a year. By implementing this automated solution, the company can enhance its manufacturing process, reduce costs, and improve overall efficiency.

ACKNOWLEDGEMENT

REFERENCES

1. Wu C, Arbor A. Part 5 human performance mathematical modeling and application in simulation. In: Handbook of Simulation Optimization. Cham: Springer; 2020. p. 483-534.

2. Bortolotti V, Abramo M. Optimization of a flexible assembly line using FlexSim. In: Advances in Production and Management Engineering. Singapore: Springer; 2022. p. 31-40.

3. Zhang Z, Liu Y. Application of FlexSim simulation technology in production scheduling. In: IOP

Conference: Materials Science and Engineering. IOP Publishing; 2021. p. 032043.

4. Jiang X, Zhang Y. Research on production scheduling optimization of flexible assembly line based on FlexSim. Journal of Physics: Conference Series. 2022;1968(1):012002.

5. Liu H, Wang J. Application of FlexSim simulation technology in logistics planning. In: IOP Conference Series: Materials Science and Engineering. IOP Publishing; 2023. p. 042001.

6. Rybicka J, Tiwari A, Enticott S. Testing a Flexible Manufacturing System Facility Production Capacity through Discrete Event Simulation: Automotive Case Study. International Journal of Mechanical, Aerospace, Industrial, Mechatronic and Manufacturing Engineering. 2016;10(4):668-72.

7. Devapriya P, Stumbled CTB, Bailey MD, Frazier S, Bulger J, Kemberling ST, et al. StratBAM: A Discrete-Event Simulation Model to Support Strategic Hospital Bed Capacity Decisions. J Med Syst. 2015; 39:130.

8. Pace D. Fidelity, Resolution, Accuracy, and Uncertainty. In: Loper M, editor. Modeling and Simulation in the Systems Engineering Life Cycle. Simulation Foundations, Methods and Applications. London: Springer; 2015. p. 29-37.

9. Zhang Z, Guan Z, Gong Y, Luo D, Yue L. Improved multi-fidelity simulation-based optimization: application in a digital twin shop floor. Int J Prod Res. 2022;60(3):1016-35.

10. Lee J, Kim S. Impact of Automation on Productivity and Quality in Electronics Manufacturing. J Manuf Syst. 2020;1-12:54. doi: 10.1016/j.jmsy.2019.12.003.

11. Garcia M. Payback Period and Risk Assessment in Manufacturing Automation. J Clean Prod. 2021;290:125732.

Prediction of the fatigue life of elevator wire rope using the Grey model GM (1,1)

Sittiphan Subcharoen, Pipat Pramot, Terdkiat Limpeteeprakarn, Apisit Muanmuang and Manusak Janthong[*]

Department of Mechanical Engineering, Faculty of Engineering, Rajamangala University of Technology Thanyaburi, Pathum Thani 12120, THAILAND

[*]Corresponding author: manusak.j@en.rmutt.ac.th

ABSTRACT

This article presents a tensile testing method for elevator wire ropes to predict fatigue life using the Grey GM (1,1) model, based on the relationship between applied force and the service life of the wire rope. The model is constructed from testing data where forces are applied to the wire rope until failure or damage occurs. A tensile testing machine for elevator wire ropes was designed and constructed, with a 5-meter-tall steel frame structure. At the top, a driving machine consisting of a 7.5-horsepower motor was installed to pull a wire rope with a diameter of 10 millimeters. One end of the wire rope is attached to the lift car, while the other is connected to the counterweight, enabling two-level vertical movement. The tensile force simulation involved adding masses of 350, 450, 550, and 650 kilograms, which moved up and down and stopped abruptly. The peak tensile forces recorded in the wire rope were 3.641, 4.845, 6.666, and 7.873 kilonewtons, respectively. The predicted fatigue life of the wire rope corresponding to these forces was 1,347,302; 927,853; 638,988; and 440,055 cycles. The results show that the fatigue life of the wire rope decreases as the tensile force increases. Predicting the fatigue life of wire ropes is crucial for inspection and quality assessment of elevator ropes. It allows for estimating wear over time in accordance with the Ministerial Regulation on Standards for Safety Management, Occupational Health, and Working Environment concerning Machinery, Cranes, and Boilers B.E. 2564 (2021).

Keywords: Wire rope, Predict the fatigue life, Wear and tear over time

INTRODUCTION

Wire ropes are essential equipment used for lifting or pulling heavy loads in various industrial applications, such as bridges, elevators, and mining hoists [1-3]. During operation, friction and wear issues arise due to differing contact conditions of the wire rope [4, 5], leading to changes in its properties. Damage may occur due to mechanical or environmental factors, or a combination of both [6, 7], which reduces performance and causes fractures [8, 9]. The complexity of wire rope wear accelerates its degradation [10].

Furthermore, deteriorating wire ropes exhibit increased elasticity, resulting in system vibrations during operation [11], posing safety hazards to users and workers [12]. Therefore, the efficiency and safety of the wire rope are critically important. Ensuring reliable elevator operation necessitates adherence to safety standards [13-15] relevant to wire rope usage. These standards cover requirements for design, testing, installation, and maintenance [16, 17], ensuring that wire ropes perform efficiently and safely.

For wire rope analysis techniques, Anil et al. [18] analyzed elevator wire rope using the Ansys program to identify best practices for managing wire rope to enhance safety and minimize elevator downtime due to rope failures. Yuanpei et al. [19] developed a finite element model of wire rope to study mechanical properties such as stress and strain, contributing to wire rope wear.

Bassir et al. [20] investigated the effects of corrosion on wire rope by immersing it in sulfuric acid and subjecting it to static traction tests to predict lifespan for maintenance planning. Yuxing [21] examined the friction and wear characteristics of fiber core wire rope (6x19+FC structure) under low-temperature environments, finding that the friction coefficient increased as ambient temperature decreased, peaking at 0.85 at -25°C, which could be mitigated by oil lubrication.

Zhen et al. [22] explored tribo-fatigue behavior by conducting bending fatigue tests on wire rope. Their study revealed that the rope's diameter decreased as bending fatigue increased, leading to damage and fractures. Xiangdong et al, [23] analyzed the sliding friction coefficient (COF), discovering that wire rope surface wear exhibited distinct patterns, including delamination, deep grooves, and plastic deformation. These effects were

significantly influenced by sliding speed, which also impacted the contact area of wire rope strands [24].

This study presents a tensile test of elevator wire rope to predict the forces acting within the wire rope. A Grey GM (1,1) model was developed to identify the relationship between force and the lifespan of the wire rope. This model aims to predict fatigue life from usage, which is crucial for inspecting and assessing the quality of elevator wire rope to ensure that elevators operate safely and efficiently.

MATERIALS AND METHODS

1. Structural design

The elevator wire rope tensile test machine's structural design consists of a steel framework, with a height of 5 meters. At the top, an elevator machine (driving machine) is installed, which includes a 7.5 horsepower motor used to pull the wire rope with a diameter of 10 millimeters. The ends of the wire rope are attached to both the lift car and the counterweight assembly, which moves up and down. There are two levels: the first level is 0.6 meters above the ground, the second level is 1.7 meters above the first, and the distance from the second level to the motor mount is 1 meter, as shown in Figure 1.
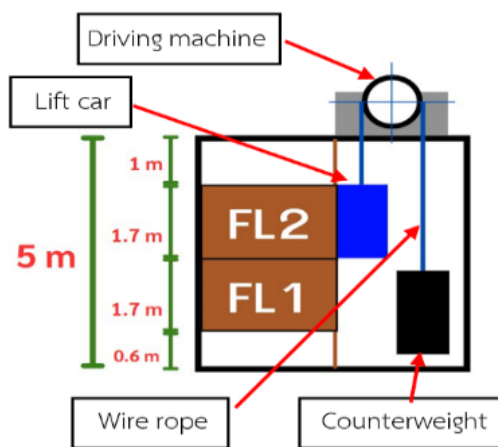
Figure 1 Structural design for testing the strength in the lift sling cable.

2. Control system

The design of the control system for the lift sling cable tensile testing machine is divided into two parts: the power circuit and the control circuit.

2.1 The power circuit consists of a fuse, which protects against short circuits and excessive current in the electrical circuit, connected to a magnetic contactor. A magnetic contactor is an electrical device that opens or closes an electrical circuit through magnetic control. It is used to control the operation of an electric motor. The motor used is an AC three-phase motor, which has advantages such as no brushes, resulting in low friction loss, high power

factor, low maintenance, easy startup, relatively constant speed, ease of construction, durability, low cost, and high efficiency, as shown in Figure 2.
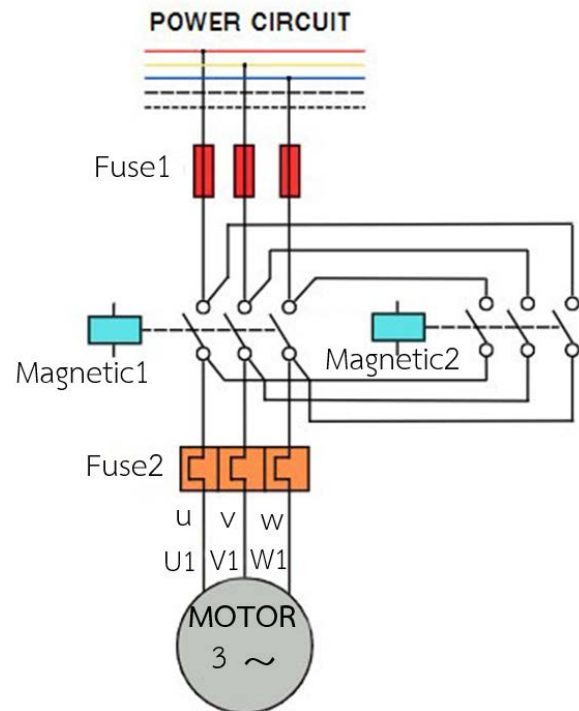
Figure 2 Motor power circuit.
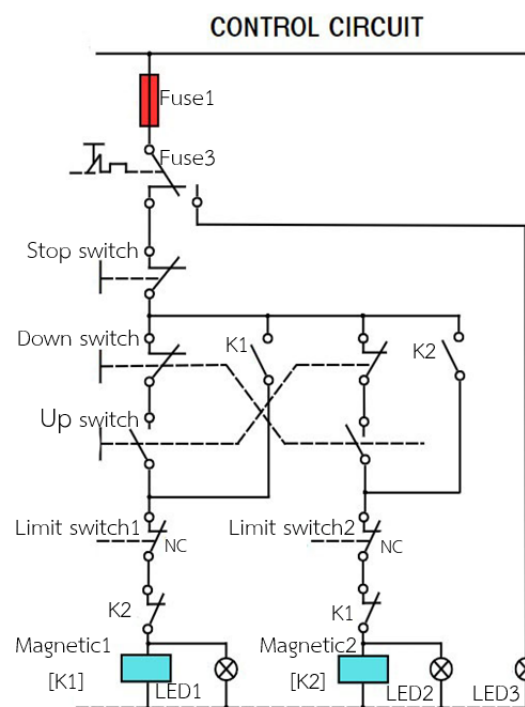
Figure 3 Motor Control Circuit.

2.2 The control circuit consists of a fuse that is connected to an overload relay (Overload Relay) to disconnect the control circuit. This is a protective device to prevent electrical equipment from exceeding its capacity or to protect the motor from damage when the current exceeds the rated load

capacity. It includes switches that command the lift to move in two directions: the up switch and the down switch. The movement will stop automatically due to the limit switches installed on each floor. However, in the event of an abnormality, a Stop switch will halt the operation for safety. The status of the operation is indicated by signal lights as shown in Figure 3.

3. Design of measurement systems

3.1 Circuit design measurement Strain refers to an object's deformation amount compared to its original size. It is a fundamental principle used to measure the strength of various materials, including checking the strength of the lift's wire rope. This ensures the safety and reliability of the lift system. A strain gauge measures the elongation or contraction of the lift's wire rope. It is attached to a metal bar placed between the wire rope and the lift cabin, as shown in Figure 4. When the motor pulls the wire rope, it causes strain on the metal bar, leading to a change in its shape, which also results in a change in the resistance of the strain gauge.
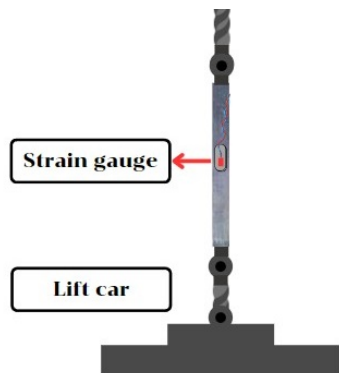
Figure 4 Attaching the strain gauge to the metal bar.

Test No.	Area mm²	Max. Load kN	Tensile strength N/ mm²	Yield point kN	Yield strength N/ mm²
1	81.00	38.71	477.95	26.18	323.21
2	122.72	63.55	571.85	63.24	515.36

Figure 5 Results of the tensile test on a steel bar.

A metal bar is used instead of a wire rope, since installing a strain gauge requires a smooth surface for accurate strain measurements, and the surface of a wire rope is not smooth, a metal bar is used instead. The metal bar must have properties that closely resemble the wire rope. The bar used has been tested for tensile strength, which is 477.95 Newtons per square millimeter, as shown in Figure 5. The wire rope used is a right-hand ordinary lay type with an 8×S (19) + FC construction, as shown in Figure 6. The tensile strength of the wire rope is 482.92 Newtons per square millimeter, as shown in Figure 7.
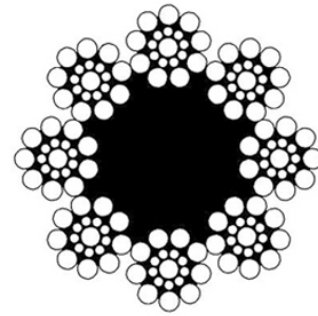

Figure 6 Helical characteristics of 8×S (19) + FC wire rope [25].

Test date : 10 February 2023

Test Temperature : 25 ℃

Testing machine : Universal Testing Machine INSTRON 5590-HVL

Table 1 the results of tensile test of SLING Size 10.45 mm

Specimen	T
Diameter (mm)	10.45
Cross sectional area (mm^2)	85.77
Maximum tensile load (kN)	41.42
Tensile strength (N/mm^2)	482.92

Figure 7 Results of the wire rope tensile test for Thailand Institute of Scientific and Technological Research (TISTR) Request No. R6600254.
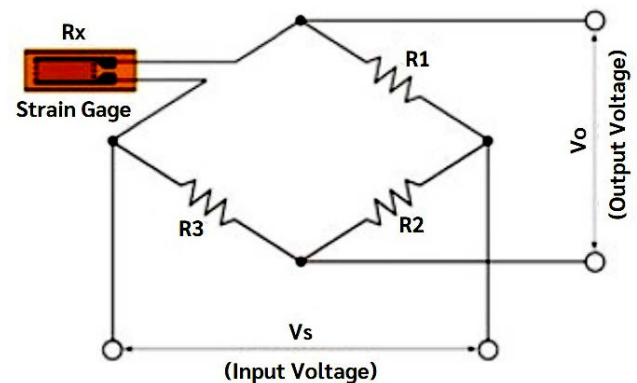
Figue 8 ¼ Wheatstone bridge circuit [26].

Measuring values from the strain gauge, to measure the values obtained from a strain gauge, a wheatstone bridge circuit is used [26] This circuit is designed to determine unknown resistance values by comparing them with standard known resistances. It is particularly effective in converting small changes in electrical resistance, as detected by the strain gauge, into an output voltage. The process involves supplying input voltage (referred to as excitation) to the circuit. The output voltage is then measured based on changes in resistance within the circuit. These changes are caused by the strain gauge's response to deformation. The resulting output is expressed in units of mV/V, as illustrated in Figure 8.

From Figure 8 the governing equation [27] can be derived as follows;

$$V_0 = \left(\frac{R_3}{R_1+R_3} - \frac{R_x}{R_2+R_x}\right)V_S \qquad (1)$$

By determining the stress value from the resistance relationship when specified. $R_x = F\varepsilon$ [28].

$$\varepsilon = \frac{4V_0}{V_{in}*A*F} \qquad (2)$$

When R_1 is Resistor 1

R_2 is Resistor 2

R_3 is Resistor 3

R_x is Strain gauge signal

ε is Strain

V_0 is Output voltage

V_s is Input voltage

F is Gauge factor

A is Strain gauge circuit amplifier gain

3.2 Specifications

The strain gauge used is the KFGS-5-120-C1-11 L1M2R model, which functions by changing the electrical resistance that occurs when the material to which the strain gauge is attached is stretched or compressed. As the metal stretches or contracts, the electrical resistance changes accordingly. This change in resistance can be converted into strain values using a Wheatstone bridge circuit, which has the following characteristics.
- Electrical resistance
- Gauge factor
- Input voltage
- Amplification rate of the strain gauge signal amplifier

3.3 Measurement system

The Wheatstone bridge circuit designed from Figure 8 is connected to the JY-S60 amplifier, which amplifies the signal as an analog signal. This signal is then sent to the NI myRIO for processing and recording results on a notebook computer, as shown in Figure 9.
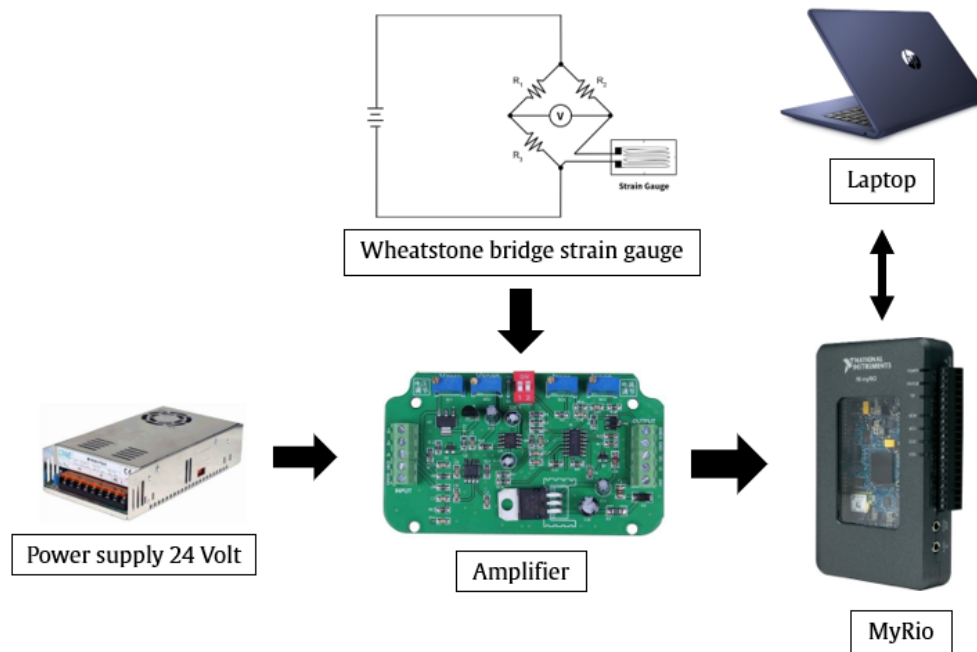
Figure 9 Measurement system equipment.

To ensure accurate prediction analysis, it is necessary to calibrate the strain gauge by applying masses of 300, 400, 500, and 600 kilograms to the lift car, which has a mass of 50 kilograms, as shown in Figure 10. The strain gauge readings in the form of voltage signals are presented in Table 1.

The values from Table 1 are plotted in a graph, as shown in Figure 11.

From Figure 11 a linear equation can be derived, which consists of the slope of the graph multiplied by the measured value, plus a constant. This linear equation should be implemented as a function in LabVIEW to convert the voltage readings into weight measurements.

3.4 The wire rope material used for securing and lifting.

The wire rope used for securing and lifting measurement equipment complies with the standards and requirements of ISO 4344 for passenger elevator applications. It meets the specified safety requirements and experimental conditions to simulate real operational scenarios. A pulley with a 10-millimeter groove diameter is used to securely hold the wire rope, ensuring firm adhesion and preventing slippage during sudden stops, as shown in Figure 12.

(a)

(b)

(c)

(d)

Figure 10 Calibration of the strain gauge with added mass in the lift car   300 kg (a), 400 kg (b), 500 kg (c), and 600 kg (d).

Table 1 Strain gauge calibration.

Voltage (Volts)	Mass (kilograms)			
	350	450	550	650
	1.406	1.660	2.095	2.354
	1.416	1.694	2.031	2.334
	1.440	1.694	2.065	2.295
Average	**1.421**	**1.683**	**2.064**	**2.328**
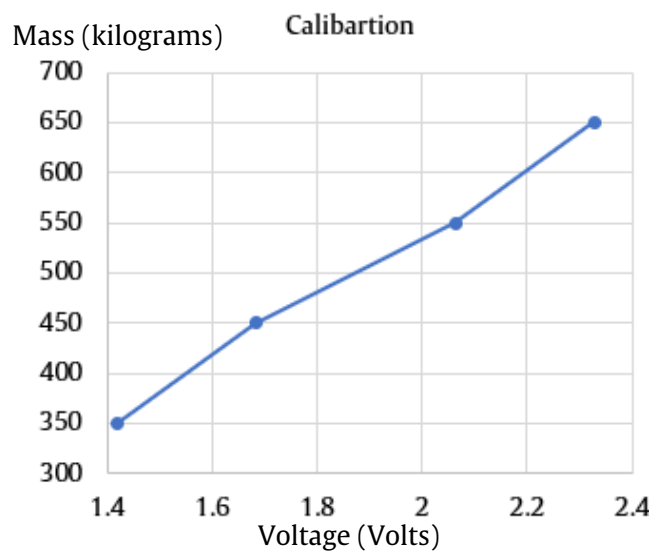
Figure 11 Strain gauge calibration.

Figure 12 Installation characteristics of the strain gauge, steel rod, and wire rope.

3.5 Testing method

In the test, the movement of the elevator will be controlled to oscillate vertically the same number of times, with a sudden stop at each instance. This is done to determine the maximum force exerted on the wire rope by measuring the strain on the material. A constant weight is added as a load applied during

testing. During the sudden stop, the elevator car carrying the weight will be halted at the midpoint of the elevator shaft to induce tension or shock force on the wire rope.

RESULTS AND DISCUSSION

1. Gray GM model (1.1) The Grey Model can process complex geometric structures, mechanical models, and external conditions that affect the fatigue lifespan of wire ropes. It helps reduce the difficulty in calculating reliable predictions of the wire rope's lifespan [29-32]. The traditional form of the GM (1,1) equation is defined as follows.

$$x^{(0)}(k) + az^{(1)}(k) = b \qquad (3)$$

Where $x^{(0)}(k)$ is the initial sequence, $x^{(1)}(k)$ is the first accumulated sequence, a is the developing coefficient, b is the gray action quantity, and $z^{(1)}(k)$ is the background value. This is achieved using the sequence of average values and calculating the derivative of the data sequence.

The values of a and b can be obtained using the least squares method for the GM (1,1) model as follows.

$$\begin{bmatrix} a \\ b \end{bmatrix} = (B^T B)^{-1} B^{TY} \qquad (4)$$

When

$$Y = \begin{bmatrix} x^{(0)}(2) \\ x^{(0)}(3) \\ \vdots \\ x^{(0)}(n) \end{bmatrix}, B = \begin{bmatrix} -z^{(1)}(2) & 1 \\ -z^{(1)}(3) & 1 \\ \vdots & \vdots \\ -z^{(1)}(3) & 1 \end{bmatrix} \qquad (5)$$

The calculation of the background value is fundamentally the area enclosed by the curve of the approximation and the axes, approximated using trapezoidal areas $x^{(1)}(t)$ along the x-axis $[k-1, k]$ and the y-axis t. Due to significant errors in this method, improvements have been made, and equation (5) is referred to as the whitenization equation. It can be rewritten as follows.

$$\int_{k-1}^{k} \frac{dx^{(1)}(k)}{dt} dt + a \int_{k-1}^{k} x^{(1)}(t)dt$$

$$= b \int_{k-1}^{k} (x^{(1)}(t))^{(2)} dt \qquad (6)$$

By rearranging the equation it can be expressed as follows.

$$x^{(0)}(k) + a \int_{k-1}^{k} x^{(1)}(t)dt$$
$$= b \int_{k-1}^{k} (x^{(1)}(t))^{(2)} dt \qquad (7)$$

Thus, the calculation $z^{(1)}(k)$ by solving the integral, the accuracy can be enhanced. $\int_{k-1}^{k} x^{(1)}(t)dt$ can enhance the accuracy of the background value estimation. This, in turn, improves the precision of predicting the fatigue life of the wire rope using the Grey Model GM (1,1). The Newton-Cotes formula is applied to compute the integral.

$$C = \frac{b-a}{90} [7f(x_0) + 32f(x_1) + 12f(x_2) + \dots$$
$$\dots + 32f(x_3) + 7f(x_4)] \qquad (8)$$

When $x_k = a + kh, h = (b-a)/4, a = k-1, b = k$ is applied, the background value is given by.

$$z^{(1)}(k) = C = \frac{b-a}{90} [7f(x_0) + 32f(x_1) + \dots$$
$$\dots + 12f(x_2) + 32f(x_3) + 7f(x_4)] \qquad (9)$$

The process of predicting the fatigue life of wire ropes under tensile force is arranged in ascending order. The GM (1,1) gray model is constructed based on the original sample age data of the wire rope from Table 2, which was obtained from testing the forces affecting the wire rope's usage. The values of a and b are determined to predict the next fatigue life.

Table 2 Experimental results on the service life of wire ropes from fatigue testing machine [33].

Tension load (kN)	N_A (cycle)
S = 15	57702
S = 20	34986
S = 25	32608
S = 30	25672

2. Experimental Results in this study a simulation of the tensile load on elevator wire ropes was conducted by increasing the mass to 350, 450, 550, and 650 kilograms, allowing vertical movement up and down and then stopping abruptly to record the maximum force exerted on the wire rope as shown in Table 3. The obtained force values were then used to predict the fatigue life of the wire rope using the Grey Model GM (1,1). The results indicate that as the tensile force applied to the wire rope increases, its fatigue life decreases accordingly. For example, when the tensile force values were 3.641, 4.845, 6.666, 7.873, 9.00, 10.00, and 15.00 kN, the predicted fatigue life cycles of the wire rope were 1,347,302, 927,853, 638,988, 440,055, 303,054,

208,689, and 143,740, respectively, as shown in Figure 13 and summarized in Table 4.

Table 3 Testing of maximum force generated from weight in each experiment.

Mass (kg)	Force Testing from Weight (N)				
	1	2	3	4	Average
350	3,503	3,639	3,693	3,729	3,641
450	4,879	4,744	4,924	4,834	4,845
550	6,706	6,796	6,503	6,661	6,666
650	8,059	7,833	7,856	7,743	7,873
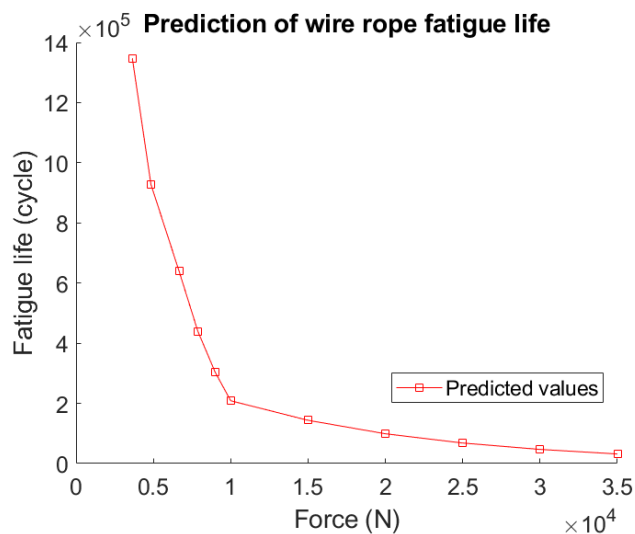
Figure 13 Prediction of wire rope fatigue life.

Table 4 Predicted Fatigue Life of Wire Rope under Tensile Load.

Tension (kN)	Fatigue life (cycle)
3.641	1,347,302
4.845	927,853
6.666	638,988
7.873	440,055
9.00	303,054
10.00	208,689
15.00	143,740

CONCLUSIONS

This research simulates the tensile load on elevator wire ropes by increasing the weight, moving up and down, and then stopping suddenly to determine the maximum force exerted on the wire rope during operation. The obtained data is used to predict the fatigue life of the wire rope. The study indicates that as the force applied to the wire rope increases, its fatigue life decreases [34-36]. Repeated tensile loading over a long period causes deterioration of the wire rope, requiring more frequent replacements.

When the wire rope reaches its lifespan limit, it may lead to damage [37-39]. From tensile tests with forces of 3.641, 4.845, 6.666, 7.873, 9.00, 10.00, and 15.00 kilonewtons, the corresponding fatigue lives of the wire rope were found to be 1,347,302; 927,853; 638,988; 440,055; 303,054; 208,689; and 143,740 cycles, respectively. It is essential to predict the lifespan of the wire rope in advance for maintenance planning. the wire rope is lifespan for maintenance planning or selecting an appropriate wire rope size. These measures must comply with the Ministerial Regulation on Safety Management, Occupational Health, and Working Environment for Machinery, Cranes, and Boilers, B.E. 2564 (2021) [40], as well as other relevant standards [41-43].

REFERENCES

1. Pal U, Mukhopadhyay G, Sharma A, Bhattacharya S. Failure analysis of wire rope of ladle crane in steel making shop. Int J Fatigue [Internet]. 2018; 116:149-55. Available from: http://dx.doi.org/ 10.1016/j.ijfatigue.2018.06.019.

2. Cao X, Wu W. The establishment of a mechanics model of multi-strand wire rope subjected to bending load with finite element simulation and experimental verification. Int J Mech Sci [Internet]. 2018;142-143:289-303. Available from: http://dx.doi.org/10.1016/j.ijmecsci. 2018.04.051.

3. Wang XY, Meng XB, Wang JX, Sun YH, Gao K. Mathematical modeling and geometric analysis for wire rope strands. Appl Math Model [Internet]. 2015;39(3-4):1019-32. Available from: http:// dx.doi.org/10.1016/j.apm.2014.07.015.

4. Zhang D, Feng C, Chen K, Wang D, Ni X. Effect of broken wire on bending fatigue characteristics of wire ropes. Int J Fatigue [Internet]. 2017;103: 456-65. Available from: http://dx.doi.org/10.1016/ j.ijfatigue.2017.06.024.

5. Wahid A, Mouhib N, Ouardi A, Sabah F, Chakir H, ELghorba M. Experimental prediction of wire rope damage by energy method. Eng Struct [Internet]. 2019;201(109794):109794. Available from: http://dx.doi.org/10.1016/j.engstruct.2019. 109794.

6. Chang XD, Huang HB, Peng YX, Li SX. Friction, wear and residual strength properties of steel

wire rope with different corrosion types. Wear [Internet]. 2020;458-9(203425):203425. Available from: http://dx.doi.org/10.1016/j.wear.2020.203425.

7. Battini D, Solazzi L, Lezzi AM, Clerici F, Donzella G. Prediction of steel wire rope fatigue life based on thermal measurements. Int J Mech Sci [Internet]. 2020;182(105761):105761. Available from: http://dx.doi.org/10.1016/j.ijmecsci.2020.105761.

8. Shu Q, Wang K, Yuan G, Zhang Y, Lu L, Liu Z. Assessing capacity of corroded angle members in steel structures based on experiment and simulation. Constr Build Mater [Internet]. 2020;244(118210):118210. Available from: http://dx.doi.org/10.1016/j.conbuildmat.2020.118210.

9. Li G, Hou C, Shen L, Yao GH. Performance and strength calculation of CFST columns with localized pitting corrosion damage. J Constr Steel Res [Internet]. 2022;188(107011):107011. Available from: http://dx.doi.org/10.1016/j.jcsr.2021.107011.

10. Xiang-dong C, Yu-xing P, Zhen-cai Z, Sheng-yong Z, Xian-sheng G, Chun-ming X. Effect of wear scar characteristics on the bearing capacity and fracture failure behavior of winding hoist wire rope. Tribol Int [Internet]. 2019;130:270-83. Available from: http://dx.doi.org/10.1016/j.triboint.2018.09.023.

11. Wu S, He P, Gong X. Analysis of transverse vibration of wire rope in flexible hoisting system. J Vibroengineering [Internet]. 2021;23(2):283-97. Available from: http://dx.doi.org/10.21595/jve.2020.21487.

12. Ray A, Dhua SK, Mishra KB, Jha S. Microstructural manifestations of fractured Z-profile steel wires on the outer layer of a failed locked coil wire rope. Pr Fail Anal [Internet]. 2003;3(4):51-5. Available from: http://dx.doi.org/10.1007/bf02715933.

13. Steel wire ropes for lifts - Minimum requirements: ISO 4344:2004(E). Geneva, Switzerland, 2004. Safety rules for the construction and installation of lifts-Part 1: Electric lifts. London: BSI Group; 2009.

14. Inspection Standard of Elevator, escalator and Dumbwaiter JIS A 4302-1992. Japan: Japanese Industrial Standard; 1992.

15. Thangavel D. Study of occupational health and safety: Elevator construction, mechanism, repairs, and reinstallations. SSRN Electron J [Internet]. 2023; Available from: http://dx.doi.org/10.2139/ssrn.4392601.

16. Wang W, Yang H, Chen Y, Huang X, Cao J, Zhang W. Motion analysis of wire rope maintenance device. Actuators [Internet]. 2023;12(10):392. Available from: http://dx.doi.org/10.3390/act12100392.

17. Babu Seelam A, Jawed MS, Hassan Krishanmurthy S. Design and analysis of elevator wire ropes. Int J Simul Multidiscip Des Optim [Internet]. 2021;12:20. Available from: http://dx.doi.org/10.1051/smdo/2021021.

18. Chen Y, Wang Q, Qin W, Xiang J. Study on the mechanical performance of a three-layered wire rope strand with a surface pit in varied corrosion direction into the wire. Eng Fail Anal [Internet]. 2022;136(106181):106181. Available from: http://dx.doi.org/10.1016/j.engfailanal.|2022.106181.

19. Youssef B, Meknassi M, Achraf W, Gugouch F, Lasfar S, Kane CSE, et al. The analysis of the corrosion effect on the wires of a 19*7 wire rope by two methods. Eng Fail Anal [Internet]. 2023;144(106816):106816. Available from: http://dx.doi.org/10.1016/j.engfailanal.2022.106816.

20. Peng Y, Wang G, Zhu Z, Chang X, Lu H, Tang W, et al. Effect of low temperature on tribological characteristics and wear mechanism of wire rope. Tribol Int [Internet]. 2021;164(107231):107231. Available from: http://dx.doi.org/10.1016/j.triboint.2021.107231.

21. Hu Z, Wang E, Jia F. Study on bending fatigue failure behaviors of end-fixed wire ropes. Eng Fail Anal [Internet]. 2022;135(106172):106172. Available from: http://dx.doi.org/10.1016/j.engfailanal.2022.106172.

22. Chang X, Peng Y, Zhu Z, Lu H, Tang W, Zhang X. Sliding friction and wear characteristics of wire rope contact with sheave under long-distance transmission conditions. Materials (Basel) [Internet]. 2022;15(20):7092. Available from: http://dx.doi.org/10.3390/ma15207092.

23. Peng Y, Huang K, Ma C, Zhu Z, Chang X, Lu H, et al. Friction and wear of multiple steel wires in a wire rope. Friction [Internet]. 2023;11(5):763-84. Available from: http://dx.doi.org/10.1007/s40544-022-0665-y.

24. Vordos N, Gkika D, Bandekas D. Wheatstone Bridge and Bioengineering. J Eng Sci Technol Rev [Internet]. 2020;13(5):4-6. Available from: http://dx.doi.org/10.25103/jestr.135.02.

25. General Purpose Rope 8×S (19)+ FC 8×W(19) + FC [Internet]. TAYMAX. [cited 2024 Sep 23]. Available from: http://www.taymax.co.th/product/general-purpose-rope-8xs-19-fc-8xw19-fc/?lang=th.

26. Oluwole OO, Olanipekun AT, Ajide OO. Design, construction and testing of a strain gauge instrument. International Journal of Scientific & Engineering Research. 2015;6(4):1825-9.

27. Zhao D, Gao C, Zhou Z, Liu S, Chen B, Gao J. Fatigue life prediction of the wire rope based on grey theory under small sample condition. Eng Fail Anal [Internet]. 2020;107(104237):104237. Available from: http://dx.doi.org/10.1016/j.engfailanal.2019.104237.

28. Zhao D, Liu YX, Ren XT, Gao JZ, Liu SG, Dong LQ, et al. Fatigue life prediction of wire rope based on grey particle filter method under small sample condition. Eksploat Niezawodn - Maint Reliab [Internet]. 2021;23(3):454-67. Available from: http://dx.doi.org/10.17531/ein.2021.3.6.

29. Lotfy HM, El-Shabasy AB, Attia TA, Hassan HA. Assessment of steel wire's fatigue life using finite elements modelling and experimental testing. IOP Conf Ser Mater Sci Eng [Internet]. 2020;973(1):012013. Available from: http://dx.doi.org/10.1088/1757-899x/973/1/012013.

30. Battini D, Solazzi L, Lezzi AM, Clerici F, Donzella G. Prediction of steel wire rope fatigue life based on thermal measurements. Int J Mech Sci [Internet]. 2020;182(105761):105761. Available from: http://dx.doi.org/10.1016/j.ijmecsci.2020.105761.

31. Ding P, Yang Q, Wang C, Wei X, Zhou Y. Application of improved grey model GM(1,1) in prediction of human health data. In: 2018 IEEE Third International Conference on Data Science in Cyberspace (DSC). IEEE; 2018.

32. Yang H, Gao M, Xiao Q. A novel fractional-order accumulation GMP(1,1) model and its application [Internet]. Research Square. 2022. Available from: http://dx.doi.org/10.21203/rs.3.rs-201981/v1.

33. Yılmaz O, İmrak CE. Discard fatigue life of stranded steel wire rope subjected to bending over sheave fatigue. Mech Ind [Internet]. 2017;18(2):223. Available from: https://doi.org/10.1051/meca/2016049.

34. Wang D, Wang B, Ge S, Wu K, Chong H, Zhang D, et al. Effects of fatigue load characteristics on bending tribo-corrosion-fatigue damage of steel wire ropes in seawater and pure water. Tribol Int [Internet]. 2025;201(110201):110201. Available from: http://dx.doi.org/10.1016/j.triboint.2024.110201.

35. Li C, Wang D, Sun Y, Xu W, Zhang J, Wu K, et al. Bending fatigue damage behavior of wire rope in hoisting system of drilling rig. Tribol Int [Internet]. 2023;187(108745):108745. Available from: http://dx.doi.org/10.1016/j.triboint.2023.108745.

36. Huang K, Peng Y, Chang X, Zhou Z, Jiang G, Lu H, et al. Fretting fatigue behavior of helical-torsional contact steel wire in wire rope. Int J Fatigue [Internet]. 2024;186(108393):108393. Available from: http://dx.doi.org/10.1016/j.ijfatigue.2024.108393.

37. Yang H, Gao M, Xiao Q. A novel fractional-order accumulation GMP(1,1) model and its application [Internet]. Research Square. 2022; Available from: http://dx.doi.org/10.21203/rs.3.rs-201981/v1.

38. Wang H, Zheng H, Tian J, He H, Ji Z, He X. Research on quantitative identification method for wire rope wire breakage damage signals based on multi-decomposition information fusion. Journal of Safety and Sustainability [Internet]. 2024;1(2):89-97. Available from: http://dx.doi.org/10.1016/j.jsasus.2024.02.001.

39. Wang D, Wang B, Ge S, Wu K, Chong H, Zhang D, et al. Effects of fatigue load characteristics on bending tribo-corrosion-fatigue damage of steel wire ropes in seawater and pure water. Tribol Int [Internet]. 2025;201(110201):110201. Available from: http://dx.doi.org/10.1016/j.triboint.2024.110201.

40. Ministerial regulation prescribing standards for the management and operations concerning safety, Occupational Health, and Working Environment related to Machinery, Cranes, and Boilers, B.E. 2564 (2021). (2021, August 6). Royal Gazette; Volume 138 (Part 52 A), p. 3-29.

41. The British Standards. Safety rules for the construction and installation of lifts - Part 1: Electric Lifts [Internet]. 2009. Available from: https://nobelcert.com/DataFiles/FreeUpload/EN%2081-22-2014.pdf.

42. Japanese Industrial Standard. Inspection standard of elevator, escalator and dumbwaiter JIS A 4302-1992 [Internet]. 1992. Available from: https://www.stdlink.com/standards/jis-a-4302-1992.html.

43. The British Standards. Safety rules for the construction and installation of lifts - Lifts for the transport of persons and goods Part 20: Passenger and goods passenger lifts [Internet]. 2014. Available from: https://nobelcert.com/DataFiles/FreeUpload/EN%2081-20-2014.pdf.

The study of relationship between compressive strength and expansion of alkali silica reaction and/or delayed ettringite formation with the use of fly ash

Thanadet Sriprasong[1], Phakkhaphum Lethaisong[2] and Vinita Khum-in[1*]

[1]Department of Civil Engineering, Faculty of Engineering, Rajamangala University of Technology Thanyaburi, Pathum Thani 12110, THAILAND

[2]Scientific Instrument and Technological Transfer Center, Faculty of Applied Science, King'Mongkut University Technology North Bangkok, Bangkok 10800, THAILAND

*Corresponding author: vinita.k@en.rmutt.ac.th

ABSTRACT

Mass concrete structures that have been deteriorated are typically attributed to shrinkage or thermal deformation. However, there is another type of cracking that has been found whose crack patterns have been considered to be the result of alkali-silica reaction (ASR) and/or delayed ettringite formation (DEF) that occurred in heat-steam cured in massive concrete structures when the initial temperature during the hydration process exceeds 70 °C. It is generally believed that fly ash has played an important role in increasing the durability in concrete. This study investigates the effects of fly ash on the compressive strength and expansion of mortar specimens subjected to ASR and/or DEF and water absorption in mortar specimens. Mortar samples were prepared using Portland cement Type III with 20% replacement of Class F fly ash, some specimens contained reactive aggregates as silica sand through a replacement of 30 wt% of river sand. Sodium sulfate was added (4%wt SO_3 addition). Some specimens were exposed to an elevated temperature curing at early age to induce ASR and accelerate DEF. Compressive strength and length change were measured over 200 days. Results indicate that fly ash effectively mitigated ASR expansion but had a limited impact on DEF. Samples exposed to both ASR and DEF conditions exhibited essential expansion and rapid reduction of compressive strength when reactive aggregate and sodium sulfate were used. This research provides insights into the complex interactions between fly ash, ASR, and DEF in cementitious systems, with implications for improving concrete durability in aggressive environments.

Keywords: Fly ash, Alkali-silica reaction, Delayed ettringite formation, Compressive strength, Expansion

INTRODUCTION

Concrete is one of the most widely used construction materials worldwide due to its versatility, strength, and relatively low cost. However, the long-term durability of concrete structures can be compromised by various degradation mechanisms, including alkali-silica reaction (ASR) and delayed ettringite formation (DEF) as shown in the bridge foundation in Thailand shown in Figure 1. These phenomena can lead to expansive reactions within the concrete matrix, resulting in cracking, loss of strength, and ultimately, reduced service life of structures [1].

ASR is a complex chemical process between reactive silica in aggregates and alkali hydroxides in the concrete pore solution. The reaction produces an expansive gel that can lead to cracking and deterioration of concrete structures[2]. The mechanism of ASR involves the dissolution of silica by hydroxyl ions,

followed by the formation of an alkali-silica gel that absorbs water and expands [3]. Recent studies have focused on the role of calcium in the ASR mechanism. Gaboriaud et al. (1999) proposed that calcium plays a crucial role in forming expansive products, suggesting that the interaction between calcium and the alkali-silica gel is essential for understanding ASR kinetics [4]. This finding has implications for using supplementary cementitious materials like fly ash, which can modify the calcium content in the pore solution. Various factors, including the reactivity of aggregates, alkali content of cement, environmental conditions, and the presence of supplementary cementitious materials influence the progression of ASR. Lindgard et al. (2012) conducted a comprehensive review of factors affecting ASR in concrete, highlighting the complex interplay between material properties and environmental conditions [5].

Figure 1 Cracking of the bridge foundation in Thailand.

DEF, conversely, is associated with the decomposition and subsequent reformation of ettringite in concrete subjected to high curing temperatures, leading to expansion and cracking in mature concrete [6]. The mechanism of DEF involves the decomposition of ettringite at temperatures higher than 70 °C, the incorporation of sulfate ions into the C-S-H gel, and the gradual release of these sulfates over time, leading to the delayed formation of ettringite in the hardened concrete matrix [7]. Recent research by Brunetaud et al. (2007) has provided insights into the kinetics of DEF, demonstrating that the expansion process occurs in three phases: induction, acceleration, and stabilization [8]. The factors influencing DEF include curing temperature, cement composition (particularly C_3A and sulfate content), and exposure conditions. Ramlochan et al. (2003) investigated the effect of supplementary cementing materials on DEF, finding that their effectiveness depends on both chemical and physical factors [9].

However, ASR and DEF have been extensively studied individually, their potential interaction in concrete systems is less well understood. Bérubé et al. (2002) investigated the combined effects of ASR and DEF, suggesting that the presence of one mechanism may influence the development of the other [10]. They observed that concrete affected by both ASR and DEF exhibited more severe deterioration than concrete affected by either mechanism alone. Recent work by Sriprasong et al. (2020) has shed light on the synergistic effects of ASR and DEF, demonstrating that the presence of ASR can accelerate the onset of DEF expansion [11]. This finding highlights the importance of considering multiple degradation mechanisms when assessing concrete durability.

Using supplementary cementitious materials (SCMs) such as fly ash has been widely recognized as an effective method to mitigate ASR in concrete [12]. Fly ash, a by-product of coal combustion in power plants, is known to reduce the available alkalis in the pore solution and modify the composition of the calcium silicate hydrate (C-S-H) gel, thereby limiting the potential for expansive reactions [13]. While the effects of fly ash on ASR have been extensively studied, its impact on DEF and the potential interaction between

ASR and DEF in the presence of fly ash are less well understood. This knowledge gap is particularly significant given that concrete structures may be simultaneously exposed to conditions that promote both ASR and DEF, such as in mass concrete elements or precast concrete products subjected to heat treatment [9]. Recent research by Owsiak (2010) has explored the combined effects of fly ash on both ASR and DEF, suggesting that the optimal fly ash content for mitigating both mechanisms may differ from that required for ASR alone[14]. This finding underscores the need for further investigation into the role of fly ash in complex degradation scenarios.

The present study aims to investigate the relationship between compressive strength and expansion in mortar specimens subjected to conditions promoting ASR and/or DEF, focusing on the mitigating effects of fly ash. By examining various combinations of reactive aggregates, sulfate addition, and high-temperature curing, this research provides a comprehensive understanding of the complex interactions between these degradation mechanisms and the role of fly ash in enhancing concrete durability. The significance of this study lies in its potential to inform the development of more resilient concrete mixtures capable of withstanding multiple degradation mechanisms. As infrastructure ages and environmental conditions become more aggressive due to climate change, the need for durable concrete that can resist both ASR and DEF becomes increasingly critical [15].

This research addresses the effect of fly ash in mitigating ASR and DEF and its combination in different situations on expansion and attendant damage in mortar, focusing on the influence of SO_3 with chemicals to add sulphate ions to the pore solution. Fine reactive aggregates (silica sand) were used to initiate ASR. The internal damage due to the expansion was characterized by correlation with the compressive strength. Hence, ASR and DEF are consistently examined, combining high temperature at early ages, addition of alkali sulphates, and reactive aggregate. In this study, High-early-strength Portland cement type III (HPC) is used, which is often used in laboratory test because it has a higher C_3A, which could accelerate ASR due to a higher alkali, while high SO_3 in HPC has an effect to DEF. It is generally believed that using fly ash reduces the alkalies in cement, which means it can inhibit the risk of ASR and possibly also the risk of DEF.

MATERIALS AND METHODS

Research design

This study employs a quantitative experimental design to investigate the effects of fly ash on the compressive strength and expansion of mortar specimens subjected to conditions promoting alkali-silica reaction (ASR) and/or delayed ettringite formation

(DEF). The research design allows for systematically manipulating key variables, including aggregate reactivity, sulfate content, and curing temperature, to isolate and examine the individual and combined effects of ASR and DEF.

Materials

Porland Cement: Type III (HPC) conforming to ASTM C150 was used as the primary binder. The chemical composition of HPC is given in Table1. Type III cement was chosen due to its higher early strength and heat of hydration, which can accelerate ASR and DEF processes, allowing for the observation of these phenomena within the study timeframe.

Table1 The chemical composition of the Portland Cement type III used in this study.

Chemical composition	%by weight
Calcium Oxide (CaO)	65.07
Silicon Dioxide (SiO$_2$)	20.74
Aluminum Oxide (Al$_2$O$_3$)	5.03
Iron Oxide (Fe$_2$O$_3$)	3.02
Magnesium Oxide (MgO)	2.78
Titanium Dioxide (TiO$_2$)	0.18
Sulphur Trioxide (SO$_3$)	1.95
Potassium Oxide (K$_2$O)	0.18
Sodium Oxide (Na$_2$O)	0.35
Loss on Ignition (ig. loss)	0.7

Fly Ash: Shehata and Thomas (2000) suggested that fly ash could mitigate ASR, especially fly ash with class F [12]. Thus, fly ash from the BLCP Power Plant in Rayong, Thailand, which was class F, similar to the report of Shehata and Thomas (2000) was used as a partial replacement for cement.

Aggregates: This study used two types of fine aggregates: 1) Natural river sand passing through a No.50 sieve (0.30 mm opening) as the non-reactive aggregate. 2) Reactive silica sand passing through a No.60 sieve (0.25 mm opening) was used to promote ASR.

Chemical Admixtures: Sodium sulfate (Na$_2$SO$_4$) was used to increase the sulfate content in selected mixtures, promoting DEF as per the methodology described [9]. In a previous study, Escadeillas et al. (2007) [16] and Zhang et al. (2002a) [17] suggested

that high SO$_3$ content in cement and SO$_3$/Al$_2$O$_3$ molar ratio could be a significant factor for DEF. In the absence of SO$_3$, there can be no ettringite. However, ettringite (not monosulphate) can be present at the end of the heat treatment in the presence of much SO$_3$. On the other hand, in the absence of Al$_2$O$_3$, ettringite is not present again. However, if Al$_2$O$_3$ is higher, monosulphate (not ettringite) can be present. Taylor et al. (2001) indicated that the pessimum of SO$_3$ is trending to increase with the content of Al$_2$O$_3$; thus, this will suggest a pessimum of the SO$_3$ / Al$_2$O$_3$ ratio [7]. Zhang et al. (2002b) have studied the expansions for the mortar specimens made from SO$_3$ / Al$_2$O$_3$ molar ratios in the range between 0.80-1.40 [18]. The results indicate that the maximum expansion occurs with the molar ratio of about 1.00, and no expansion was observed when the molar ratio is lower 0.80. Zhang et al. (2002b)'s also defined a DEF Index for the expansion as shown in Eqn. 1-1 and suggested that there is no expansion when DEF index (calculated from Eqn. 1-1) is lower than 1.1 while the expansion can be observed when DEF index is above 1.1 [18].

Eqn.1-1

$$\mathbf{DEFIndex} = \left(\frac{SO_3}{Al_2O_3}\right)_a \times \left[\frac{(SO_3+C_3A)_b}{10}\right] \times \sqrt{Na_2O_{eq}}$$

where; (SO$_3$ / Al$_2$O$_3$)$_a$ is the molar ratio of SO$_3$ to Al$_2$O$_3$ of the cement,
(SO$_3$ + C$_3$A)$_b$ is the combination of SO$_3$ and C$_3$A %wt in the cement
$\sqrt{Na_2O_{eq}}$ is the square root of Na$_2$O$_{eq}$ %wt in the cement.

Mixture proportions

The amount of water can be found according to the flow table test method (ASTM C230/C230M). The flow test result suggests the water-to-cement ratio is equal to 0.83 Six mortar mixtures were prepared with a water-to-binder (cement + fly ash) ratio of 0.83. The mixture proportions are detailed in Table 2. The mixture IDs are interpreted as follows: FA contains fly ash, NS is no sulfate addition, S is sulfate addition, NR is no reactive aggregate, R contains reactive aggregate (silica sand), T cured at room temperature, and 90 subjected to 90°C heat treatment.

Table 2 Mortar Mixture Proportions.

Mixture ID	Cement (%)	Fly Ash (%)	River Sand (%)	Silica sand (%)	Na$_2$SO$_4$ (% of cement weight)
FA_NSR_T	80	20	70	30	0
FA_NSR_90	80	20	70	30	0
FA_SNR_T	80	20	100	0	4
FA_SNR_90	80	20	100	0	4
FA_SR_T	80	20	70	30	4
FA_SR_90	80	20	70	30	4

Specimen preparation

Mortar specimens were prepared according to ASTM C109 for compressive strength testing (50 mm cubes) and ASTM C1260 for expansion testing (25x25x285 mm prisms). The mixing procedure followed ASTM C305.

Curing regimes

In order to accelerate the DEF effectively, the temperature history was adapted based on the work of Famy (1999) and Famy et al. (2001) as shown in Figure 2. A set of specimens suffixed by_90 were cured for four hours under sealed conditions at 30 °C soon after casting, and then exposed to 90 C for twelve hours with a temperature gradient of 30 °C/hr. Subsequently, the temperature was gradually reduced to 30 °C over four hours, the specimens were kept at 30 °C for another two hours, and finally the seal and mould of the specimens were removed. Another set of specimens, suffixed by _T, were cured at 30±2 °C (room temperature) for twenty-four hours under sealed conditions.
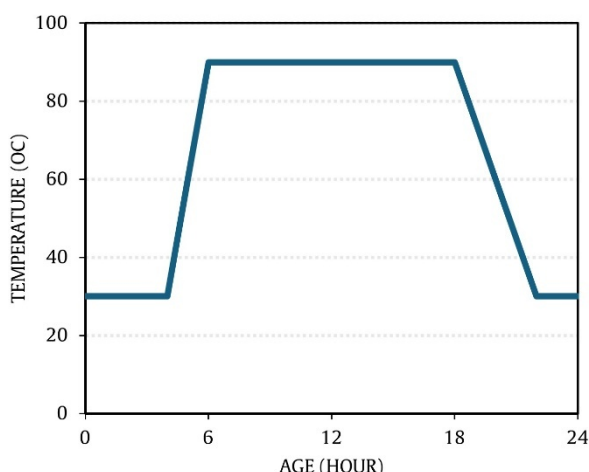
Figure 2 Curing regimes at early age to accelerate DEF.

After the initial curing period, all specimens were submerged in water at 30 ± 2°C, As the DEF expansion rate may be retarded when the pH in the pore solution rises due to leaching [19, 20] the water used to submerge the specimens needs to be changed every four weeks.

Testing procedures

Expansion measurements: length change measurements were conducted on mortar prisms at 7, 14, 28, 56, 100, 150, and 200 days using a digital length comparator with a precision of 0.001 mm, following the procedure outlined in ASTM C1260.

Compressive strength testing: compressive strength tests were performed on mortar cubes at 7, 14, 28, 56, 100, 150, and 200 days using a hydraulic press under ASTM C109.

Data analysis: The results are reported by averaging the measured values of three specimens for each type of mix proportion and curing condition. The expansion and compressive strength data were analyzed using descriptive statistics and graphical methods to identify trends and relationships. The effects of fly ash, sulfate addition, reactive aggregates, and curing temperature on expansion and strength development were evaluated by comparing the different mixture designs. The relationship between expansion and compressive strength was examined using regression analysis to test the hypothesis of a non-linear relationship and to identify potential threshold values for critical expansion related to the higher expansion that might occur when the compressive strength is suddenly reduced.

RESULTS AND DISCUSSION

1. Results

1.1 Expansion measurements
The expansion measurements for all mortar mixtures over the 200-day test period are presented in Figure 3.
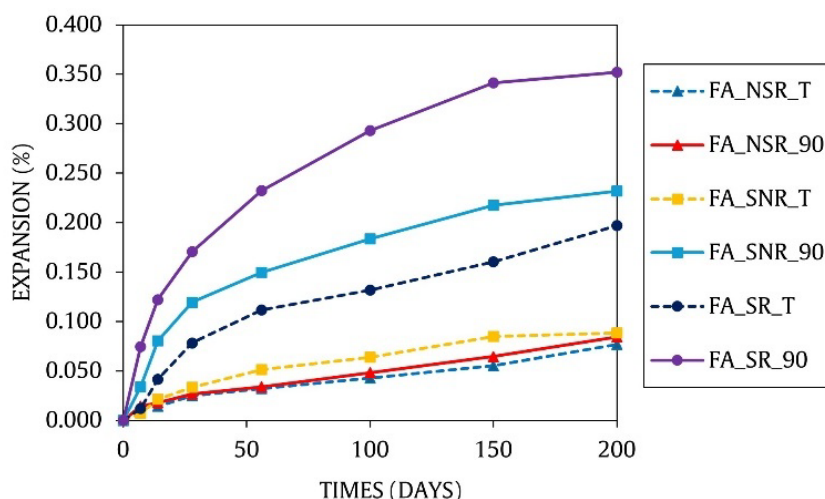
Figure 3 Expansion of mortar specimens over time.

The expansion results reveal several key trends as follows: 1) mixtures subjected to high-temperature curing (90°C) consistently showed higher expansion compared to their room-temperature counterparts, 2) the addition of sodium sulfate resulted in increased expansion, particularly when combined with high-temperature curing, 3) mixtures containing reactive aggregates (R) exhibited higher expansion than those without, indicating the occurrence of ASR, 4) the combination of reactive aggregates, sulfate addition, and high-temperature curing (FA_SR_90) produced the highest expansion, reaching 0.352% at 200 days, and 5) mixtures without reactive aggregates or sulfate addition (FA_NSR_T and FA_NSR_90) showed the lowest expansion, suggesting that fly ash was effective in mitigating ASR when other promoting factors were absent.

1.2 Compressive strength results

The compressive strength results for all mortar mixtures over the 200-day test period are presented in Figure 4.
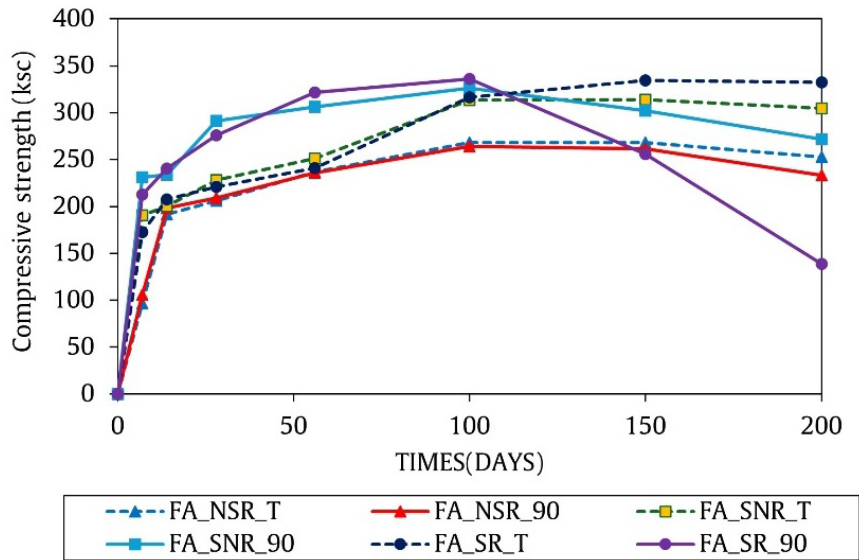
Figure 4 Compressive strength of mortar specimens over time.
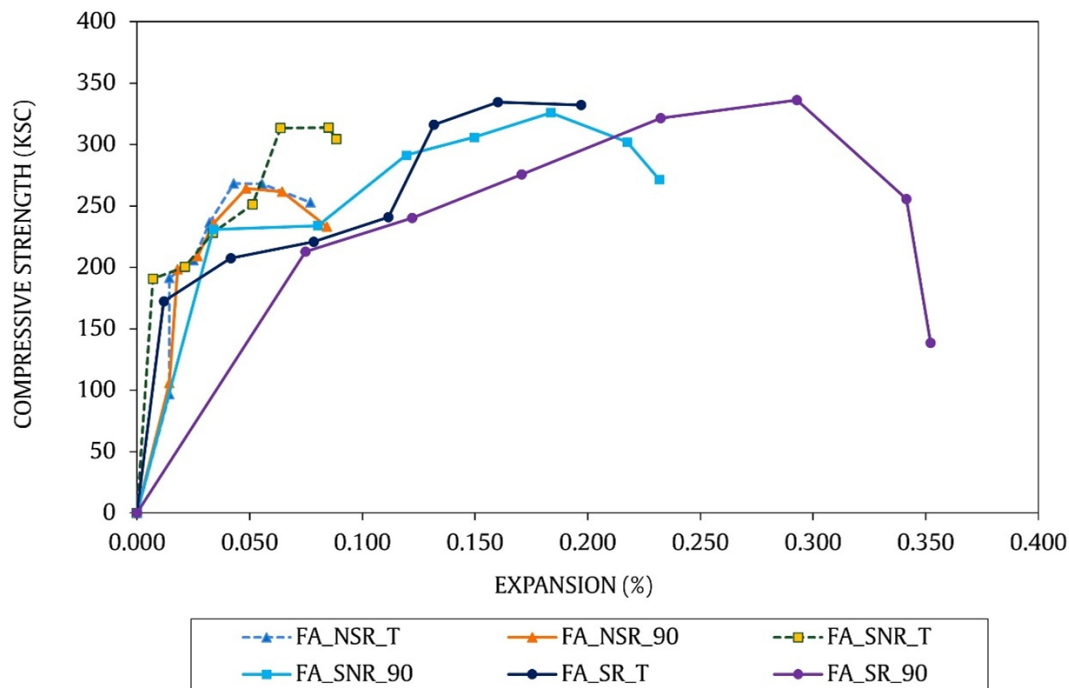
Figure 5 Relationship between expansion and compressive strength.

The compressive strength results reveal the following trends: 1) most mixtures showed an increase in strength up to 100 days, followed by a plateau or decline, 2) mixtures subjected to high-temperature curing initially developed higher strengths but showed more pronounced strength loss at later ages, 3) the addition of sodium sulfate (S) resulted in higher early-age strength but led to more significant strength loss

over time, particularly when combined with high-temperature curing, 4) the mixture with both ASR and DEF promoting factors (FA_SR_90) exhibited the most dramatic strength loss, dropping from a peak of 32.94 MPa at 100 days to 13.60 MPa at 200 days, and 5) mixtures without reactive aggregates or sulfate addition (FA_NSR_T and FA_NSR_90) maintained relatively stable strength throughout the test period.

1.2 Relationship Between Expansion and Compressive Strength

The relationship between expansion and compressive strength for all mixtures is illustrated in Figure 5 Key observations from this analysis include:

• A general inverse relationship between expansion and compressive strength is evident, with higher expansion associated with lower strength.

• The relationship appears non-linear, with a more rapid decline in strength observed beyond an expansion threshold of approximately 0.10%.

• Mixtures subjected to both ASR and DEF-promoting conditions (FA_SR_90) show the most pronounced negative correlation between expansion and strength loss.

• Mixtures with only fly ash and no promoting factors for ASR or DEF (FA_NSR_T and FA_NSR_90) exhibit minimal expansion and maintain relatively stable strength.

These results provide insights into the complex interactions between fly ash, ASR, and DEF, and their combined effects on mortar expansion and strength development. These findings have implications for understanding the durability of cementitious systems exposed to multiple degradation mechanisms and the role of fly ash in mitigating these effects.

2. Discussion

The results of this study provide valuable insights into the complex interactions between fly ash, alkali-silica reaction (ASR), and delayed ettringite

formation (DEF) in cementitious systems. The following discussion interprets these findings in the context of the research questions and existing literature.

2.1 Effectiveness of Fly Ash in Mitigating ASR and DEF

The expansion results demonstrate that fly ash effectively mitigated ASR expansion, particularly without other promoting factors. This is evident in the low expansion values observed for mixtures FA_NSR_T and FA_NSR_90, which contained fly ash but no reactive aggregates or added sulfates. This finding is consistent with previous research [12]. who reported significant reductions in ASR expansion with fly ash. The ASR detection via ASR detection kit, as shown in Figure 6, suggests a tiny amount of ASR gel (green gel) around the reactive aggregate (red aggregate).
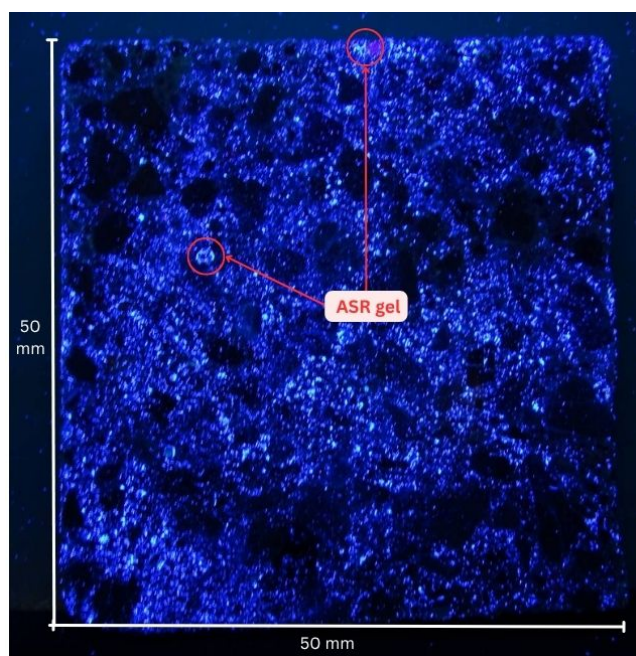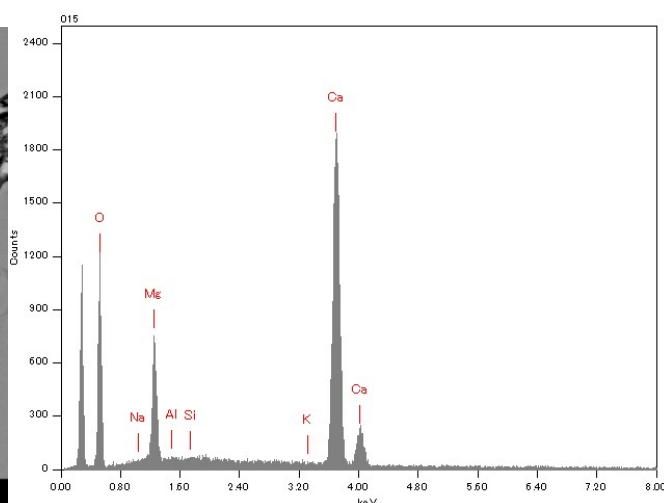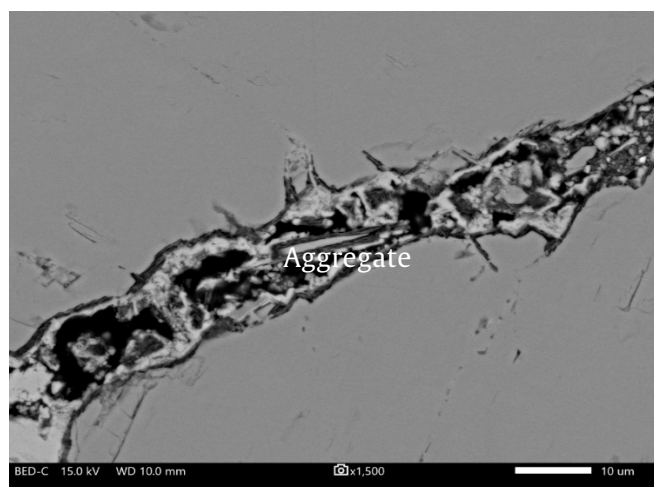

Figure 6 ASR Detection of mortar specimens.

Figure 7 Left: Backscattered electron image (cracks inside aggregate) Right: Results of qualitative analysis using EDS.
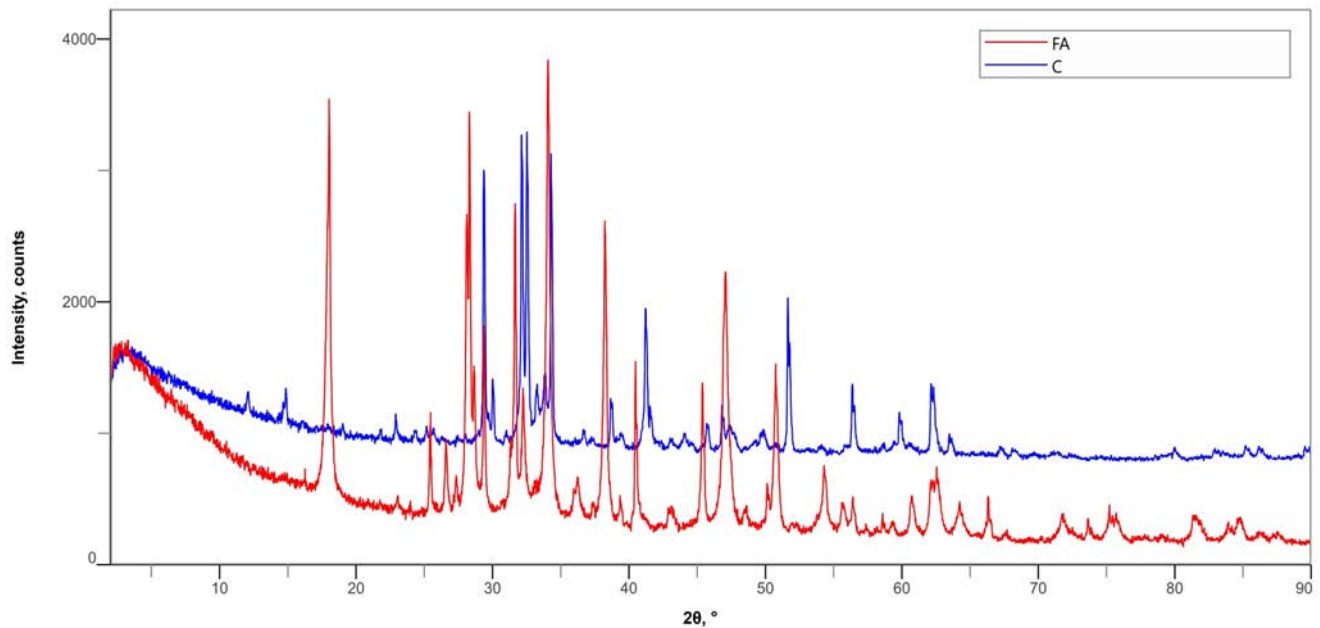
Figure 8 XRD Analysis.

However, the effectiveness of fly ash in mitigating DEF-induced expansion appears to be more limited. Despite fly ash, mixtures containing added sulfates (FA_SNR_T and FA_SNR_90) exhibited higher expansion than their non-sulfate counterparts. This observation aligns with Ramlochan et al. (2003) [9], who noted that higher quantities of fly ash might be necessary to mitigate DEF compared to ASR effectively. The results suggest that while the 20% fly ash replacement used in this study was beneficial in reducing ASR expansion, it may not have significantly mitigated DEF under the aggressive conditions created by sulfate addition and high-temperature curing. This highlights the importance of considering the specific degradation mechanisms and exposure conditions when determining optimal fly ash content for durability.

Moreover, there is no gaps around the aggregate which it possibly suggests to ettringite or cracks in the cement paste. At the same time, the EDS analysis also indicated that there is low silica (Si) in the specimens, which can ensure that fly ash could reduce the occurrence of ASR according to Figure 7 that were observed by polarizing microscope by SEM-EDS analysis. Figure 8 shows a specimen containing fly ash (red line) and a specimen without the replacement of fly ash (blue line). The position (2θ angles) and intensities of the peak provide information about the spacing between the lattice planes and the abundance of different crystallographic forms present in the sample, which means the specimens that contain fly ash could have a higher percent crystallinity and also a higher crystal perfection according to a peak width. From this perspective, it can be suggested that the higher compressive strength and lower expansion have occurred due to fly ash, which led to a gap fulfillment before the occurrence of ASR.

2.2 Relative Contributions of ASR and DEF to Expansion and Strength Loss

The expansion and strength data reveal distinct patterns for specimens subjected to conditions promoting ASR, DEF, or both mechanisms simultaneously. Mixtures containing reactive aggregates (FA_SR_T and FA_SR_90) showed higher expansion than those without, indicating the occurrence of ASR. However, the addition of sulfates and high-temperature curing (FA_SNR_90 and FA_SR_90) resulted in even greater expansion, suggesting a significant contribution from DEF.

The expansion was higher in the presence of a reactive aggregate and added sulphate (FA_SR_90), which might be due to the high curing temperature initiating ASR, while the subsequent reaction occurs later in moist curing conditions [21]. Without a reactive aggregate, the larger expansion of FA_SNR_90 than FA_SNR_T at 200 days was likely due to ettringite formation at a later age. Usually, when sulphate is added, alkali content is exposed to a high temperature (over 70 °C) at an early stage, DEF is more likely to occur [7]. Even at 200 days, a continued expansion is evident from the DEF requiring more time to complete the reaction [22].

In the specimens that exhibited a significant expansion, there was a steeper slope from a gradual degradation of compressive strength in FA_SR_T compared to the slope of FA_SNR_90 and FA_SR_90, which gradually increased at the beginning and rapidly reduced at a later age. The gradual degradation in FA_SR_T indicates that K_2SO_4 and reactive aggregate cause ASR expansion and subsequent damage at the initial stage due to ASR gel that produces an internal tensile strength and easily affects ASR as a reduction of the modulus [23].

In the specimens coupled with ASR and DEF (FA_SR_90), the ASR acceleration at the initial stage from the elevated temperature can immediately reduce compressive strength development and early expansion. The subsequent damage and rapid expansion at later stages might be caused by DEF, which likely results from a lowered pH by ASR occurrence.

Alternatively, the increased slope for FA_SNR_90 at the initial stage might be due to the accelerated hydration from an increased curing temperature [24]. At later stages, the slope of FA_SNR_90 starts to fall sharply when the expansion reaches approximately 0.18%, which might be due to the occurrence of DEF leading to a rapid reduction of the compressive strength.

2.3 Expansion and Strength Development Patterns

This study's expansion and strength development patterns reveal complex interactions between ASR, DEF, and fly ash over time. The non-linear relationship between expansion and compressive strength, particularly evident in mixtures subjected to both ASR and DEF conditions (FA_SR_90), supports this study's fourth hypothesis (H4). This non-linear relationship suggests the existence of a threshold expansion value beyond which strength loss accelerates rapidly.

For the FA_SR_90 mixture, this threshold appears to be around 0.2% expansion, corresponding to the 56-day measurement. After this point, the rate of strength loss increased dramatically, with compressive strength dropping from 31.51 MPa at 56 days to 13.60 MPa at 200 days. This observation is consistent with the findings of Bérubé et al. (2002), who reported accelerated strength loss in concrete affected by both ASR and DEF once a critical level of expansion was reached.

The time-dependent nature of ASR and DEF development is also evident in the results. In mixtures prone to both mechanisms (FA_SR_90), expansion occurred more rapidly in the early stages (up to 56 days) compared to DEF-only mixtures (FA_SNR_90). This suggests that ASR may have dominated the early expansion, with DEF contributing more significantly to later stages. This observation supports the fifth hypothesis (H5) and aligns with the work of Biangam et al.(2012), [25] who noted that the relative contributions of ASR and DEF to concrete deterioration can vary over time.

2.4 Implications for Concrete Durability

The findings of this study have several important implications for concrete durability in environments where both ASR and DEF are potential concerns:

1) Fly ash effectiveness: While 20% fly ash replacement effectively mitigated ASR expansion, controlling DEF under aggressive conditions may not be sufficient. This suggests higher fly ash contents or combinations with other supplementary cementitious materials may be necessary for comprehensive durability enhancement.

2) Synergistic effects: The severe deterioration observed in specimens subjected to both ASR and DEF highlights the need to consider potential synergistic effects when assessing concrete durability. Designing for resistance to a single degradation mechanism may not be sufficient in complex exposure environments.

3) Early-age thermal management: The significant impact of high-temperature curing on DEF development underscores the importance of careful thermal management in precast concrete production and mass concrete placement. Limiting maximum curing temperatures and controlling cooling rates may be critical for long-term durability.

4) Long-term monitoring: The delayed nature of DEF-induced expansion and strength loss emphasizes the need for extended monitoring periods in durability studies and in-service structures. Standard 28-day tests may not capture the full extent of potential deterioration in systems prone to DEF.

5) Mixture optimization: The complex interactions between fly ash, ASR, and DEF observed in this study suggest that optimizing concrete mixtures for durability may require a more nuanced approach. Balancing the mitigation of multiple degradation mechanisms while maintaining desired early-age properties presents a significant challenge for concrete technologists.

2.4 Limitations and Future Research Directions

While this study provides valuable insights into the interactions between fly ash, ASR, and DEF, several limitations should be acknowledged:

1) Limited fly ash content: Only one fly ash replacement level (20%) was investigated. Future studies should explore a range of fly ash contents to determine optimal levels for mitigating both ASR and DEF.

2) Single fly ash source: The study used Class F fly ash from a single source. Different fly ash compositions may yield varying results, warranting further investigation.

3) Mortar vs. concrete: The use of mortar specimens, while allowing for accelerated testing, may not fully represent the behavior of concrete under field conditions. Validation studies using concrete specimens are recommended.

4) Laboratory conditions: The controlled laboratory environment may not accurately reflect the variability of field exposure conditions. Long-term field studies would provide valuable complementary data.

5) Limited duration: While the 200-day test period captured significant deterioration, even longer-term studies may reveal additional insights into the progression of ASR and DEF.

Based on these limitations and the findings of this study, several directions for future research are proposed:

1) Investigate the effectiveness of higher fly ash contents and combinations with other supplementary cementitious materials in mitigating combined ASR-DEF deterioration.

2) Explore alternative test methods that can differentiate between ASR and DEF-induced expansion, such as microstructural analysis techniques.

3) Conduct parallel studies using concrete specimens to validate the mortar bar results and assess the impact of coarse aggregates on ASR-DEF interactions.

4) Develop and validate numerical models to predict long-term concrete performance under combined ASR-DEF conditions, incorporating the effects of fly ash and other mitigation strategies.

5) Investigate the potential for developing performance-based specifications that address multiple degradation mechanisms simultaneously, moving beyond single-parameter durability criteria.

CONCLUSIONS

This study investigated the effects of fly ash on the compressive strength and expansion of mortar specimens subjected to conditions promoting alkali-silica reaction (ASR) and/or delayed ettringite formation (DEF). The key findings can be summarized as follows:

1) The 20% fly ash replacement used in this study effectively mitigated ASR-induced expansion but showed limited efficacy in controlling DEF under aggressive conditions.

2) Specimens subjected to conditions promoting both ASR and DEF exhibited the highest expansion and most severe strength loss, supporting the hypothesis of synergistic effects between these degradation mechanisms.

3) A non-linear relationship between expansion and compressive strength was observed, with accelerated strength loss occurring beyond a threshold expansion value of approximately 0.2%.

4) The relative contributions of ASR and DEF to overall deterioration varied over time, with ASR appearing to dominate early expansion and DEF becoming more significant in later stages.

5) High-temperature curing significantly exacerbated both ASR and DEF-induced deterioration, highlighting the importance of thermal management in concrete production and placement.

These findings contribute to the broader understanding of concrete durability under complex exposure conditions and have important implications for designing durable cementitious systems. The study underscores the need for a more comprehensive approach to durability enhancement that considers multiple degradation mechanisms and their potential interactions. Future research should optimize fly ash content and explore combinations with other supplementary cementitious materials to effectively mitigate ASR and DEF. Additionally, long-term field studies and the development of advanced predictive models will be crucial for translating these laboratory findings into practical guidelines for durable concrete design and construction.

ACKNOWLEDGEMENT

REFERENCES

1. Thomas M. The effect of supplementary cementing materials on alkali-silica reaction: A review. Cem Concr Res. 2011;41(12):1224-31.

2. Rajabipour F, Giannini E, Dunant C, Ideker JH, Thomas MDA. Alkali-silica reaction: Current understanding of the reaction mechanisms and the knowledge gaps. Cem Concr Res. 2015;76:130-46.

3. Ichikawa T, Miura M. Modified model of alkali-silica reaction. Cement and Concrete Research. 2007;37(9):1291-7.

4. Gaboriaud F, Nonat A, Chaumont D, Craievich AF. Aggregation and gel formation in basic silico-calco-alkaline solutions studied: a saxs, sans, and els study. Journal of Physical Chemistry B. 1999;103:5775-81.

5. Lindgård J, Andiç-Çakır Ö, Fernandes I, Rønning TF, Thomas MDA. Alkali-silica reactions (ASR): Literature review on parameters influencing laboratory performance testing. Cement and Concrete Research. 2012;42(2):223-43.

6. Scrivener KL, Taylor HFW. Delayed ettringite formation: a microstructural and microanalytical study. Advances in Cement Research. 1993;5(20):139-46.

7. Taylor HFW, Famy C, Scrivener KL. Delayed ettringite formation. Cement and Concrete Research. 2001;31(5):683-93.

8. Brunetaud X, Linder R, Divet L, Duragrin D, Damidot D. Effect of curing conditions and concrete mix design on the expansion generated by delayed ettringite formation. Mater Struct. 2007;40(6):567-78.

9. Ramlochan T, Zacarias P, Thomas MDA, Hooton RD. The effect of pozzolans and slag on the expansion of mortars cured at elevated temperature: Part I: Expansive behaviour. Cem Concr Res. 2003;33(6):807-14.

10. Bérubé MA, Duchesne J, Dorion JF, Rivest M. Laboratory assessment of alkali contribution by aggregates to concrete and application to concrete structures affected by alkali-silica reactivity. Cem Concr Res. 2002;32(8):1215-27.

11. Thanadet S, Shingo A, Joshi Nirmal R. Study on the combined alkali silica reaction and delayed ettringite formation. Geomate Journal. 2020;19 (75):84-91.

12. Shehata MH, Thomas MDA. The effect of fly ash composition on the expansion of concrete due to alkali-silica reaction. Cem Concr Res. 2000;30 (7):1063-72.

13. Malvar L, Lenke L. Efficiency of fly ash in mitigating alkali-silica reaction based on chemical composition. ACI Mater J. 2006;103.

14. Owsiak Z. The effect of delayed ettringite formation and alkali-silica reaction on concrete microstructure. Ceramics - Silikaty. 2010;54.

15. Mehta PK, Monteiro PJM. Concrete: Microstructure, Properties, and Materials. 4th Edition ed. New York: McGraw-Hill Education; 2014.

16. Escadeillas G, Aubert JE, Segerer M, Prince W. Some factors affecting delayed ettringite formation in heat-cured mortars. Cem Concr Res. 2007;37:1445-52.

17. Zhang Z, Olek J, Diamond S. Studies on delayed ettringite formation in early-age, heat-cured mortars I. Expansion measurements, changes in dynamic modulus of elasticity, and weight gains. Cem Concr Res. 2002a;32:1729-36.

18. Zhang Z, Olek J, Diamond S. Studies on delayed ettringite formation in heat-cured mortars II. Characteristics of cement that may be susceptible to DEF. Cem Concr Res. 2002b;32:1737-42.

19. Famy C. Expansion of Heat-Cured Mortar [dissertation]. London: University of London; 1999.

20. Famy C, Scrivener KL, Atkinson A, Brough AR. Influence of the storage conditions on the dimensional changes of heat-cured mortars. Cem Concr Res. 2001;31(5):795-803.

21. Diamond S, Ong S. Combined effects of ASR and secondary ettringite deposition in steam cured mortars. In: Gartner EM, Uchikawa H, editors. Cement technology. Westerville (OH): The American Ceramic Society; 1994. p. 79.

22. Shayan A, Aimin X. Effect of cement composition and temperature of curing on AAR and DEF expansion in steam-cured concrete. In: Proceedings of the 12th International Conference on Alkali-Aggregate Reaction in Concrete; 2014. p. 773-88.

23. Mohammadi A, Ghiasvand E, Nili M. Relation between mechanical properties of concrete and alkali-silica reaction (ASR); a review. Constr Build Mater. 2020;258:1-16.

24. Elkhadiri I, Palacios M, Puertas F. Effect of curing temperature on cement hydration. Ceramics Silikaty. 2009;53(2):65-75.

25. Baingam L, Sangsoy W, Choktaweekarn P, Tangtermsirikul S. Diagnosis of a combined alkali silica reaction and delayed ettringite formation. TIJSAT. 2012;17(4):23-8.

Sustainable composite foam development: Crosslinked tapioca starch with corn husk sheet reinforcement and chitosan biocoating

Manisara Phiriyawirut*, **Kanitta Liangkee, Prueksa Pruangsillaparat and Suchada Tunnara**

Department of Tool and Materials Engineering, Faculty of Engineering, King Mongkut's University of Technology Thonburi, Thungkru, Bangkok 10140, THAILAND
*Corresponding author: manisara.pee@kmutt.ac.th

ABSTRACT

Laminar composite foams were developed to create environmentally sustainable materials. Crosslinked tapioca starch was utilized as the foam matrix and reinforcement was provided by corn husk sheets, with a chitosan biocoating subsequently applied to modify the surface. These foams were produced through hot-pressing, with the number of corn husk sheet layers varied (1, 2, and 3) alongside chitosan coating concentrations (1% and 3% by weight). The resultant materials were subjected to comprehensive characterization, where morphology, density, crystallinity, flexural and impact strength, thermal stability, and water absorption properties were evaluated. Refined foam cell structure and reduced structural defects were observed upon incorporating corn husk sheets. Increases in density and mechanical strength, as determined through flexural and impact testing, were documented with higher fiber content. In contrast, thermal stability decreased, while water absorption was reduced. The chitosan biocoating further densified the foam cell structure, increasing density and mechanical strength with increasing concentration, though crystallinity showed no significant change. Notably, the chitosan coating improved water resistance. The composite foam with two corn husk layers and a 3% chitosan coating exhibited optimal performance, demonstrating a 57.32% reduction in water uptake after 20 minutes, a 251.61% increase in flexural strength, and a 195.23% rise in impact strength compared to the unmodified foam. These sustainable composite foams show significant potential for sustainable food packaging, highlighting the synergistic property enhancements achieved through this laminar composite architecture.

Keywords: Starch foam, Corn husk, Chitosan, Laminar composite, Water resistance

INTRODUCTION

Thailand has been increasingly confronted by a significant environmental challenge stemming from the rising volume of annual waste. This increase is largely attributed to greater consumer spending and rapid technological advancements, leading to shorter product lifespans. Notably, plastic materials, especially foam plastics, are widely used in packaging and containers due to their lightweight nature and ease of manufacture. However, the growing accumulation of plastic waste has exacerbated environmental problems [1]. In 2021, approximately 2.76 million tons of plastic waste were generated in Thailand, representing about 11% of the total waste. Most of this plastic was single-use. These synthetic, non-biodegradable plastics pose a major disposal issue. Incineration, a common waste management method, has resulted in environmental pollution. Specifically, the combustion of foam materials releases styrene gas, which is absorbed through the skin and lungs. Long-term styrene exposure has been linked to adverse effects on the central nervous system, including headaches, fatigue, and potential depression [2].

To address these environmental concerns, bio-based polymers have been investigated as sustainable substitutes for materials derived from fossil fuels, with their potential for reduced harmful emissions being a key advantage. Tapioca starch, a readily available bio-based polymer in Thailand, has been considered for food packaging applications under low moisture conditions. However, its inherent limitations, particularly brittleness, low mechanical strength, and poor water resistance, have restricted its widespread use compared to synthetic polystyrene foam. Starch, a renewable and biodegradable biopolymer obtained from abundant agricultural sources such as tapioca, corn, and rice, is a promising alternative to petroleum-based packaging materials [3-4]. Its easy availability, low cost, and biodegradability have aligned with the increasing demand for environmentally conscious materials.

Starch-based foams are recognized for their limited flexibility and high susceptibility to moisture

[5]. To mitigate these inherent drawbacks, starch modification through crosslinking has been explored. Glyoxal, a documented crosslinking agent, effectively alters starch, improving water resistance [6-7]. Nevertheless, crosslinked starch foams still exhibit issues with brittleness and high water absorption. To address these remaining shortcomings, strategies involving blending with hydrophobic polymers, such as octanoyl starch [8] and PBS [9], or reinforcement with natural fibers like chitin [8], have been investigated. Natural fibers, including jute, corn husk, kraft pulp, sugarcane bagasse, and flax, have also been considered as reinforcement materials [10]. Studies on the mechanical properties of these natural fibers indicate that fiber length and orientation significantly influence their strength [11]. Consequently, research has increasingly focused on composite material development. Laminar composites, characterized by low density, lightweight, and versatile properties, have been explored as a potential solution. Material properties can be tailored in these structures by strategically aligning fibers or reinforcements along applied stress directions, optimizing performance for specific uses [12-13].

Often viewed as readily available agricultural residues, corn husks, the natural protective outer layers of corn cobs, have gained increasing attention as a sustainable and economical resource, traditionally used for food wrapping during cooking. A distinct color change is typically observed, from light green when fresh to cream or light brown upon drying. Fibers easily obtained from corn husks and stalks have been explored for textiles and composite reinforcement, and they are already being used in decorations and some food packaging due to their low cost [14]. The significant elongation exhibited by corn husks under tension, comparable to coconut and palm fibers, makes them interesting for reinforcing polymer matrices. It is generally accepted that a natural fiber's elongation at break is mainly determined by its cellulose content and the alignment of cellulose microfibrils along the fiber axis. Consequently, corn husk fibers have been investigated as reinforcement in numerous polymer composite studies [15-16]. Based on these promising characteristics, corn husk sheets are particularly suitable for laminar reinforcement within crosslinked starch foam structures.

To specifically address the inherent susceptibility to water often associated with starch foam packaging, crosslinked starch laminate composite foams, reinforced through the strategic incorporation of corn husks in a layered structure, were developed as a central focus of this research. Corn husks were utilized explicitly as a reinforcing phase within these composite structures to improve the overall mechanical integrity and reduce water uptake. However, it is well-established that natural cellulose fibers, including those abundantly present in corn husks, are known to

exhibit a degree of interaction with water molecules due to the presence of numerous hydroxyl groups (-OH) within their fundamental chemical structure, which readily attract and bind with water molecules through hydrogen bonding [17]. This inherent characteristic has been observed to result in limitations such as poor overall water resistance of the resulting composite.

Chitosan, a linear polysaccharide copolymer derived from chitin, has garnered significant interest for its ability to impart enhanced water resistance and antifungal properties, as widely explored in scientific literature [18-22]. Previous studies have demonstrated that chitosan coatings can slightly increase density and reduce water and moisture absorption in starch-based materials [23]. Its capacity to form films that significantly enhance barrier properties, particularly water resistance due to its polar nature, makes it a promising candidate. Moreover, chitosan is recognized for its potential to improve mechanical strength and rigidity when applied as a coating, a characteristic expected to densify the surface of our starch/corn husk foams and provide additional structural integrity. Its inherent antimicrobial properties also offer a potential benefit for food packaging applications.

This study introduces a novel approach to address limitations in existing starch-based biocomposites by developing a unique laminar composite architecture. This innovative design integrates a crosslinked tapioca starch foam matrix with distinct corn husk sheet reinforcing layers, a structural configuration that is less explored in sustainable materials. We aim for a synergistic enhancement of properties through this specific layered design. A chitosan biocoating is then applied to the composite surface. This coating's primary goal is to enhance water resistance, while its known antimicrobial properties offer a potential secondary benefit for food packaging applications. Our research focuses explicitly on simultaneously improving critical properties like water resistance and mechanical strength, which remain significant hurdles for many current starch-based materials, especially for sustainable food packaging. We investigate how varying the number of corn husk sheet layers and the chitosan coating concentration influences these crosslinked tapioca starch laminate composite foams' morphology, density, thermal properties, flexural/impact strength, and water absorption. This detailed investigation aims to clearly articulate the scientific gap our work addresses and its unique contribution to the field of sustainable biocomposites.

MATERIALS AND METHODS

Materials

Tapioca starch, the foundational matrix material, was obtained from commercial suppliers in Thailand. Processing aids, including guar gum and magnesium

stearate, were sourced from Chemipan Corporation Co., Ltd. (Thailand). To modify the tapioca starch matrix, glyoxal (40% solution, Merck) was employed as the crosslinking agent. Acetic acid (analytical reagent grade, RCI Labscan Co. Ltd, Thailand) was utilized in pH adjustments and chitosan processing. Corn husk sheets, representing the sustainable reinforcement component, were procured from a local farm within Thailand. The corn husk sheets used were carefully selected to maintain consistent dimensions, specifically 20 mm in width, 150 mm in length, and approximately 0.2 mm in thickness. The control over thickness was primarily achieved through a meticulous manual selection process of individual corn husk sheets, ensuring uniformity for the fabrication of the composite foams. Chitosan was acquired from Marine Bio Resources Co. Ltd. (Thailand) to apply biocoating, which is characterized by a degree of deacetylation (DD) of 72%.

Preparation of chitosan biocoated corn husk sheets

A chitosan biocoating procedure was implemented to enhance interfacial compatibility and reduce the moisture sensitivity of the corn husk sheet reinforcement. Chitosan solutions, at 1% and 3% (w/v) concentrations, were formulated by dissolving chitosan powder in a 1% (v/v) aqueous acetic acid solution. The resulting solutions were magnetically stirred at room temperature (25°C) until complete dissolution and homogeneity were achieved.

Next, pre-cut corn husk layers were immersed in the prepared chitosan solutions at 25°C for uniform coating. After immersion, these biocoated layers were oven-dried at 50°C for 10 minutes to remove residual solvent and fix the chitosan. The resulting chitosan-modified reinforcement was then stored in a desiccator until incorporated into the crosslinked tapioca starch foam matrix.

Crosslinked tapioca starch preparation

An initial pre-drying step was performed on 80 g of tapioca starch at 110°C for 24 hours to remove residual moisture and prepare the crosslinked tapioca starch. The dried starch was then dispersed in 120 mL of deionized water. Glyoxal, employed as the crosslinking agent, was added at a concentration of 0.0375 g per 100 g of starch [7-8]. The mixture was then mechanically stirred at 25°C for 20 minutes to ensure uniform crosslinking was achieved. Subsequently, the resulting starch-glyoxal mixture was vacuum-filtered using an aspirator pump. Unreacted glyoxal was removed by thoroughly rinsing the filtered mixture three times with deionized water. The filtered crosslinked starch was then dried at 50°C for 24 hours. Finally, the dried material was ground into a fine powder using a mortar and pestle and then sieved through a 60-mesh sieve to obtain a consistent particle size.

Composite foam formulation

A uniform dry blend was formulated using 100 g of crosslinked tapioca starch powder. To enhance binding and lubrication, 1 wt% guar gum and 2 wt% magnesium stearate were incorporated, respectively [9]. These components were thoroughly mixed using a kitchen-aid mixer. Subsequently, 120 g of distilled water was gradually introduced into the dry mixture. The resulting mixture was subjected to an additional 20 minutes of mixing to ensure complete dispersion and hydration.

Fabrication of crosslinked starch/corn husk laminate composite foams

Composite foam fabrication utilized a compression molding technique. Molds, 15 mm wide by 120 mm long, adhered to ASTM D5943-5996 flexural and impact testing standards. Starch mixture and reinforcing corn husk layers (either uncoated or chitosan-coated) were integrated following specific patterns (Figure 1). For the single-layer design (Figure 1a), the process began with a starch mixture base, followed by a corn husk layer centered in the mold, then topped with more starch mixture. In the two-layer configuration (Figure 1b), two husk layers were placed at the mold's bottom and top, with starch mixture introduced between them. For the three-layer setup (Figure 1c), three husk layers alternated with the starch mixture, with a husk layer forming the final surface. The loaded molds were then subjected to 160°C and 50 bar pressure for 4 minutes to facilitate crosslinking and lamination. The resulting crosslinked starch/husk laminate composite foams were subsequently cooled to ambient temperature.
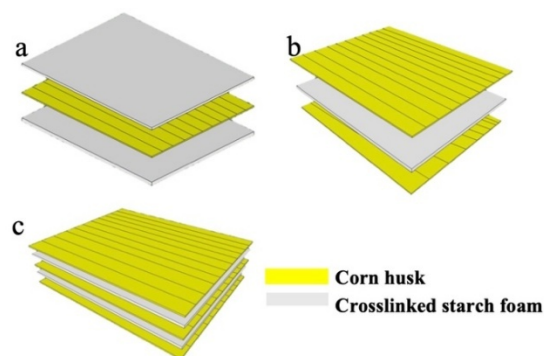
Figure 1 The configuration of crosslinked starch/corn husk laminate composite foams with varying numbers of corn husk layers: (a) single-layer, (b) two-layer, and (c) three-layer.

Characterization

Morphology: The microstructure of corn husk sheets, as well as crosslinked tapioca starch/corn husk laminate composite foams, both with and without chitosan biocoating, was investigated using scanning electron microscopy (SEM, JEOL JSM-6610 LV). Fracture surfaces resulting from flexural testing were sputter-

coated with gold to improve electrical conductivity. SEM images were obtained at an accelerating voltage of 10 kV, allowing for visualization of the foam morphology and interfacial interactions.

Density: The density of the composite foams was determined at room temperature using a density determination kit, with chloroform employed as the displacement fluid.

Crystal structure: The crystalline structure of the composite foams was analyzed using X-ray diffraction (XRD). Measurements were performed at room temperature on both chitosan-coated and uncoated samples.

Thermal stability: The thermal degradation behavior of the composite foams was evaluated using thermogravimetric analysis (TGA, NETZSCH TG 209 F3 Tarsus). Before TGA, samples were dried at 80°C for 72 hours to remove residual moisture. TGA was conducted under a nitrogen atmosphere at a heating rate of 10°C/min, from 30°C to 500°C. Weight loss data was subsequently used to assess the thermal stability of the materials.

Mechanical properties: The flexural strength of the composite foams was determined through a three-point bending test conducted on a LLOYD Instruments LR50K universal testing machine, following ASTM D790-03. The test was performed with a maximum load of 5 kN and a 2 mm/min crosshead speed. The impact strength of notched composite foams was evaluated using a cantilever beam (Izod-type) impact test, per ASTM D256. Notches, 4.8 mm in depth and 0.25 mm in radius, were introduced into the samples using a milling machine, as specified by ASTM D256. Three impact tests were performed per sample, and the average impact strength was subsequently reported.

Figure 2 Experimental setup for water absorption crosslinked starch/corn husk laminate composite foams.

Water absorption and weight loss: To evaluate the water absorption behavior of the fabricated sustainable composite foams, square specimens of crosslinked tapioca starch/corn husk laminate composites (15.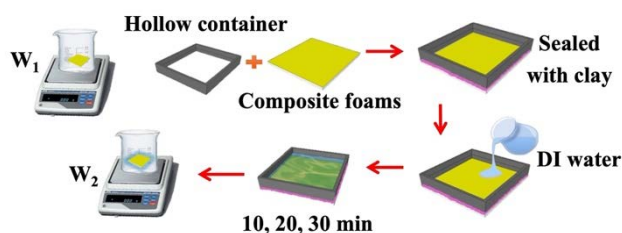0 mm x 15.0 mm), both with and without chitosan biocoating, were prepared. Water absorption capacity was determined using a custom-designed apparatus, as shown in Figure 2. A plastic hollow rectangular container with dimensions of 15.0 × 15.0 mm, sized to fit the test samples precisely, was placed on each foam specimen and sealed with modeling clay to prevent leakage. Deionized water was then carefully added to the container. Water uptake was measured at predetermined time intervals of 10, 20, and 30 minutes. After each interval, any surface water was gently removed using absorbent paper, and the specimens were immediately reweighed. All tests were performed under controlled conditions at 25 °C. The percentage of water absorption was calculated using Equation 1:

Water Absorption (%) = $[(W_2 - W_1) / W_1]$ x 100 (1)

where W_1 represents the initial weight of the specimen, and W_2 represents the weight of the specimen after water absorption.

In order to evaluate the potential for degradation or leaching of constituent components from the composite foams, weight loss measurements were conducted. Specimens, sized 15.0 mm x 15.0 mm, were immersed in deionized water for 24 hours. Following this immersion, specimens were carefully removed and placed within a forced-air convection oven, maintained at a temperature of 60°C. Drying was continued for 24 hours, or until a consistent weight was attained, indicating the removal of all absorbed moisture. The weight loss percentage was then determined by applying Equation 2.

Weight Loss (%) = $[(W_1 - W_3) / W_1]$ x 100   (2)

where W_1 represents the initial weight of the specimen, and W_3 represents the weight of the specimen after immersion and drying.

RESULTS AND DISCUSSION

Crosslinked starch/corn husk laminate composite foams
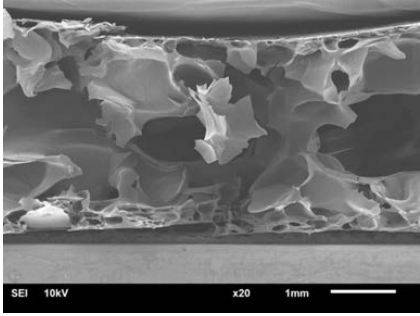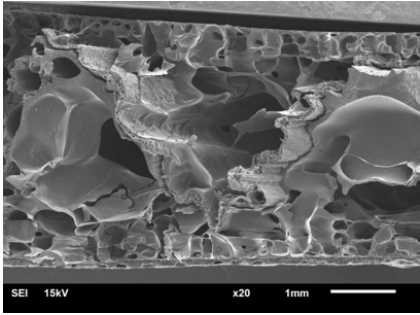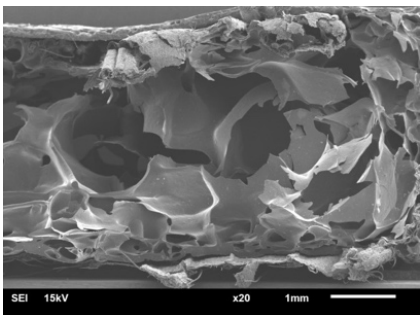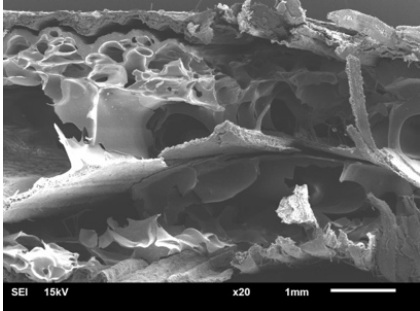
Crosslinked tapioca starch composite foams were reinforced with corn husk sheets, selected for their established mechanical strength and inherent water resistance. To evaluate the influence of reinforcement layers, single-layer, two-layer, and three-layer configurations of corn husk were incorporated into the starch foam matrix.

The morphology of the resulting crosslinked tapioca starch/corn husk laminate composite foams was examined through scanning electron microscopy (SEM). Representative SEM images are presented in Table 1. For pure crosslinked tapioca starch foam, a dense outer layer with small foam cells was observed, while the inner core exhibited larger cells and evidence of fracture, indicative of inherent brittleness. However, upon the introduction of a single corn husk sheet as a central reinforcement layer, a more uniform foam cell structure was achieved. This structural modification was accompanied by an increase in overall density and a reduction in average cell size. Furthermore, the void size within the central core was also observed to decrease.

A notable increase in foam cell density and a concurrent decrease in cell size were observed upon incorporating two corn husk sheets, strategically positioned on the upper and lower surfaces of the tapioca starch foam. Conversely, including three corn husk sheet layers resulted in the formation of larger voids within the foam structure. It is hypothesized that the increased confinement of the starch matrix between three corn husk sheet layers restricted its expansion during the foaming process, leading to the development of larger, fewer foam cells. Consequently, the three-layer composite exhibited a lower overall foam density when compared to the composites reinforced with one and two layers. These findings highlight the significant influence of corn husk sheet distribution on the resulting foam morphology and density.

Table 1 Fracture surface analysis (visual inspection and SEM micrograph) and density of crosslinked starch/corn husk laminate composite foams with varying numbers of corn husk layers.

Numbers of corn husk layers	Fracture surface		Density (g/cm^3)
	Visual inspection	SEM micrograph (20X)	
0	-		0.29 ± 0.01
1			0.41 ± 0.13
2			0.41 ± 0.15
3			0.60 ± 0.32

The density of the crosslinked tapioca starch/corn husk laminate composite foams, incorporating one, two, and three layers of corn husk sheets, was measured and is presented in Table 1. A consistent increase in density was observed with each additional corn husk sheet layer. This increase can be attributed

to the inherent density of the corn husk sheets, determined to be 0.35 ± 0.45 g/cm³. As the number of corn husk sheet layers integrated into the composite structure was increased, a corresponding rise in the overall density of the resulting foam material was noted. This finding is consistent with previous research [8, 24]. This observation highlights the effective contribution of corn husk sheets as a reinforcing component in enhancing the bulk density of the tapioca starch-based composite foam.

X-ray diffraction (XRD) patterns, illustrating the crystalline structures of crosslinked tapioca starch foam and a composite foam reinforced with two corn husk sheet layers, are presented in Figure 3. A characteristic peak at 17.1°, indicative of the semi-crystalline nature of the starch, was observed in the XRD pattern of the crosslinked tapioca starch foam [25]. Upon incorporating two corn husk sheet layers, a new peak was detected at 22.6°, attributed to crystalline cellulose within the corn husk [26]. This cellulose-specific peak, absent in the pure starch foam pattern, confirms the successful integration of corn husk sheets. While the overall pattern of the laminate composite foam appeared sharper than that of the pure starch foam, this primarily indicates the crystallinity contributed by the corn husk component itself, rather than a significant increase in the crystallinity of the starch matrix.

Table 2 presents the flexural strength and elongation at break of the crosslinked tapioca starch/ corn husk laminate composite foams. A notable increase in flexural strength was observed as the corn husk sheet content was increased from one to two layers. This improvement is attributed to the laminar reinforcement mechanism, which effectively enhanced the material's capacity to bear load during three-point bending tests. It is theorized that this type of reinforcement facilitates a more efficient

distribution of both compressive and tensile stresses experienced by the material, a phenomenon supported by previous studies' findings [27]. However, a subsequent increase in the corn husk sheet content to three layers decreased flexural strength. This reduction is likely due to a relative decrease in the proportion of the continuous starch matrix within the composite structure, leading to a reduction in the number of cohesive foam cells and a concurrent increase in overall porosity. Consequently, the efficiency of interfacial stress transfer between the distinct phases of the composite was compromised, ultimately resulting in a lower measured flexural strength. Moreover, while corn husk provides reinforcement, the interface between the corn husk and the starch matrix might not be perfectly bonded without adhesion promoters. At three layers, the increased number of interfaces could lead to more potential sites for interfacial debonding or delamination under flexural stress, thereby lowering the strength.
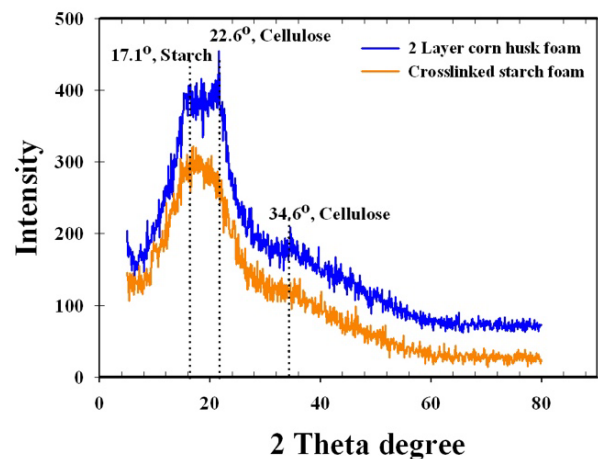
Figure 3 XRD patterns of crosslinked starch foam and crosslinked starch laminate composite foams with 2 layers of corn husk sheet.

Table 2 Flexural properties and impact strength of crosslinked starch/corn husk laminate composite foams with varying numbers of corn husk layers.

Numbers of corn husk layers	Flexural properties			Impact strength (J/m²)
	Strength (MPa)	Strain (%)	Modulus (MPa)	
0	3.1 ± 0.4	4.1 ± 0.0	278 ± 0.1	56.6 ± 0.5
1	7.5 ± 0.2	4.8 ± 0.1	566 ± 0.0	96.9 ± 0.2
2	10.3 ± 0.1	4.6 ± 0.8	796 ± 0.2	139.0 ± 0.3
3	8.2 ± 0.3	7.0 ± 0.2	278 ± 0.1	117.7 ± 0.4

Interestingly, the observed increase in flexural strain for the three-layer composite, notably higher than that of the one- and two-layer samples, can be attributed to several toughening mechanisms inherent in multi-layered laminar structures. The increased number of reinforcing corn husk layers likely facilitates improved stress distribution across the composite,

allowing individual layers to deform more effectively before catastrophic failure [28]. This multi-layered configuration can also promote crack deflection at the interfaces, forcing propagating cracks to follow a more tortuous path and thereby absorbing more energy [29]. Furthermore, the overall enhanced deformability of the structure, despite the presence

of rigid reinforcing layers, may stem from the intricate interplay between the flexible starch foam matrix and the multiple corn husk layers, enabling greater strain accommodation before fracture [30]. These combined effects contribute to the superior ductility observed in the three-layer composite.

Impact resistance of the crosslinked tapioca starch laminate composite foams, reinforced with varying corn husk sheet layers (1, 2, and 3 layers), was evaluated, and the results are presented in Table 2. A noticeable increase in impact resistance was recorded when the corn husk sheet content was raised from 1 to 2 layers. This improvement is believed to be a direct result of the inherent strength of the corn husk sheets, which effectively reinforced the composite foam against impact. Furthermore, the increased density and reduced foam cell size observed in the 2-layer samples facilitated efficient stress transfer within the composite, contributing to the enhanced impact performance. However, a subsequent decrease in impact resistance was seen upon further increasing the corn husk sheet content to 3 layers. This reduction is associated with a corresponding decrease in foam density and an increase in foam

cell size, leading to larger voids. These voids are hypothesized to have interfered with effective stress transfer, thereby diminishing the overall impact resistance of the composite foam.

The thermal stability of corn husk sheets, crosslinked tapioca starch foam, and the resulting crosslinked tapioca starch/corn husk laminate composite foams was evaluated using thermogravimetric analysis (TGA). Distinct thermal degradation profiles for each material were observed, as illustrated in Figure 4 and summarized in Table 3.

Thermal decomposition of corn husk sheets was observed to occur in two stages. An initial 5.67% weight loss was noted between 36°C and 162°C, attributed to moisture evaporation. A subsequent substantial weight loss of 38.87% began at 188°C, corresponding to cellulose and hemicellulose degradation. Similarly, crosslinked tapioca starch foam exhibited a two-stage degradation profile. The first stage, between 36°C and 248°C, involved 7.16% weight loss due to moisture evaporation. At 269°C, significant degradation (79.21% weight loss) was observed, associated with the breakdown of α-1,4 glycosidic linkages within the starch polymer.
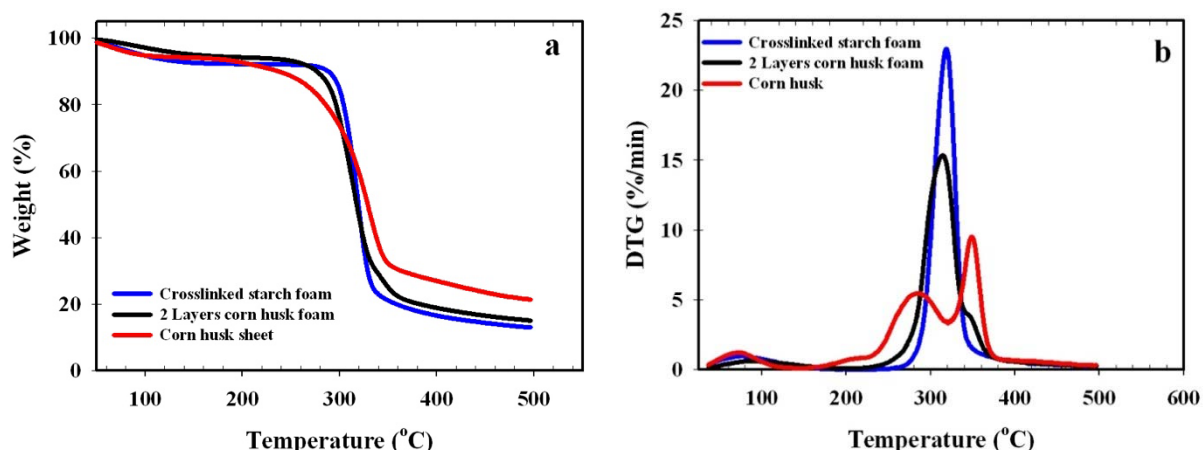
Figure 4 Thermal degradation behavior of corn husk sheet, crosslinked starch foam and crosslinked starch/corn husk laminate composite foams (a) TGA thermogram and (b) DTG thermogram.

Table 3 Thermal degradation of corn husk sheet, crosslinked starch foam and crosslinked starch/corn husk laminate composite foams.

Sample	1st Degradation		2nd Degradation	
	T (°C)	W (%)	T (°C)	W (%)
Corn husk sheet	36-162	5.67	188	72.76
Crosslinked starch foams	36-248	7.16	269	79.21
Crosslinked starch laminate composite foams with 2 layers of corn husk sheet	36-117	5.70	247	79.14

It was observed that the crosslinked tapioca starch/corn husk laminate composite foams demonstrated a reduced thermal stability when compared to the crosslinked tapioca starch foam. This reduction can be attributed to corn husk sheets containing β-1,4 glycosidic linkages. These linkages

are known to degrade at a lower temperature (188°C) than the α-1,4 linkages found in tapioca starch (degrading between 260-320°C). Consequently, the composite foams showed an earlier onset of thermal degradation [31], indicating that the corn husk

component's thermal stability dictates the overall composite's initial degradation temperature.

The water absorption behavior of crosslinked tapioca starch foam and its corn husk sheet reinforced composites was analyzed over a 10 to 30 minutes period (Figure 5). An increase in water absorption with time was observed for both materials. However, water uptake was significantly reduced upon incorporating corn husk sheets.

The reduction in water absorption is primarily attributed to the barrier effect of the layered corn husk sheets within the composite structure. While cellulose, the main component of corn husk [14], exhibits an inherent lower affinity for water than the highly hydrophilic starch matrix, its role extends beyond mere hydrophobicity. The dense, layered arrangement of the corn husk sheets effectively impedes the diffusion of water molecules into the underlying starch foam matrix, thereby limiting direct and prolonged contact between water and the more absorbent starch component. This physical impediment significantly contributes to the observed decrease in overall water uptake.

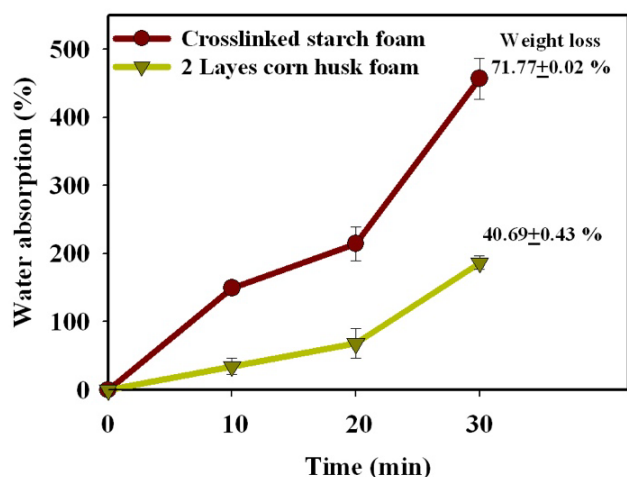**Figure 5** Water absorption and weight loss of crosslinked starch foam and crosslinked starch laminate composite foams with 2 layers of corn husk sheet.

Further evidence supporting the enhanced water resistance was obtained through weight loss measurements. Following a 24-hour water immersion and subsequent 24-hour drying at 60°C, the neat crosslinked tapioca starch foam exhibited a substantial weight loss of 71.77 ± 0.02%, indicating significant water-induced degradation. In contrast, the composite reinforced with two layers of corn husk sheet demonstrated a significantly lower weight loss of 40.69 ± 0.43%. This represents a 43.3% reduction in weight loss compared to the neat crosslinked tapioca starch foam. This decrease in weight loss is attributed to the protective effect of the corn husk sheets, which effectively encapsulate the starch foam, thereby

minimizing direct water contact and reducing the leaching of starch components into the aqueous medium.

The placement of corn husk sheet layers significantly influences the composite's overall performance in practical applications, particularly concerning mechanical integrity, barrier properties, and material efficiency. A well-distributed, multi-layered structure enhances flexural and impact strength, which is crucial for durable packaging during handling and transport, by effectively distributing stress and resisting crack propagation. Furthermore, the strategic layering of corn husk within the hydrophilic starch foam creates tortuous pathways for water molecules, significantly improving water resistance- a vital property for preserving food freshness. This allows for tailoring packaging solutions to specific performance needs, optimizing material usage, and contributing to the sustainability and cost-effectiveness of potential mass production.

Chitosan-coated crosslinked starch/corn husk laminate composite foams

The crosslinked tapioca starch laminate composite foams reinforced with corn husk sheets exhibited enhanced mechanical properties and improved, albeit still limited, water resistance. Furthermore, the susceptibility of corn husk sheets to fungal growth under high humidity conditions was identified as a challenge. To address these limitations, a chitosan solution was applied as a biocoating to the corn husk sheets further to enhance the water resistance of the composite foams. Chitosan coatings with concentrations of 1% and 3% (w/v) were investigated. The inherent hydrophilicity of both starch and corn husk contributed to the observed water absorption and fungal susceptibility. Chitosan, recognized for its antimicrobial and hydrophobic characteristics, was employed to establish a barrier against water uptake and fungal proliferation [22].
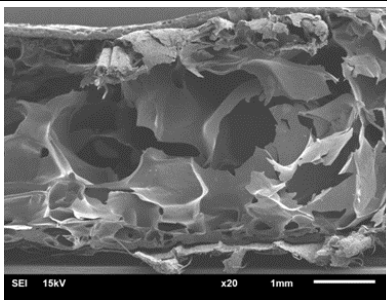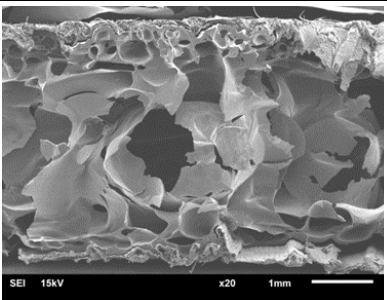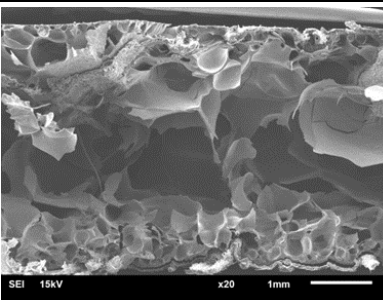
The cross-sectional morphology of composite foams, reinforced with two layers of corn husk sheets and subjected to chitosan biocoatings (0-3 wt%), was examined via scanning electron microscopy (SEM), with representative micrographs presented in Table 4. SEM analysis revealed a significant influence of the chitosan biocoating on the resultant foam morphology. Specifically, increased foam cell density was observed with increasing chitosan concentrations. This densification is attributed to forming a chitosan film that effectively occluded pores within the corn husk sheets. Consequently, water vapor diffusion during the foam formation process was hindered, leading to restricted foam cell expansion and a denser overall microstructure. The chitosan biocoating, therefore, plays a key role in modifying the cellular architecture of these sustainable composite foams, resulting in enhanced structural integrity and potentially improved

barrier properties against moisture and other environmental factors.

A direct correlation was observed between chitosan coating concentration and the density of crosslinked tapioca starch laminate composite foams reinforced with two layers of corn husk sheets. As detailed in Table 4, foam density increased proportionally with higher chitosan concentrations. This increase is attributed to the deposition of chitosan, a relatively dense polymer, onto corn husk fibers and within the foam's internal structure. The inherent high density of corn husk sheets (1.16 ± 0.40 g/cm³) also contributed to the composite's overall density. Chitosan application effectively filled voids and interstitial spaces within the foam, yielding a more compact material. This density enhancement is considered a key factor in the improved mechanical properties of the composite foams, as load-bearing capacity and structural integrity are directly influenced.

Table 4 Fracture surface analysis (SEM) and density of two-layered corn husk/crosslinked starch composite foams with varying chitosan concentrations.

	Chitosan concentration (%)		
	0	**1**	**3**
SEM (20X)			
Density (g/cm³)	0.41 ± 0.15	0.43 ± 0.29	0.50 ± 0.20

Figure 6 XRD patterns of crosslinked starch laminate composite foams with 2 layers of corn husk sheet with and without 3% chitosan coating.

Figure 6 displays the X-ray diffraction (XRD) patterns obtained for the crosslinked tapioca starch/corn husk laminate composite foams, with a direct comparison made between the uncoated sample and the sample coated with 3 wt% chitosan. Typical chitosan diffraction peaks, usually found around $9.35°$, $19.42°$, and $21.14°$ [32], were not visible in the pattern of the chitosan-coated composite foam. This absence is likely because the chitosan concentration used was too low for the XRD technique to detect. No significant change in the crystallinity of the composite foam was observed with the chitosan coating, suggesting a minimal impact on the material's structural order. This indicates that while chitosan may interact with the corn husk/tapioca starch matrix, it does not substantially alter the overall crystallinity under these conditions.

The thermal resistance properties of crosslinked tapioca starch laminate composite foams, reinforced with corn husk sheets with and without 3% chitosan coating, were compared using thermogravimetric analysis (TGA). As depicted in Figure 7 and summarized in Table 5, the results revealed that the composite foams containing 2% corn husk sheets, both uncoated and coated with 3% chitosan, exhibited a two-stage thermal degradation process.

The initial stage of thermal degradation, associated with the evaporation of absorbed moisture and volatile components, was observed in the temperature range of 36-117°C for the uncoated composite, resulting in a 5.7% weight loss. This initial stage occurred between 36-190°C for the chitosan-coated composite, with a corresponding weight loss of 6.81%. The second major degradation stage, attributed to the decomposition of α 1-4 glycosidic linkages and chitosan, commenced at 247°C for the uncoated sample and a slightly lower temperature of 238°C for the chitosan-coated sample. This second stage resulted in substantial weight

losses of 79.14% and 79.37% for the uncoated and coated samples, respectively.

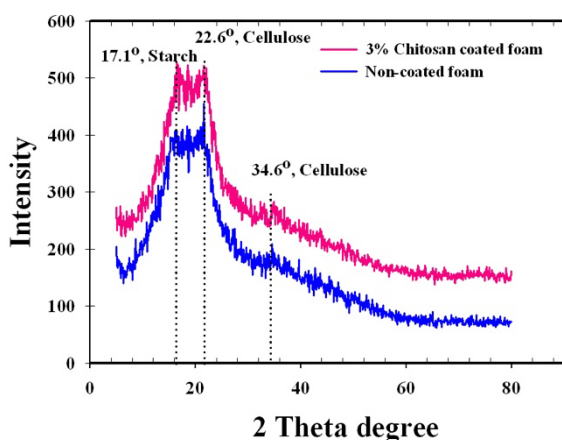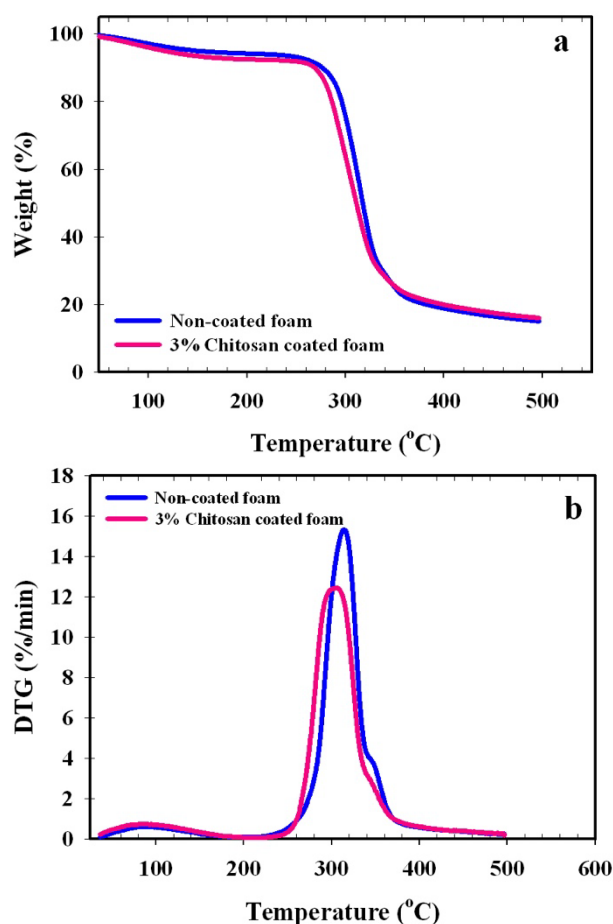**Figure 7** Thermal degradation behavior crosslinked starch laminate composite foams with 2 layers of corn husk sheet with and without 3% chitosan coating. (a) TGA thermogram and (b) DTG thermogram.

Table 5 Thermal degradation of two-layered corn husk/crosslinked starch composite foams with varying chitosan concentrations.

Chitosan conc. (%)	1st Degradation		2nd Degradation	
	T (°C)	W (%)	T (°C)	W (%)
0	36-117	5.7	247	79.14
3	36-190	6.81	238	79.37

It was observed that the chitosan-coated corn husk sheet reinforced crosslinked tapioca starch composite foam exhibited slightly faster thermal degradation compared to the uncoated counterpart. This accelerated degradation is believed to be due to the earlier decomposition of chitosan, which occurs around 200°C, a temperature lower than that of corn husk sheets and crosslinked tapioca starch. The earlier decomposition of chitosan likely initiates the degradation process at a lower temperature, leading to a slightly faster overall degradation rate for the coated composite.

The flexural and impact properties of crosslinked tapioca starch composite foams, reinforced with two corn husk sheet layers and a chitosan biocoating, were evaluated, and the results are detailed in Table 6. A slight enhancement in both flexural strength and elongation was observed with increasing chitosan concentration. This improvement is attributed to the chitosan coating, which reduced foam cell size and increased density, leading to higher structural rigidity. Furthermore, the crosslinked tapioca starch composite foams upon chitosan coating noted a marginal increase in impact resistance. This observation is believed to be due to the influence of chitosan on the foam structure, where smaller and denser foam cells are thought to contribute to improved impact energy absorption.

Table 6 Flexural properties and impact strength of two-layered corn husk/crosslinked starch composite foams with varying chitosan concentrations.

Chitosan conc. (%)	Flexural properties			Impact strength (J/m²)
	Strength (MPa)	Strain (%)	Modulus (MPa)	
0	10.3 ± 0.1	4.6 ± 0.8	796.0 ± 0.2	139.0 ± 0.3
1	10.7 ± 0.1	3.9 ± 0.7	982.2 ± 0.2	160.8 ± 0.0
3	10.9 ± 0.2	2.7 ± 0.0	989.8 ± 0.0	167.1 ± 0.2

The water absorption of composite laminate foams over 10-30 minutes was investigated, with a comparison made between crosslinked tapioca starch/corn husk foams and chitosan-coated variants (Figure 8). A reduction in water penetration was observed following chitosan application onto the corn husk sheets. This decrease is attributed to chitosan's hydrophobic nature, effectively sealing the pores of the exterior corn husk sheets and limiting water uptake. Notably, the 3 wt% chitosan coating exhibited lower water absorption than the 1 wt% coating, likely due to

the more substantial barrier hindering water molecule diffusion.

Weight loss in crosslinked tapioca starch/corn husk laminate composite foams, with and without chitosan biocoating, is presented in Figure 8. A reduction in weight loss was observed upon chitosan application to the corn husk sheets. This phenomenon is attributed to the hydrophobic nature of chitosan, leading to diminished dissolution or leaching of materials due to reduced water interaction. Furthermore, a progressive decrease in weight loss was recorded

with increasing chitosan concentrations on the corn husk sheet surfaces, suggesting the formation of a more substantial barrier against water interaction with a denser chitosan layer.
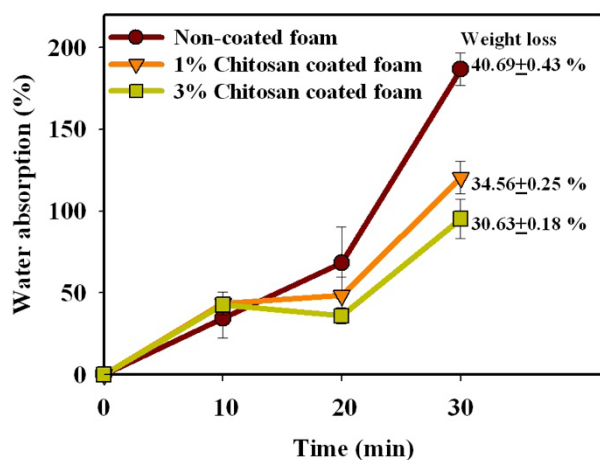

Figure 8 Water absorption and weight loss of crosslinked starch laminate composite foams with 2 layers of corn husk sheet with varying chitosan concentrations.

CONCLUSIONS

This study investigated the morphology, density, crystal structure, flexural and impact strength, thermal stability, and water absorption of crosslinked tapioca starch laminate composite foams, reinforced with corn husk sheets, with and without chitosan coating. Key findings are summarized:

Crosslinked tapioca starch composite foams reinforced with corn husk sheets exhibited an open-cell structure. Smaller, denser foam cells at the edges resulted in a higher density than crosslinked tapioca starch foam. Flexural and impact strength increased with more corn husk layers, attributed to corn husk's good elongation. However, thermal stability was lower than that of crosslinked tapioca starch foam. Corn husk sheets' top and bottom placement restricted foam cell expansion, leading to smaller, denser cells and improved flexural strength and water resistance.

Chitosan coating on corn husk sheets sealed surface pores, impeding water vapor evaporation. This resulted in smaller, denser foam cells, increased flexural and impact strength, and improved water resistance, which was further enhanced by increasing chitosan concentration.

In summary, the structural and functional properties of crosslinked tapioca starch composite foams were significantly influenced by corn husk sheet incorporation and chitosan biocoating. An optimized formulation of two corn husk sheet layers and a 3% chitosan coating demonstrated substantial improvements This particular composition showed a 57.32% reduction in water uptake and marked enhancements in mechanical strength, with a 251.61% increase in flexural strength and a 195.23% rise in impact strength compared to the unmodified foam, highlighting the strong potential of these sustainable materials for various applications, especially sustainable food packaging.

REFERENCES

1. Jambeck JR, Geyer R, Wilcox C, Siegler TR, Perryman M, Andrady A, et al. Plastic waste inputs from land into the ocean. Science [Internet]. 2015;347(6223): 768-71. Available from: http://doi.org/10.1126/science.1260352.

2. Rosemond Z, Chou S, Wilson J, Schwartz M, Tomei-Torres F, Ingerman L, et al. Toxicological profile for styrene. Atlanta, Georgia: Agency for Toxic Substances and Disease Registry; 2010.

3. Tapia-Blácido DR, Aguilar GJ, Teixeira de Andrade M, Rodrigues-Júnior MF, Guareschi-Martins FC. Trends and challenges of starch-based foams for use as food packaging and food container. Trends Food Sci [Internet]. 2022;119:257-71. Available from: https://doi.org/10.1016/j.tifs.2021.12.005.

4. Jiang T, Duan Q, Zhu J, Liu H, Yu L. Starch-based biodegradable materials: Challenges and opportunities. Adv Ind Eng Polym Res [Internet]. 2020;3:8-18. Available from: https://doi.org/10.1016/j.aiepr.2019.11.003.

5. Bénézet JC, Stanojlovic-Davidovic A, Bergeret A, Ferry L, Crespy A. Mechanical and physical properties of expanded starch, reinforced by natural fibres. Ind Crop Prod [Internet]. 2012;37(1):435-40. Available from: https://doi.org/10.1016/j.indcrop.2011.07.001.

6. Kumar Y, Singh S, Saxena DC. A comprehensive review on methods, mechanisms, properties, and emerging applications of crosslinked starches. Int J Biol Macromol [Internet]. 2025;306(2):141526. Available from: https://doi.org/10.1016/j.ijbiomac.2025.141526.

7. Uslu MK, Polat S. Effects of glyoxal cross-linking on baked starch foam. Carbohydr Polym [Internet]. 2012;87(3):1994-99. Available from: https://doi.org/10.1016/j.carbpol.2011.10.008.

8. Phiriyawirut M, Hankham P, Butsukhon R, Pongvichai U. Biomass-based composite foam from tapioca starch/octenyl succinate starch blended with alpha-chitin. Open J Compos Mater [Internet]. 2019;9:355-64. Available from: https://doi.org/10.4236/ojcm.2019.94022.

9. Phiriyawirut M, Mekaroonluck J, Hauyam T, Kittilaksanon A. Biomass-based foam from crosslinked tapioca starch/polybutylene succinate blend. J Renew Mater [Internet]. 2016;4:185-89. Available from: https://doi.org/10.7569/JRM.2015.634121.

10. Bénézet JC, Stanojlovic-Davidovic A, Bergeret A, Ferry L, Crespy A. Mechanical and physical properties of expanded starch, reinforced by natural fibres. Ind Crop Prod [Internet]. 2012;37(1):435-40. Available from: https://doi.org/10.1016/j.indcrop.2011.07.001.

11. Dungani R, Karina M, Subyakto, Sulaeman A, Hermawan De, Hadiyane A. Agricultural waste fibers towards sustainability and advanced utilization: A review. Asian J Plant Sci [Internet]. 2016;15:42-55. Available from: https://doi.org/10.3923/ajps.2016.42.55.

12. Liew KM, Pan ZZ, Zhang LW. An overview of layerwise theories for composite laminates and structures: Development, numerical implementation and application. Compos Struct [Internet]. 2019;216:240-59. Available from: https://doi.org/10.1016/j.compstruct.2019.02.074.

13. Phiriyawirut M, Rodprasert P, Kulvorakulpitak P, Cothsila R, Kengkla N. Pushing the boundaries of starch foams: Novel laminar composites with paper reinforcement. Renew Mater [Internet]. 2025;13(1):101-14. Available from: https://doi.org/10.32604/jrm.2024.056830.

14. Reddy N, YongY. Natural cellulose fibers from corn stover. In: Innovative Biofibers from Renewable Resources [Internet]. Springer Berlin: Heidelberg; 2015. Available from: https://doi.org/10.1007/978-3-662-45136-6.

15. Ibrahim MIJ, Sapuan SM, Zainudin ES, Zuhri MYM. Potential of using multiscale corn husk fiber as reinforcing filler in cornstarch-based biocomposites. Int J Biol Macromol [Internet]. 2019;139:596-604. Available from: https://doi.org/10.1016/j.ijbiomac.2019.08.015.

16. Hazrol MD, Sapuan SM, Ilyas RA, Zainudin ES, Zuhri MYM, Abdul NI. Effect of corn husk fibre loading on thermal and biodegradable properties of kenaf/cornhusk fibre reinforced corn starch-based hybrid composites. Heliyon [Internet]. 2023; 9(4):e15153. Available from: https://doi.org/10.1016/j.heliyon.2023.e15153.

17. Natural Fibers, Biopolymers, and Biocomposites [Internet]. Mohanty AK, Misra M, Drzal LT. 1st ed. Boca Raton: CRC Press; 2005. Available from: https://doi.org/10.1201/9780203508206.

18. Ben Seghir B, Benhamza MH. Preparation, optimization and characterization of chitosan polymer from shrimp shells. J Food Meas Charact [Internet]. 2017;11:1137-47. Available from: https://doi.org/10.1007/s11694-017-9490-9.

19. Aguilar R, Nakamatsu J, Ramírez E, Elgegren M, Ayarza J, Kim S, et al. The potential use of chitosan as a biopolymer additive for enhanced mechanical properties and water resistance of earthen construction. Constr Build Mater [Internet]. 2016; 114:625-37. Available from: https://doi.org/10.1016/j.conbuildmat.2016.03.218.

20. Inthamat P, Karbowiak T, Tongdeesoontorn W, Siripatrawan U. Biodegradable active coating from chitosan/astaxanthin crosslinked with genipin to improve water resistance, moisture and oxygen barrier and mechanical properties of Kraft paper. Int J Biol Macromol [Internet]. 2024;254(2):127816. Available from: https://doi.org/10.1016/j.ijbiomac.2023.127816.

21. Tanpichai S, Witayakran S, Wootthikanokkhan J, Srimarut Y, Woraprayote W, Malila Y. Mechanical and antibacterial properties of the chitosan coated cellulose paper for packaging applications: Effects of molecular weight types and concentrations of chitosan. Int J Biol Macromol [Internet]. 2020; 155:1510-19. Available from: https://doi.org/10.1016/j.ijbiomac.2019.11.128.

22. El-araby A, Janati W, Ullah R, Uddin N, Bari A. Antifungal efficacy of chitosan extracted from shrimp shell on strawberry (*Fragaria × ananassa*) postharvest spoilage fungi. Heliyon [Internet]. 2024;10(7):e29286. Available from: https://doi.org/10.1016/j.heliyon.2024.e29286.

23. Bergel BF, da Luz LM, Santana RMC. Comparative study of the influence of chitosan as coating of thermoplastic starch foam from potato, cassava and corn starch. Prog Org Coat [Internet]. 2017;106:27-32. Available from: https://doi.org/10.1016/j.porgcoat.2017.02.010.

24. Zhang X, Teng Z, Huang R, Catchmark JM. Biodegradable starch/chitosan foam via microwave assisted preparation: Morphology and performance properties. Polymers [Internet]. 2020;12(11):2612. Available from: https://doi.org/10.3390/polym12112612.

25. Akuzawa S, Okada N, Tamaki Y, IkegamiK A, Fujita N, Vilpoux OF, et al. Physicochemical properties of starches isolated from five cassava (Manihot esculenta Crantz) landraces of Brazil. J

Appl Glycosci [Internet]. 2012;59(3):131-38. Available from: https://doi.org/10.5458/jag.jag. JAG-2011_030.

26. Prado KS, Spinacé MAS. Characterization of fibers from pineapple's crown, rice husks and cotton textile residues. Mater Res [Internet]. 2015;18(3):530-37. Available from: https://doi.org/10.1590/1516-1439.311514.

27. Abdellaoui H, Bensalah H, Echaabi J, Bouhfid R, Qaiss A. Fabrication, characterization and modelling of laminated composites based on woven jute fibres reinforced epoxy resin. Mater Des [Internet]. 2015;68:104-13. Available from: Available from: https://doi.org/10.1016/j.matdes.2014.11.059.

28. Arruda Filho AB, Lima PRL, Carvalho RF, Gomes OdFM, Filho RDT. Effect of number of layers on tensile and flexural behavior of cementitious composites reinforced with a new sisal fabric. Textiles [Internet]. 2024;4(1):40-56. Available from: https://doi.org/10.3390/textiles4010004.

29. Faber KT, Evans AG. Crack deflection processes-I. Theory. Acta Metall [Internet]. 1983;31(4):565-76. Available from: https://doi.org/10.1016/0001-6160(83)90046-9.

30. Tamlicha A, Rizal S, Hasanuddin I, Noor MM, Ikramullah I, Nazaruddin N. The effect of number of laminate layers on the ramie E-glass fiber hybrid composite for Jaloe kayoh material. Materials Science Forum [Internet]. 2025;1149: 47-54. Available from: https://doi.org/10.4028/p-d718kw.

31. Hiremath VS, Reddy DM, Mutra RR, Sanjeev A, Dhilipkumar T, et al. Thermal degradation and fire retardant behaviour of natural fibre reinforced polymeric composites- A comprehensive review. J Mater Res Technol [Internet]. 2024;30:4053-63. Available from: https://doi.org/10.1016/j.jmrt.2024.04.085.

32. Kumari S, Rath PK. Extraction and characterization of chitin and chitosan from (Labeo rohit) fish scales. Procedia Mater Sci [Internet]. 2014;6:482-89. Available from: https://doi.org/10.1016/j.mspro.2014.07.062.

Leveraging blockchain for enhancing electronic data interoperability in Thailand's port community system: Barriers and strategic enablers

Chaiporn Thoppae[*] and Tuangyot Supeekit
Faculty of Engineering, Mahidol University, Nakhonpathom 73170, THAILAND
[*]Corresponding author: chaiporn.th@gmail.com, tuangyot.sup@mahidol.edu

ABSTRACT

Thailand's port logistics sector faces significant challenges in achieving secure and interoperable electronic data exchange across stakeholders. Although a standardized Port Community System (PCS) has been promoted, persistent issues-including fragmented digital platforms, security vulnerabilities, and institutional mistrust-impede Electronic Data Interchange (EDI) effectiveness. This study investigates the key barriers (BAR) to EDI implementation and examines how blockchain technology can be a foundational solution to overcome (OVB) them. A structured survey of 350 PCS service users and providers was administered. The data were examined using Confirmatory Factor Analysis (CFA) to check the different parts of the study and Canonical Correlation Analysis (CCA) to look at the relationships between seven identified barrier factors (like infrastructure, legal issues, and budget) and seven strategies to overcome them (such as technology acceptance, organizational readiness, and management support). The first canonical function showed a strong relationship, with a correlation coefficient of 0.652 ($p < 0.01$), meaning that certain organizational actions are closely linked to reducing important barriers. This research is the first empirical study in Thailand to apply multivariate statistical modeling to blockchain-enabled PCS adoption. It contributes methodological rigor through validated measurement models, structural analysis, and practical insight for policymakers, port administrators, and logistics managers. The findings suggest blockchain can enhance transparency, trust, and secure data integration in national logistics infrastructures.

Keywords: Canonical-Correlation Analysis, Maritime NSW, National Single Window (NSW), Port Community System (PCS), Thailand

INTRODUCTION

Thailand's port logistics system is fundamental to its trade competitiveness. While projects such as the Port Community System (PCS) [1], Electronic Data Interchange (EDI) [2, 3], and National Single Window (NSW) have been implemented globally for the better part of the past few decades [4] to improve efficiency in cargo handling processes and reduce paperwork, it is clear from the state of the current port operations that Thailand has many disparate digital platforms in use [5]. User complaints include repetitive manual entry requirements, limited system integration, and delays from multiple operations among the various port authorities, government agencies, and port service providers [6].

Thailand is not unique in this. Most countries around the Asia-Pacific have attempted reforms along these lines with varying degrees of success [7]. While countries like Singapore have developed advanced NSW systems that make it easier to do business [8], others are wrestling with uneven implementation, regulatory loopholes, and a lack of trust among stakeholders.

These problems are slowing Thailand's efforts to create a smooth, paperless trade system, even though the government is stressing the need to improve PCS operations and connect with regional platforms like the ASEAN Single Window.

One of the technologies frequently proposed to address such challenges is blockchain. Its decentralized and immutable structure offers promising solutions to long-standing trust, duplication, and inefficiency issues in PCS and NSW platforms [3, 12, 13]. Empirical studies from Japan, Croatia, and the Asia-Pacific further support blockchain's ability to enhance data integrity and streamline cross-agency logistics operations [7, 14]. The distributed, tamper-proof nature of blockchain is naturally well-suited to environments where multiple organizations must share data [13] and simultaneously access it without depending on a central reference point of control [12]. In port logistics, blockchain technology would enable the automatic execution of transactions, reduce fraud, increase trust and transparency [12, 15], and support real-time visibility throughout the process. In Thailand, however, the practical use of

blockchain in PCS environments has been marginally explored, and its feasibility in practical use is still unclear.

While blockchain technical models have been proposed in global contexts [3, 7, 12-16], there is little empirical work about what conditions need to be in place for the blockchain-enabled EDI to succeed-especially in a country such as Thailand in which organizational, legal, and infrastructure barriers remain considerable. Much of the conversation remains conceptual or technical, failing to consider the barriers service users and providers face on the ground. This diagnostic study aims to identify the socio-organizational preconditions for blockchain adoption in PCS rather than to design a technical solution.

Therefore, this study addresses that gap. Rather than establishing a technical architecture, we identify the organizational and system-level challenges of EDI interoperability in Thailand's PCS (EDI-PCS) and assess how blockchain could best help overcome those challenges. Using a survey of 350 logistics and port stakeholders, we identify key barriers-infrastructure limitations, management resistance, legal uncertainty, and lack of coordination and then rank which strategies are most likely to overcome those barriers [17].

Utilizing Confirmatory Factor Analysis (CFA) [18]. Additionally, using Canonical Correlation Analysis (CCA) [19], we examine these obstacles and suggest ways to overcome them, pointing out specific factors (like support from top management, readiness of the organization, and acceptance of technology) that are statistically linked to better success in implementation.

This research contributes practical insights for decision-makers in Thailand's logistics ecosystem by clarifying the socio-organizational conditions necessary for blockchain adoption. It also lays the groundwork for future technical implementations, offering a roadmap for what must be in place before blockchain can improve port interoperability.

Literature review

As nations modernize their trade and logistics systems, integrating digital technologies like Electronic Data Interchange and Port Community Systems (EDI-PCS) and blockchain has become essential. However, despite global momentum, many countries-particularly in developing regions-continue to face persistent barriers to full system interoperability. This literature review examines the evolution of PCS and EDI platforms, identifies recurring obstacles to their adoption, explores strategies for overcoming these barriers, and evaluates the potential role of blockchain in enhancing transparency and trust. By critically engaging with global and regional studies, this section establishes the empirical and conceptual foundation for the present research and identifies the gaps it seeks to address.

Evolution of PCS, EDI, and NSW systems

Ever since the 1980s, EDI-PCS systems have been at the heart of digital trade reform, with first-generation PCS platforms designed to improve communication and automate documentation between customs, ports, shipping lines, and freight companies [1, 7, 20]. As a result, port communities become more competitive [21]. Thailand followed this global trend by launching a management information system (MIS) in 1998 and EDI-based customs clearance in 2000 [3, 4].

Introducing Thailand's National Single Window (NSW) in 2005 was a significant step toward integrating various government and private-sector systems. Similar systems were deployed across the Asia-Pacific to streamline data exchange and reduce clearance times [10, 11], with Singapore's TradeNet beginning in 1989, followed by Hong Kong's TradeLink in 1997, Japan's Nippon Automated Cargo and Port Consolidated System (NACCS) and South Korea's u-Trade platform in 2003, Indonesia's NSW in 2007, and Malaysia' NSW in 2009 [11].

At the same time, Thailand's National Single Window (THAI NSW) has evolved but still faces operational fragmentation. While paperless customs have reduced processing costs, stakeholder systems often remain disconnected, resulting in duplicated inputs, delays, and inefficiencies.

The development of the Single Window system has been categorized into five progressive levels [11], as illustrated in Figure 1.
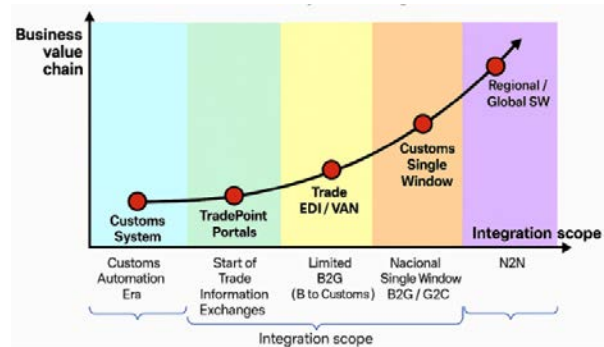
Figure 1 Level of development of integrated government electronic services system (Single Window) [11] (with author enhancements).

Globally, NSW platforms have multiplied. A 2022 UNECE report noted that 74% of Asia-Pacific countries were developing or operating NSWs. The Organization of Islamic Cooperation reported 40% adoption across its members by 2016, attributing progress to improved ICT infrastructure and falling software costs [22].

Thailand's logistics costs reached an estimated USD 70.2 billion in 2023 (14.1% of GDP), suggesting that continued digital reform could yield significant gains [5, 23]. Meanwhile, countries like Singapore (TRADENET), Ghana, and Senegal have served as early benchmarks, setting expectations for faster, more coordinated digital customs ecosystems [8].

Common barriers (BAR) to EDI integration in Port Community Systems (EDI-PCS)

Despite digital infrastructure investments, many nations-Thailand included-struggle to realize the full potential of EDI-PCS platforms. Common challenges include technological mismatches between systems, lack of interoperability, and outdated infrastructure [20, 24]. Organizational barriers, such as resistance to change, low digital literacy, and weak interagency coordination, further complicate integration [25].

Legal and institutional gaps also persist. Trade policies still lack alignment with digital practices, creating uncertainty, particularly in cross-border transactions. In Pakistan, stakeholders reported that while interest in blockchain exists, issues like skills shortages, immature infrastructure, and a lack of government incentives hinder rollout [5]. Corruption and a fear of losing control over opaque processes were also noted as deterrents to full-scale system adoption.

In Montenegro, Peynirci [26] argued that maritime systems favor technical over human-centered design, limiting broader stakeholder buy-in. These structural and cultural challenges are critical to understanding why digital port systems underperform, even when supported by national plans.

Strategies for overcoming (OVB) digital trade barriers

Recognizing these challenges, many governments have issued national logistics development plans. Thailand's Third Logistics Development Plan calls for a unified NSW authority, improved PCS-to-airport integration, and greater use of EDI between government-to-government (G2G) and government-to-business (G2B) actors [27-28].

Strategic interventions include:
- Enhancing top management support to drive system reforms;
- Increasing organizational readiness via training and process reengineering;
- Strengthening infrastructure and legal frameworks for data security and privacy;
- Supporting cross-agency coordination and inter-ministerial integration [9].

Croatia's PCS rollout, for instance, was tied directly to national port competitiveness, while Turkey's system emphasized harmonizing ship-clearance procedures in compliance with IMO standards [24, 26].

Blockchain as a solution to EDI challenges

In response to trust and transparency issues-especially in developing economies-blockchain has emerged as a promising technology. First popularized after the 2008 financial crisis, blockchain offers a decentralized ledger system where transactions are secure, transparent, and immutable [29-31] (Figure 2).

Blockchain's core features-distributed architecture, smart contracts, peer-to-peer transactions, consensus mechanisms, and encryption-make it attractive for supply chains involving multiple stakeholders [3, 32]. When integrated with PCS platforms, blockchain could reduce manual duplication, automate document sharing, and enhance accountability. However, blockchain is not a plug-and-play solution. It requires political will, technical expertise, and readiness at multiple levels. Studies in Pakistan and Turkey underscore that successful deployment hinges on much more than just the technology itself-it depends on governance structures, stakeholder trust, and digital literacy [5, 33].
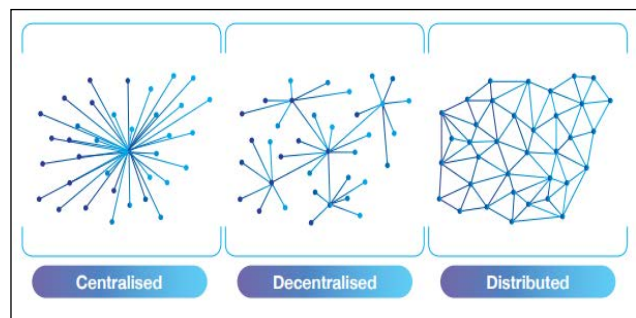
Figure 2 Centralized, decentralized, and distributed systems [31].

Identified gap and study contribution

Although there are many case studies and ideas about integrating PCS, NSW, and blockchain, there are not many large-scale studies that look at the specific challenges and strategies that influence how ready organizations in Southeast Asia are for blockchain-based EDI. Most studies are either theoretical or narrowly scoped to technical implementation.

This study addresses that gap by:
- Surveying 350 stakeholders across Thailand's PCS ecosystem;
- Identifying seven major categories of barriers and seven overcoming strategies;
- Applying CFA to validate these constructs [18];
- Using Canonical Correlation Analysis (CCA) to explore multivariate relationships between barriers and strategies [19].

In doing so, this research provides a grounded, stakeholder-driven perspective on the conditions that must be in place for blockchain adoption in PCS settings to succeed.

The researcher created a research framework, shown in Figure 3, based on the literature review about challenges in connecting electronic information of freight community systems at ports with blockchain technology (BAR) and addressing issues in PCS EDI using blockchain technology (OVB).
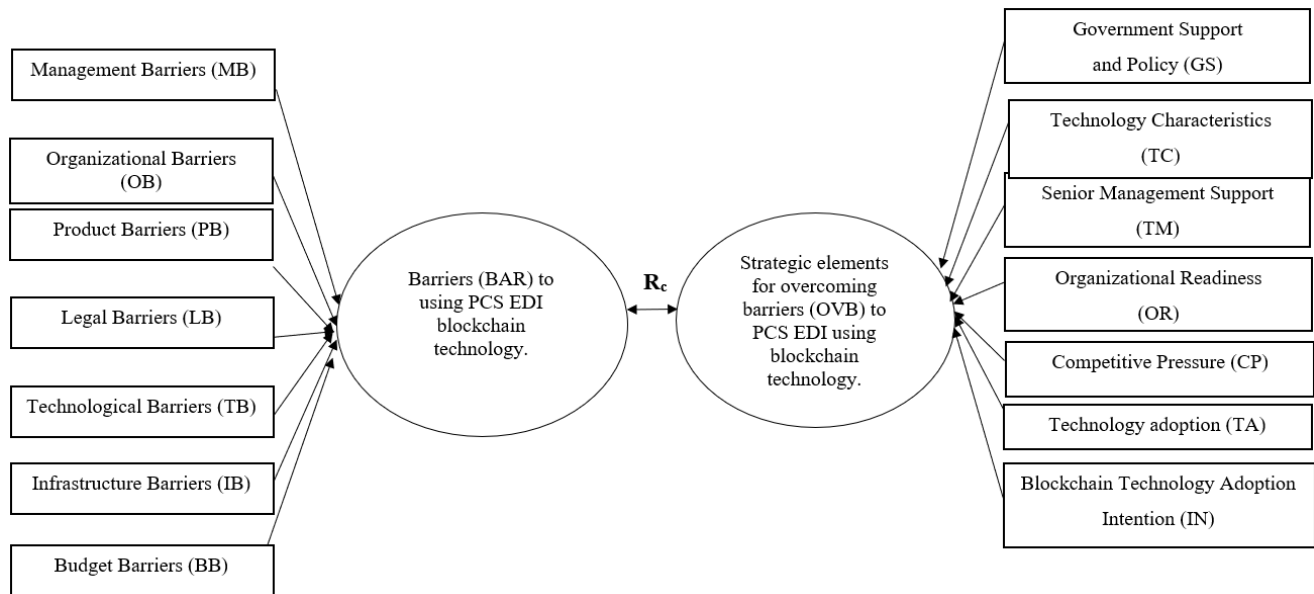
Figure 3 Research framework.

MATERIALS AND METHODS

Population and sample

The study's population is service users and service providers who use EDI systems to transport goods within Thailand's port community system (PCS). The sample group is service users and providers using EDI systems to transport goods within Thailand's port community (PCS) have stated that there is no shortage of recommendations regarding sample sizes using factor analysis. However, various studies have suggested that a ratio method can be used and suggested 10 to 20 questionnaires for each observed variable. Other studies have indicated that for CFA/SEM research, a sample size of 200 or more is sufficient, depending on the model complexity.

Therefore, the study identified 14 observed variables. Using a multiple of 20 to ensure better statistical validity, and when multiplied by 14, the researchers obtained a requirement for 280 questionnaires. However, an effort was made to achieve a higher number, which, after the received questionnaires were audited for usability, was 350.

Research tools

A three-part questionnaire was used as the research tool, which contained items concerning the barriers (BAR) and overcoming barriers (OVB) to EDI within Thailand's PCS using blockchain technology.

Part 1 consisted of a checklist of general information about the respondent's gender, age, education level, and position.

Part 2 and Part 3 included questions about each person's views on the obstacles to EDI (Electronic Data Interoperability), called BAR, and ways to overcome those obstacles, known as OVB, in Thailand's PCS using blockchain technology.

Part 2 and Part 3 consisted of items concerning each individual's opinions about barriers (BAR) and overcoming barriers (OVB) to EDI of Thailand's PCS using blockchain technology, divided into 21 items for BAR and 30 for OVB (51 total).

Opinion measurement

The questionnaire used a 5-level opinion scale that used '5' to indicate the 'highest level' of agreement (4.51-5.00), '4' to indicate a 'high level' of agreement (3.51-4.50), 3' to indicate a 'moderate level' of agreement (2.51-3.50), '2' to indicate a 'low level' of agreement (1.51-2.50), and '1' to indicate the 'lowest level' of agreement (1.00-1.50).

Questionnaire content validity

Five experts participated in the questionnaire's content validity process. [6] Commonly, the index of item-objective congruency (IOC) is suggested for this process [42], with studies suggesting that values of ≤ .50 should be revised or deleted. [36] After completing this process, the authors determined that the final questionnaire had IOC values of 0.60-1.00.

Questionnaire content reliability

After the experts' content validity check, the revised questionnaire was used to try out 30 service users and EDI service providers within Thailand's PCS (Table 1) who did not participate in the final survey. Content reliability is commonly assessed using a Cronbach's alpha coefficient. After the numbers were tallied, the tryout reliability was assessed to have an average value of 0.90. According to [28], α values ≥ .9 are excellent.

Sample questionnaire items

Table 1 shows sample items from the final questionnaire.

Table 1 Sample items for questionnaire constructs.

Construct	Sample Item (English Translation)
Management Barriers (MB)	Executives lack systematic planning for blockchain implementation.
Organizational Barriers (OB)	Our organization lacks a suitable structure to support blockchain technology.
Legal Barriers (LB)	There is no clear regulatory support for blockchain use.
Technological Barriers (TB)	There is a lack of adequate ICT infrastructure to support blockchain applications.
Infrastructure Barriers (IB)	The organization lacks sufficient facilities and systems to support blockchain integration.
Budget Barriers (BB)	The implementation of blockchain faces budget constraints and requires high investment.
Technology Adoption (TA)	Blockchain improves operational efficiency compared to existing systems.
Technology Characteristics (TC)	Blockchain increases data security and reliability for port logistics systems.
Top Management Support (TM)	Executives should participate in blockchain-related policy and decision-making.
Organizational Readiness (OR)	Our organization has sufficient resources and infrastructure to implement blockchain.
Competitive Pressure (CP)	International trade organizations are encouraging the use of blockchain.
Government Support (GS)	Government policy development encourages the adoption of blockchain.
Adoption Intention (IN)	I plan to use blockchain to improve the transparency of information sharing in our logistics system.

Analysis tools

Data analysis tools included descriptive statistics (mean, standard deviation, skewness, and kurtosis) and inferential statistics.

Moreover, a CFA was employed to assess and confirm the construct validity of the hypothesized barrier (BAR) and overcoming-barrier (OVB) constructs. The reason for using CFA is that it can check how accurately the observed variables reflect the hidden constructs suggested in the theoretical framework based on existing research. Since there are known theoretical aspects of the challenges and solutions in blockchain adoption, CFA checks if measuring these fits with the data we have gathered.

A Canonical Correlation Analysis (CCA) was also conducted to examine the multivariate relationships between the two sets of variables-BAR and OVB. CCA is particularly appropriate for this study because it allows us to identify which barriers are most strongly associated with overcoming strategies in blockchain-based EDI systems. This insight is crucial for practical implementation in port community systems, where multiple interdependent factors interact across technical, organizational, and policy domains.

RESULTS AND DISCUSSION

1. Results

1.1 Research framework

Table 2 presents the demographic characteristics of the 350 respondents and their level of understanding of blockchain technology. A notable finding is that over 74% of respondents rated their knowledge of blockchain as moderate to high, indicating a strong foundational awareness that could support adoption initiatives. Furthermore, the relatively balanced gender participation (55% men, 45% women) reflects inclusive engagement across organizational roles. Significantly, 59% of participants were 40 or younger, suggesting that technology adoption efforts may benefit from a workforce that is both adaptive and poised for long-term integration. The high level of education (90% holding a bachelor's degree or higher) reinforces the capability of the target population to understand and implement EDI systems using blockchain.

Table 3 reveals that BAR and strategies for overcoming OVB were rated at a high level, with mean scores ranging from 3.54 to 3.71. Among the barrier categories, Organizational Barriers (OB) were the most significant, likely reflecting internal challenges in

adapting organizational culture and procedures. Infrastructure and Management Barriers (MB) were rated the lowest, perhaps due to ICT access or institutional readiness improvements. On the other hand, Technology Adoption (TA) and Organizational Readiness (OR) received the highest OVB ratings, suggesting that stakeholders perceive internal preparedness and adaptability as critical levers for success. These insights highlight where targeted interventions as leadership buy-in or infrastructure modernization-could yield the most significant returns.

Table 4 shows the CFA results, which indicate strong and important factor loadings (all p < 0.01), confirming the strength of both BAR and OVB concepts. The R^2 values show that Competitive Pressure (CP) (R^2 = 0.83) and Organizational Readiness (OR) (R^2 = 0.70) are very strong indicators in the OVB construct. Similarly, Management Barriers (MB) (R^2 = 0.75) and Technology Barriers (TB) (R^2 = 0.56) contribute substantially to the BAR construct. These findings support the structural validity of the model and indicate where strategic resources should be focused in implementation planning.

Table 5 shows the results of the canonical correlation analysis (CCA) that looks at the relationships between the barrier (BAR) and overcoming-barrier (OVB) concepts. Out of the seven main functions identified, only the first one was statistically significant (Wilk's Lambda = 0.520, χ^2 = 88.186, p < .01), showing a canonical correlation of 0.652, which means there is a shared variance (R^2) of 0.425.

Table 2 Respondents' information (*n* = 350).

Item		*n*	%
Blockchain Technology Knowledge Levels			
5 = The most level		33	9.40
4 = High level		123	35.20
3 = Moderate level		138	39.40
2 = Low level		56	16.00
1 = Lowest level		-	-
	Summation	350	100.00
Gender			
Men		191	54.60
Women		159	45.40
	Summation	350	100.00
Age			
25-30 years		51	14.60
31-35 years		70	20.00
36-40 years		84	24.00
41-45 years		38	10.90
46-50 years		66	18.80
Over 51		41	11.70
	Summation	350	100
Education			
No university degree		34	9.70
Bachelor's degree		226	64.60
Postgraduate		90	25.70
	Summation	350	100

Table 3 Descriptive statistics for BAR and OVB constructs.

Latent Variable	Observable Variables	Mean	SD	Skew.	Kurt.
BAR	MB-Management Barriers	3.54	0.78	-0.15	1.20
BAR	OB-Organization Barriers	3.69	0.59	-0.52	1.38
BAR	PB-Product Barriers	3.64	0.82	-2.07	1.07
BAR	LB-Legal Barriers	3.60	0.89	-2.17	0.74
BAR	TB-Technology Barriers	3.62	0.82	-1.46	0.92
BAR	IB-Infrastructure Barriers	3.54	0.61	-2.45	0.02
BAR	BB-Budget Barriers	3.58	0.70	-2.85	1.11
OVB	TA-Technology Adoption	3.70	0.60	-0.05	1.24
OVB	TC-Technology Characteristics	3.60	0.60	-0.46	0.60
OVB	TM-Senior Management Support	3.56	0.52	-2.80	0.71
OVB	OR-Organizational Readiness	3.71	0.68	-0.42	2.52
OVB	CP-Competitive Pressure	3.61	0.66	-1.39	1.08
OVB	GS-Government Support and Policies	3.62	0.71	-0.18	1.25
OVB	IN-Intention	3.65	0.69	-0.11	0.98

Table 4 CFA results for BAR and OVB constructs.

Observed Variables	b_{sc}	SE.	T	R^2
BAR Variables				
MB	0.68**	0.08	8.89	0.75
OB	0.41**	0.04	11.34	0.48
PB	0.45**	0.05	9.11	0.30
LB	0.56**	0.05	11.19	0.39
TB	0.62**	0.05	12.85	0.56
IB	0.40**	0.03	11.77	0.43
BB	0.44**	0.05	8.21	0.39
OVB Variables				
TC	0.31**	0.03	9.34	0.26
TM	0.33**	0.03	12.86	0.40
OR	0.57**	0.03	19.23	0.70
CP	0.60**	0.03	21.61	0.83
GS	0.59**	0.03	18.34	0.69
IN	0.54**	0.03	17.21	0.61
TA	0.32**	0.03	9.61	0.28

Note: ** $p < 0.01$

Table 5 Canonical Correlation Analysis (CCA) results between BAR and OVB constructs.

CF	CC	Canonical R^2	Wilk's Lambda	χ^2	p-value
1	0.652**	0.425	0.520	88.186	0.000
2	0.225	0.051	0.907	6.398	0.596
3	0.153	0.023	0.955	2.853	0.931
4	0.117	0.013	0.978	1.671	0.966
5	0.688	0.004	0.992	0.552	0.979
6	0.051	0.002	0.997	0.319	0.913
7	0.013	0.001	0.999	0.022	0.800

Note. **Statistically significant at 0.01 level, CF = canonical correlation, CC = Canonical Correlation.

This result suggests a moderately strong multivariate association between the perceived barriers and mitigation strategies. The first function's strength and importance show that one main factor explains how organizations match their views on challenges with their strategic responses.

The non-significance of subsequent functions (p > 0.05) indicates that additional canonical dimensions do not contribute meaningful explanatory power. This highlights the key role of the main canonical relationship, where factors like technological readiness (TA), leadership support (TM), and organizational preparedness (OR) are important in overcoming challenges related to technology, infrastructure, and management.

These findings support the idea that a company's internal skills and flexible leadership are closely connected to how people see both outside and inside challenges, giving a solid basis for focused strategic planning.

Table 6 shows the main weights, loadings, cross-loadings, and shared variance (R²) for Function 1, which is the only important canonical dimension found in earlier analysis. This breakdown reveals how each variable contributes to the multivariate relationship between barriers (BAR) and overcoming barriers (OVB) constructs.

On the independent side (BAR), the most influential contributors are Management Barriers (MB), with a canonical loading of -0.908 (R² = 33.46%) and Infrastructure Barriers (IB) (-0.876, R² = 32.38%). These high loadings suggest that internal organizational and technical challenges are perceived as dominant constraints to EDI-PCS implementation.

On the dependent side (OVB), Technology Adoption (TA) exhibited an exceptionally high canonical weight (0.867), with a canonical loading of 0.991 and R² = 56.54%. This underscores its role as the central success lever, mediating the relationship between internal barriers and strategic outcomes. Other key contributors include Senior Management

Support (TM) and Organizational Readiness (OR), which exceed R² thresholds of 40%.

The cross-loadings show that there is a significant overlap between the two ideas, especially for TA and MB, indicating that trying to address internal challenges with adaptive technologies and active leadership matches well with the obstacles people see. These results strongly support prioritizing technology-oriented interventions and internal capacity building in policy design and implementation roadmaps.

Table 6 Canonical weights (CW), canonical loadings (CL), canonical cross-loading (CCL), and shared variance (R²) for Function 1 between BAR and OVB variables.

	CW	CL	CCL	R²
Independent Variables (BAR)				
MB	-0.417	-0.908	-0.570	33.46
OB	-0.228	-0.903	-0.568	31.25
PB	-0.170	-0.863	-0.544	30.39
LB	-0.096	-0.844	-0.529	27.98
TB	-0.148	-0.710	-0.446	19.85
IB	-0.349	-0.876	-0.552	32.38
BB	-0.021	-0.822	-0.518	26.79
Dependent Variables (OVB)				
TA	0.867	0.991	0.623	56.54
TC	0.189	0.545	0.312	29.25
TM	0.542	0.741	0.464	46.78
OR	0.521	0.736	0.398	44.22
CP	0.312	0.622	0.344	37.21
GS	0.224	0.597	0.300	29.97
IN	0.147	0.494	0.290	28.74

Figure 4 shows the standard correlation model that represents the complex relationship between BAR and OVB variables in using a blockchain-based Electronic Data Interchange Port Community System (EDI-PCS).

The model visually confirms the statistically significant inverse relationship between the two variable sets identified in the CCA (canonical function 1, $R^2 = 0.425$, $p < .01$). Barrier variables, such as Management Barriers (MB) and Infrastructure Barriers (IB), are shown on the left side of the model and are negatively correlated with OVB factors, such as Technology Adoption (TA), Organizational Readiness (OR), and Leadership Support (TM), displayed on the right.

The moderate-to-strong negative canonical loadings indicate that when people feel there are more barriers-especially those related to internal structure and technical infrastructure tend to think that strategies for overcoming these barriers are less effective, and the opposite is also true. Technology Adoption (TA) emerges as the most critical OVB dimension, given its substantial canonical weight and loading observed in Table 5.

This figure is important because it visually confirms the structural alignment and compensatory dynamics between organizational challenges and strategic enablers. Investment in internal capabilities (like digital readiness, leadership engagement, and infrastructure modernization) is reactive and potentially predictive of success in overcoming adoption hurdles.

The CCA model shown here is a useful tool that helps in planning by allowing stakeholders to see which barriers need the most attention and which supports can provide the best benefits for using EDI-PCS with blockchain.
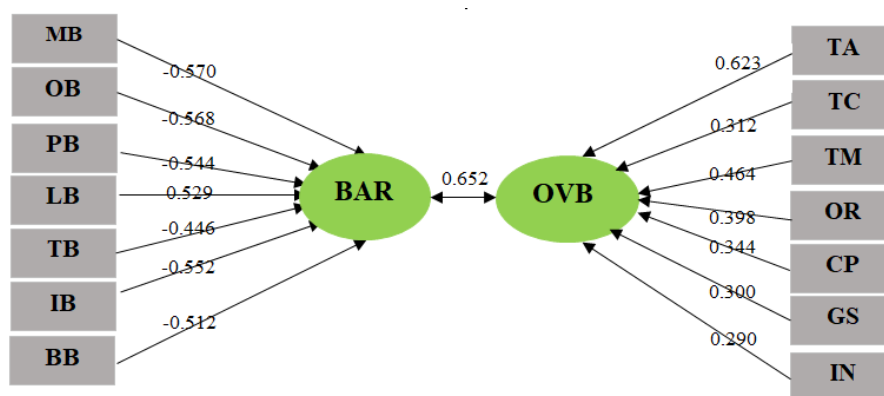
Figure 4 Canonical Correlation Model depicting the relationship between Barrier (BAR) and Overcoming-Barrier (OVB) constructs in implementing a blockchain-based EDI PCS.

2. Discussion

2.1 Barriers (BAR)

The model that explains the obstacles (BAR) to using a blockchain-based Electronic Data Interchange Port Community System (EDI PCS) includes seven main types of barriers: Management Barriers (MB), Organizational Barriers (OB), Product Barriers (PB), Legal Barriers (LB), Technological Barriers (TB), Infrastructure Barriers (IB), and Budget Barriers (BB). These categories highlight challenges like leaders' resistance, inflexible structures, complicated regulations, and technical issues that make using new technologies in port systems hard.

2.2 Overcoming barriers (OVB)

The OVB model points out seven key factors that help with strategy: Technology Adoption (TA), Technology Characteristics (TC), Senior Management Support (TM), Organizational Readiness (OR), Competitive Pressure (CP), Government Support and Policies (GS), and Blockchain Adoption Intention (IN). These factors are a mix of what a company can do internally and outside influences that affect how well blockchain is adopted in PCS [8, 35].

Results from the CCA revealed significant pairings between specific barriers and overcoming variables:

1. Management Barriers (MB) and Technology Adoption (TA) - Canonical loadings of 0.570 for MB and 0.623 for TA suggest that strong technological competencies significantly mitigate managerial resistance. This reinforces the importance of promoting technical literacy and digital confidence among organizational leaders [36].

2. Organizational Barriers (OB) and Government Support (GS) - The combination of OB (0.568) and GS (0.593) shows that having supportive policies and clear rules can significantly lower pushback against change, particularly in organizations with strict structures.

3. Product Barriers (PB) and Blockchain Adoption Intention (IN) - With scores of 0.544 and 0.548, this relationship indicates that a strong intention to use blockchain helps reduce worries about product issues like how well the system works with other systems and its reliability.

4. Technology Barriers (TB) and Senior Management Support (TM) - Canonical loadings of 0.552 for TB and 0.471 for TM highlight the role of engaged leadership in addressing technical complexity. Leaders who actively champion innovation help foster a culture of openness to new technologies [37].

2.3 Canonical correlation analysis (CCA)

The first main function showed a strong statistical link between the barrier and overcoming factors, with a canonical correlation of 0.652 ($p < .01$) and a shared variance of 42.5% ($R^2 = 0.425$). This suggests that nearly half the variation in the barrier set can be explained by the strategic enablers in the OVB set.

These results back up the main idea, showing that certain internal challenges (like resistance from managers or old systems) can be successfully tackled with specific support measures such as leadership backing, alignment with government policies, and focused investments in technology infrastructure. As noted by Tian et al. [37], factors like perceived benefits, external pressure, and senior management trust are vital for successful digital transformation in SMEs [32, 38], an insight that translates well to the port logistics context.

3. Synthesis of findings and implications for practice

This study evaluated the strategic elements for OVB to EDI-PCS using blockchain technology. Through empirical data analysis from 350 stakeholders, we identified seven core barriers and seven corresponding overcoming strategies. Confirmatory Factor Analysis (CFA) validated the construct structure. At the same time, CCA revealed that technology adoption, organizational readiness, and senior management support are statistically and practically linked to key barrier domains such as infrastructure, management, and legal complexity. The findings underscore that blockchain adoption in PCS is not merely a technical undertaking but highly contingent upon socio-organizational readiness. This includes trust in interagency systems [32, 38], legal alignment, and institutional leadership. Our validated analytical framework can be a diagnostic tool for policymakers and logistics authorities to assess blockchain implementation feasibility. These insights are particularly relevant for developing economies where systemic barriers and institutional inertia often impede technological modernization. Addressing these preconditions is vital to unlocking the transformative potential of blockchain for secure, transparent, and interoperable logistics systems.

CONCLUSION

This study empirically analyzed the relationships between key organizational barriers and strategic enablers for Blockchain-based EDI adoption in Thailand's PCS. Using CFA and CCA, the findings highlight how management, infrastructure, and organizational issues are perceived as the most important organizational barriers to achieving sustainable Blockchain-based EDI adoption. In contrast, Technology Adoption, Organizational Readiness, and Leadership Support are strategic enablers of Blockchain-based EDI-PCS adoption.

These findings suggest that blockchain in logistics adoption is as much a socio-organizational issue as a technological one. By synchronizing internal capacity with enabling rules and leadership, Thailand will be in a stronger position to improve the efficacy and trustworthiness of its national logistical platforms.

Future research should concentrate on conducting longitudinal impact assessments, performing cost-benefit analyses, and implementing pilot programs to clarify how blockchain can impact this domain. This study presents a theoretical framework and practical roadmap for stakeholders interested in constructing interoperable and transparent port systems.

Limitations and challenges

This study provides valuable insights into the strategic enablers of blockchain technology adoption within Thailand's Port Community System (PCS) based on empirical research; however, there are a few limitations to this study. Firstly, this study is cross-

sectional, collecting perceptions simultaneously. Hence, we could not consider changes in respondents' organizational readiness or attitudes over time.

Second, the notable sample size ($n = 350$) is statistically sound but limited to Thailand stakeholders in the PCS ecosystem. Therefore, the findings may not generalize to other national contexts or port systems.

Third, since the data in the present study were gathered from self-report surveys, response bias may have emerged because the participants themselves evaluated their organizations' capabilities and awareness of blockchain.

Finally, although Canonical Correlation Analysis (CCA) offers valuable multivariate insights, it does not imply causal relationships. Future longitudinal or experimental studies should be conducted to validate these associations and causality.

Implications and future research

This study has both theoretical and practical implications. These include:

• Organizational Strategy: Blockchain implementation in port logistics is not solely a technical challenge-it requires strategic alignment, institutional agility, and stakeholder buy-in.

• Policy Recommendations: Government support is crucial. In developing economies, institutional inertia and corruption may severely hinder adoption. Policies promoting transparency, interoperability standards, and fiscal incentives can improve adoption rates.

• Managerial Action: Leaders must foster a culture of innovation, provide resources for digital upskilling, and support cross-functional integration.

• Conduct cost-benefit analyses of blockchain deployment in related systems (e.g., NSW, MNSW, secure EDI).

• Investigate the role of anti-corruption initiatives and public-private partnerships in blockchain adoption.

• Undertake longitudinal studies to monitor post-adoption performance and institutional learning trajectories.

This research provides a validated analytical framework and empirical foundation for policymakers, technology leaders, and logistics stakeholders seeking to implement blockchain in national supply chain infrastructure.

DECLARATION OF AI AND AI-ASSISTED TECHNOLOGIES IN THE WRITING PROCESS

The authors utilized ScholarGPT and Grammarly Premium to improve the legibility and clarity of the figures and text during the preparation of this work. The authors assume full responsibility for the publication's content, and they review and edit it as necessary after using this tool or service.

REFERENCES

1. Ollivier PRG, Sahu SP, Saragiotis P. Port Community Systems: Lessons from Global Experience [Internet]. Washington (DC): World Bank Group; 2024 [cited 2025 May 29]. Available from: https://tinyurl.com/9c4r7zx9.

2. Tijan E, Jardas M, Aksentijevic S, Hadzic AP. Integrating Maritime National Single Window with Port Community System-Case study Croatia. In: Proceedings of the 31st Bled Conference; 2018 Jun 17–20; Bled, Slovenia. p. 41. Available from: https://tinyurl.com/2t46hnha.

3. Tijan E, Agatić A, Jović M, Aksentijević S. Maritime National Single Window-A prerequisite for sustainable seaport business. Sustainability. 2019;11(17):4570. doi: 10.3390/su11174570.

4. Pengman H, Kettapan K. The development of a single window integrated with transportation management in ASEAN. Veridian E-J Silpakorn Univ (Humanities Soc Sci Arts) [Internet]. 2018;11(4):879-88. Availablefrom: https://tinyurl.com/2p8v5bcc.

5. Thoppae C, Praneetpolgrang P. Analyzing a blockchain-enabled e-government Document Interchange Architecture (DIA) in Thailand. TEM J. 2021;10(3):1220-27. doi: 10.18421/TEM103-28.

6. Zainuddin N, Hasim NA, Rosman NA, Deraman N. A review on development challenges for an inland port at Malaysia-Thailand border. Quantum J Soc Sci Humanit. 2021;2(6):113-25. doi: 10.55197/qjssh.v2i6.114.

7. Iida J, Watanabe D. Focal points for the development and operation of port community System-A case study of development history in Japan. Asian Transp Stud. 2023;9:100116.

8. Fonseka M, Indraratna K. National Single Window: paving the way for paperless trade [Internet]. 2022 Jan 8 [cited 2025 Apr 18]. Available from: https://tinyurl.com/mry7pxyv.

9. Pamulapati N. Single window legal framework for cross-border trade: 10 case studies [Internet]. Bangkok: United Nations Economic and Social Commission for Asia and the Pacific (UN ESCAP); 2021 [cited 2025 May 28]. Available from: https://hdl.handle.net/20.500.12870/663.

10. Bodhibandhu S, Socatiyanuruk M. Development of Thailand's National Single Window: Current Status and Improvements. RMUTT Glob Bus Econ Rev. 2024;19(1):111-33. doi: 10.60101/rmuttgber.2024.275251.

11. Tsen JTT. Single Windows and Supply Chains in the Next Decade: Ten years of Single Window implementation: lessons learned for the future [Internet]. Global Trade Facilitation Conference; 2011 Oct; Geneva, Switzerland. Available from: https://tinyurl.com/hc55cwp7.

12. Irannezhad E. The architectural design requirements of a blockchain-based port community system. Logistics [Internet]. 2020;4(4):30. Available from: https://www.mdpi.com/2305-6290/4/4/30.

13. Serra P, Fancello G, Tonelli R, Marchesi L. Application prospects of blockchain technology to support the development of interport communities. Computers. 2022;11(5):60. doi: 10.3390/computers 11050060.

14. Jović M. Digital transformation of Croatian seaports. In: 32nd Bled eConference: Humanizing Technology for a Sustainable Society Conference proceedings/Doctoral Consortium; 2019 Jun; Bled, Slovenia. p. 1147-64.

15. Thumburu SKR. Integrating Blockchain Technology into EDI for Enhanced Data Security and Transparency. MZ Comput J [Internet]. 2021;2(1). Available from: https://tinyurl.com/mryfck9z.

16. Caldwell S. Empirical decision-making tools in the Industry 4.0 paradigm: Application to seaports [dissertation]. Liverpool: Liverpool John Moores University; 2024.

17. El Fellah K, El Azami I, El Makrani A. Original Research Article A comparative analysis of blockchain and Electronic Data Interchange (EDI) in supply chain: Identifying strengths, weaknesses, and synergies. J Auton Intell [Internet]. 2024;7(5). Available from: https://tinyurl.com/4cd97tfj.

18. Mulaji SM. Technological, organisational, and environmental factors affecting the adoption of blockchain-based distributed identity management in organisations [master's thesis]. Cape Town (South Africa): University of Cape Town; 2023. Available from: http://hdl.handle.net/11427/38087.

19. Sherry A, Henson RK. Conducting and Interpreting Canonical Correlation Analysis in Personality Research: A User-Friendly Primer. J Pers Assess. 2005;84(1):37-48. doi: 10.1207/s15327752 jpa8401_09.

20. Baigy E, Pan X. Innovation adoption case study and the potential of blockchain on Trade Single Window: Identification of adoption challenges and suggestions for Pakistan Single Window [master's thesis]. Uppsala (Sweden): Uppsala University; 2022. Available from: https://tinyurl. com/mr2deskk.

21. Rodon J, Ramis Pujol J. Exploring the intricacies of integrating with a port community system. In: 19th Bled eConference eValues; 2006 Jun 5-7; Bled, Slovenia. p. 1-15.

22. UNECE. The evolution of the concept [Internet]. 2022 [cited 2025 Apr 18]. Available from: https://tinyurl.com/4h24ezx6

23. Office of the National Economic and Social Development Council (NESDC). Thailand's Logistics Report 2023 [Internet]. Bangkok: NESDC; 2023 [cited 2025 Apr 18]. Available from: https://tinyurl.com/2s2ces7e.

24. Radulovic A. Development of human centred model of single window on the example of Port of Bar, Montenegro. Proc Inst Civ Eng Smart Infrastruct Constr. 2022;1-13. doi: 10.1680/ jsmic.22.00013.

25. Khaslavskaya A, Roso V. Outcome driven supply chain perspective on dry ports. Sustainability. 2019;11(5):1492. doi: 10.3390/su11051492.

26. Peynirci E. The rise of emerging technologies: A quantitative based research on maritime single window in Turkey. Res Transp Bus Manag. 2021;100770. doi: 10.1016/j.rtbm.2021.100770.

27. Remali MZH, Harun M. Malaysia National Single Window: the enforcement Royal Malaysia Custom and Miti liabilities on trade system and logistic sector. Adv Transp Logist Res [Internet]. 2018;1:935-47. Available from: https://tinyurl. com/pya7nphj.

28. Torlak I, Tijan E, Aksentijević S, Oblak R. Analysis of Port Community System Introduction in Croatian Seaports-Case Study Split. Trans Marit Sci. 2020;9(2):331-41. doi: 10.7225/toms.v09.n02.015.

29. Onag G. Thailand confident on achieving industry 4.0 ambition [Internet]. Future IoT. 2021 Aug 2 [cited 2025 Apr 18]. Available from: https://tinyurl.com/akrjezxt.

30. IPCSA. PCS/Port community systems-IPCSA International [Internet]. 2022 [cited 2025 Apr 8]. Available from: https://ipcsa.international/ pcs/pcs-general/.

31. Baran P. On distributed communications: I. Introduction to distributed communications networks [report]. Santa Monica (CA): RAND Corporation; 1964. Report No.: RM 3420 PR. Available from: https://tinyurl.com/2h358s4x.

32. De Filippi P, Mannan M, Reijers W. Blockchain as a confidence machine: The problem of trust & challenges of governance. Technol Soc. 2020;62: 101284. doi: 10.1016/j.techsoc.2020.101284.

33. Kamble S, Gunasekaran A, Arha H. Understanding the Blockchain technology adoption in supply chains-Indian context. Int J Prod Res. 2019;57(7): 2009-33. doi: 10.1080/00207543.2018.1518610.

34. Tran TT, Do QH. Critical factors affecting the choice of logistics service provider: an empirical study in Vietnam. J Asian Financ Econ Bus. 2021;8(4):145-50. doi: 10.13106/jafeb.2021.vol8. no4.0145.

35. Malik MS. Factors affecting the organisational adoption of blockchain technology in Australia: A mixed-methods approach [dissertation]. Ballarat (Australia): Federation University; 2022. Available from: https://core.ac.uk/download/ pdf/572923378.pdf.

36. Clohessy T, Acton T. Investigating the influence of organizational factors on blockchain adoption: An innovation theory perspective. Ind Manage Data Syst. 2019;119(7):1457-91. doi: 10.1108/ IMDS-08-2018-0365.

37. Tian M, Deng P, Wu B. Culture and innovation in the international context: A literature overview. Innovation. 2021;34(4):426-53. doi: 10.1080/ 13511610.2020.1783644.

38. El Khatib M, Mohamad H. Digital Transformation and SMART: The Trust Factor. Int J Theory Organ Pract. 2023;3(2):137-55. doi: 10.54489/ijtop. v3i2.311.

Analysis of plowing patterns and effect on the efficiency of land preparation following rice harvest

Rewat Termkla, Sahapat Chalachai, Wirach Anuchanuruk and Lakkana Pitak*

Department of Agricultural Machinery, Faculty of Agriculture and Technology, Rajamangala University of Technology Isan
Surin Campus, Surin 32000, THAILAND
*Corresponding author: lakkana.ph@rmuti.ac.th

ABSTRACT

This study aimed to examine the effect of different plowing patterns on land preparation efficiency. Three plowing patterns were tested: left-handed plowing, right-handed plowing, and headland plowing. A 90-horsepower tractor fitted with a 7-disc harrow was utilized for the experiments. The analysis of soil properties across all nine plots revealed no significant differences. The average soil moisture content ranged from 15% to 18% (dry basis), while the bulk density of the soil was measured between 1.18 and 1.23 g/cm³. Puncture resistance increased with greater depth. After plowing, the physical properties of the soil, including the average width of the plow furrow and soil depth, were approximately equal, with the width measuring around 127 cm. The depth varied slightly, but both the left-handed and right-handed plowing patterns achieved similar and greater depths compared to the headland plowing pattern. Due to the nature of skip-row plowing, it was necessary to lift and lower the plowshare when beginning a new row. The efficiency of the three methods of land preparation was assessed, with the left-handed plowing pattern demonstrating the highest efficiency, followed by the right-handed pattern, and then the skip-row pattern. The actual work capacities were measured at 2.57, 2.44, and 2.23 rai/hr respectively, while the spatial work efficiencies were 43.34%, 41.60%, and 38.20%. Furthermore, the fuel consumption rates for the three tillage methods did not show significant statistical differences ($p > 0.05$). The left-handed plowing method exhibited the lowest fuel consumption rate, while the skip-row plowing method provided the most consistent working pattern across the field.

Keywords: Tillage patterns, Tractor, Disk plow, Plough furrow, Fuel consumption

INTRODUCTION

Land preparation plays a critical role in crop production, serving as the foundation for optimal plant growth and productivity. Various methods of soil transformation are employed depending on the specific requirements of each cropping system. The selection of an appropriate land preparation method must consider factors such as soil and climatic conditions, the biological characteristics of the crops, the timing of operations, and the costs associated with inputs, machinery, and technology [1,2]. For proper soil preparation, farmers need to plow to an appropriate depth, ensuring that plant residues fall into zones with microbial activity where they can decompose quickly [2-4]. The soil should be plowed to a depth of approximately 150 to 300 millimeters. Therefore, soil plowing is a preliminary tillage operation conducted to break and invert the soil, affecting the structure of the upper soil layer and impacting the soil's ability to perform essential functions and services, such as root growth, gas and water transport, and organic matter turnover [5-7]. As a fundamental step in crop cultivation, plowing improves soil conditions, enhances crop yields, and contributes to the sustainability of agricultural systems and the livelihoods of farmers.

Tilling is the process of altering the condition of the soil to create an environment conducive to plant growth. The three factors related to soil tilling are the energy source (tractor), the soil, and the equipment (disk plow). Choosing the right tractor and equipment for each area requires data on their field performance of the tractor and equipment. Tractors and equipment must be tested in real-world conditions under different working scenarios to prevent severe damage, which will allow for the selection of tractors and equipment that are suitable for specific needs [8]. General field operations include primary tasks such as plowing the main part of the area where crops are to be planted, as well as additional tasks such as headland plowing and the interval for changing rows [9,10]. When the tractor turns into the work area, the downtime depends on the distance traveled during the turn and the average speed of movement [11-13]. Movement in the work area affects

fuel consumption, exhaust gas pollution, and production efficiency. Longer and more complex movements require more fuel, produce more pollution, and reduce production efficiency [14, 15]. For those who are new to plowing, they often encounter difficulties in starting the task, such as not being sure where to begin on the plot and facing problems when having to reverse the plow to collect the remaining parts around the plot because they cannot turn the tractor to plow. Therefore, to ensure that plowing is done smoothly, the entire field must be plowed without gaps and without wasting much time turning around, so it is necessary to have a method of dividing the work. By dividing the area into sections to reduce redundant practices, past practices have shown that fuel use during tillage not only depends on soil conditions, technology and cultivation equipment, and plot size, but also on the shape of the plot [16].

Many studies have proposed methods to optimize tillage paths in rice fields of various shapes. The direction of travel during the tillage is usually determined by the longest edge of the rice field and then continues in a rectangular pattern [17]. For the plowing methods, there are several ways to start depending on the condition of the area and the desired neatness of the work. They can be divided as follows: 1. Circuitous pattern, 2. Headland pattern [18]. The study by Sarkar et al. [19] examined appropriate tillage patterns by considering fuel savings and tillage costs. The patterns studied included circular, straight, and overlapping or traditional tillage. It was found that the circular tillage pattern had the highest fuel consumption rate at a tillage depth of 8 cm. No significant difference was found between the rotational and straight tilling methods. While the rotational tilling method requires the most tilling time, the traditional tilling method is found to be the most fuel-efficient for sandy loam soil. Bekele ZM and Ayanie CG [20] evaluated five tillage patterns based on time taken, plot efficiency, and plot capacity. The experiment was conducted using a completely randomized block design with three replications, considering physical, machine, and time parameters. The experimental results found that the plowing pattern from the rear furrow of the working head was recommended first, as it took less time, had higher efficiency and field capability, and reduced overall operating costs. Next is the mixed plowing method for using multiple machines at once. Kuncoro et al., [21] studied the impact of 5 different plowing patterns on fuel consumption rates. The results showed that different plowing patterns lead to varying times and energy consumption rates. The number of turns is a significant factor affecting these differences. Similar to the findings of Ranjbarian et al. [22], an increase in speed has been reported to enhance the capabilities of plowing equipment. It has been said that increasing the operational speed improves the performance of

the equipment. Fuel consumption decreases when the speed increases from 1.5 km/h to 3 km/h but increases when the speed increases from 3 km/h to 4 km/h. Additionally, it was found that in order to save energy, the size of the tractor and the operating parameters must be matched appropriately with the equipment.

When considering research that studies tillage patterns, the important factors are the appropriate tillage method for the field conditions and the operator's expertise. Therefore, the main objective of this study is to test which tillage method is suitable for the horsepower of the tractor in the test field conditions. The variables considered include the type of tractor, horsepower, and number of plow discs, as well as measuring soil properties to improve the process and increase plowing efficiency, the performance indicators used include work capacity, performance, efficiency, and fuel consumption of the tractor.

MATERIALS AND METHODS

Study of tillage patterns affecting fuel consumption There is a concept of studying and testing work efficiency in three steps, which are: Step 1: Study the plowing patterns for soil preparation in rice fields and examine the soil properties. Step 2: Prepare the plot area for testing the plowing with a 7-disc plow attached to the tractor. Step 3: Record the test results and calculate efficiency. The study process has steps and concepts as shown in Figure 1.
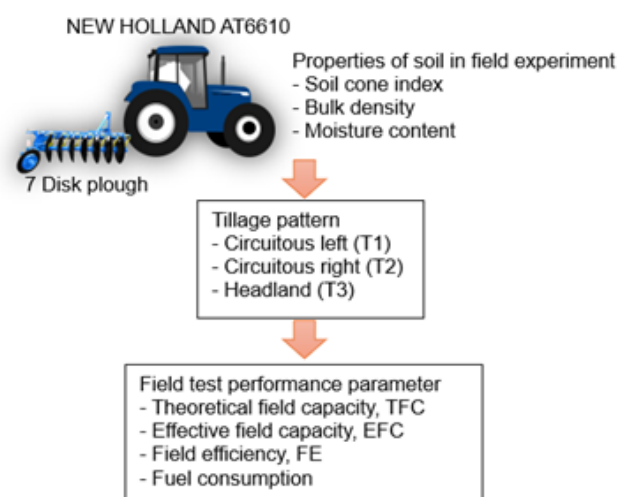
Figure 1 Schematic for study of tillage pattern.

Preparing the testing area

The experimental field was situated at the Agricultural Engineering Department, Faculty of Agriculture and Technology, Rajamangala University of Technology Isan, Surin Campus, Thailand (14.90° N, 103.50° E). The soil at the experimental site was characterized as sandy loam, with a flat terrain predominantly covered by grass and rice stubble. Prior to the initiation of the main field experiment, initial soil samples were systematically collected for

testing from nine points per plot, distributed across the front, middle, and rear sections of each plot, to determine baseline soil moisture content. Concurrently, soil penetration resistance was measured at three depths: 5 cm, 10 cm, and 15 cm, to assess other baseline soil conditions.

Experimental design

The study employed a Randomized Complete Block Design (RCBD). This design was selected to mitigate the impact of potential soil heterogeneity or other environmental gradients across the experimental field, thereby enhancing the precision of treatment comparisons. The experiment was structured into three blocks, with each of the three plowing methods (T1: left-handed plowing, T2: right-handed plowing, and T3: headland plowing) randomly assigned to one plot within each block. This arrangement yielded a total of 9 experimental plots (F1-F9), ensuring three replications for each plowing method. Each individual plot measured 1 rai (1,600 m^2) in area. The spatial layout of the experimental plots and the distribution of treatments are schematically represented in Figure 2. Data collected from these plots were subjected to statistical analysis to evaluate the effects of tillage patterns on fuel consumption.

Block 1	Block 2	Block 3

F1
      T1
	F4
	      T3
		F7
		      T2

F2
      T3
	F5
	      T2
		F8
		      T1

F3
      T2
	F6
	      T1
		F9
		      T3

Figure 2 Field layout of the experimental area.

The initial weight of all samples was measured using a digital scale, and the samples were subsequently dried in a hot air oven at 105°C for 24 hours. After drying, the samples were removed from the oven and their final weights were recorded. The dry basis moisture content of soil (S_{db}) was calculated according to Eq. (1) [23, 24]. And the bulk density as Eq. (2), showing the average moisture content and bulk density as shown in Table 1 for the cone index indicating soil hardness, expressed as force per square centimeter for the conical penetrometer head penetrating the soil. The cone penetration resistance was measured with a dial static cone penetrometer [25, 18]. According to ASAE standards as shown in Figure 3. Then, record the values at different depths, measuring the cone index at 9 different points within the depth range of 0 - 15 cm. Table 2 shows the soil cone index results in the experimental area.

$$S_{db} = \frac{M_1 - M_2}{M_2} \times 100 \qquad (1)$$

Where S_{db} is the dry basis moisture content of soil (%), M_1 is the weight of the soil before drying (g), and M_2 is the weight of the soil after drying (g) [23].

$$\rho_b = \frac{M_s}{V_b} \qquad (2)$$

Where ρ_b is the bulk density of the soil (g/cm^3), M_s is mass or weight of the soil after drying (g), and V_b is total volume of soil (cm^3) [18, 24, 25].
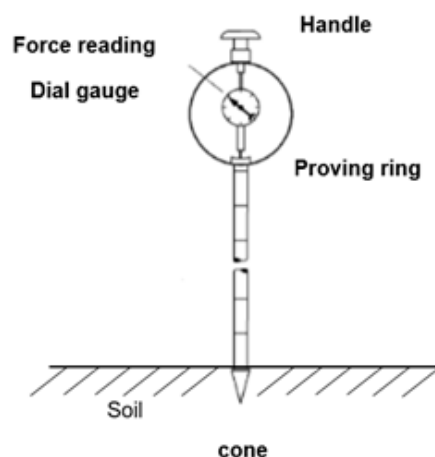
Figure 3 Cone penetrometer test.

Table 1 shows the average moisture content (%db) and bulk density determined for the field used in the experiment.

Field experiment	Moisture content (%db)	Bulk density (g/cm^3)
T1	15.13±0.96	1.23±0.09
T2	17.30±0.34	1.20±0.05
T3	18.07±0.83	1.18±0.06

Table 2 shows the average soil cone index over the 0–15 cm depth range, taken at 9 different spots.

Depth (cm)	Soil cone index (MPa)		
	T1	T2	T3
5	2.87	2.82	3.03
10	3.48	3.57	3.77
15	4.10	4.16	4.26

From the soil moisture within the test plots for the three types of tillage, the moisture content is in the range of 15-18 %db, and the bulk density values are consistent with [20]. It is stated that the acceptable bulk density of soil should be less than 1.3 g/cm³, and the average bulk density of the soil in each plot falls within the recommended range as specified in Table 1. When considering the penetration resistance values in Table 2, it was found that in dry soil conditions and at greater depths, the penetration resistance values were higher [25].

Tractors and soil preparation tools

- *Tractors*

The tractor used as the power source was a NEW HOLLAND AT6610 with a capacity of 90 horsepower, a 4WD drive system, a 4-cylinder diesel engine with direct injection, a cylinder volume of 5,000 cc, an 8-speed forward and 2-speed reverse transmission, a PTO speed of 540 RPM, and a fuel tank capacity of 90 liters, as shown in Figure 4.

Figure 4 Tractor NEW HOLLAND AT6610.

- *Soil preparation tools*

Tilling is the management of soil using machinery to create conditions favorable for plant production. It involves breaking up the compacted surface soil to a specified depth and loosening the soil mass so that plant roots can penetrate and spread through the soil. Tillage can be divided into primary tillage to reduce soil compaction, cover plant residues, and rearrange soil mass. The tools used are called primary tillage implements, which are pulled by tractors and include moldboard plow, disk plow, subsoilers, and chisel plow. As shown in Figure 5, the second tillage is carried out to improve the soil suitable for sowing seeds and planting crops. It is a lighter and more detailed operation. The equipment used includes various types of rakes, tillers, soil levelers, and soil grinders [26-29].

Tillage is the mechanical manipulation of soil to improve conditions for crop growth, typically categorized into primary and secondary tillage. Disk plows, a type of primary tillage implement, are used to break up compacted soil, incorporate residues, and

invert the soil layer. As shown in Figure 5b, the vertical disk plow features concave steel disks (60–80 cm in diameter, and 5–10 mm in thickness). An important characteristic of the vertical disk plow is that all disks are mounted on a single rotating shaft. This type of plow allows adjustment only to the disk angle, while the working depth is generally shallower compared to that of a standard disk plow. The working depth can reach up to 30 cm [30]. In the soil tillage test conducted in this study, the specific characteristics of the disk plow used are presented in Table 3.
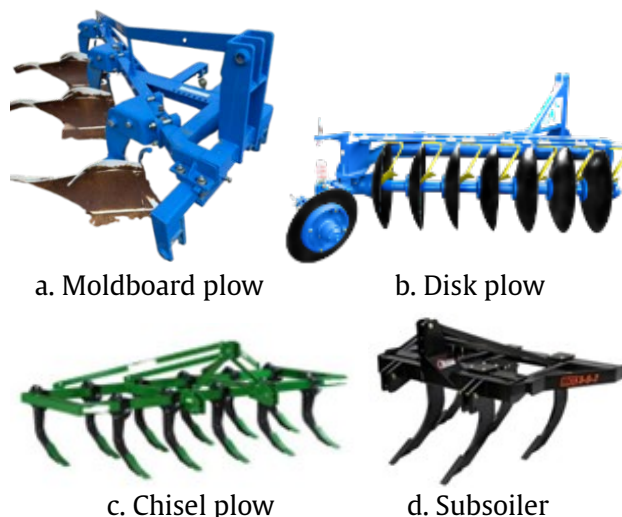

a. Moldboard plow   b. Disk plow

c. Chisel plow   d. Subsoiler

Figure 5 The tillage implements.

Table 3 Specifications of selected tillage implements used for experiment.

Particulars	Disk plow
No. of bottom(s)/tines	7
Operating width	160 cm.
Depth of cut	15-20 cm.
Weight	660 kg.
Power requirement	>70 hp.

Plowing operation procedures

- *Method of dividing the work*

To ensure that plowing is done smoothly, the entire area must be plowed without gaps and without wasting time turning around. Therefore, it is necessary to have a method of dividing the work by splitting the area into sections, each section should not exceed 40 m in width. As for the length, it can be as long as desired, and the longer it is, the better, as it saves time on turning around. After dividing the plot into sections according to the desired width, there should be markers or reference points for dividing the plot into sections and then estimate the area to be used as the headland for turning around [31]. The head cutting will be done after dividing the plot into sections, leaving a space at the head of the plot on both sides, approximately the length of two vehicles. Then, plow in a shallow line,

ensuring that the rear plow touches the ground slightly along the entire length of the plot head on both sides. This serves as a reference point for setting the plow when starting work and lifting the plow when finishing work. If this is not done, it will cause the plow to be misaligned, resulting in uneven furrows and making it difficult to finish the work neatly.
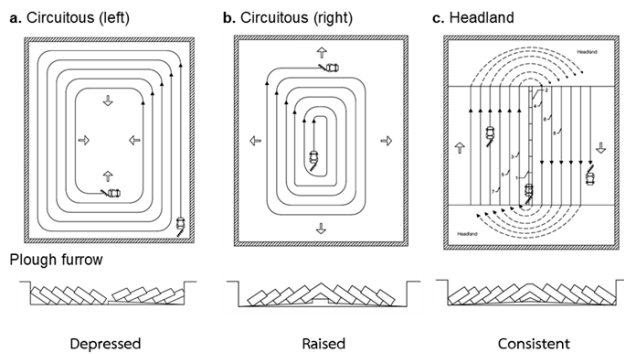

Figure 6 Tillage pattern and plough furrow.

- *Method for testing plowing patterns*
Agriculture in Thailand, especially rice cultivation, mostly involves small-sized rice fields. This leads to significant fuel loss during plowing. It is necessary to apply expertise and methods that can reduce such losses. There are several plowing methods that farmers commonly use. In this test, three methods were evaluated as follows: 1. The circular plowing method includes left-hand circular plowing (Figure 6a). This type of plowing, when repeated annually, will cause water to accumulate in the center of the plot., 2. Right-hand plowing (Figure 6b) is a method where farmers start plowing from the center of the plot and move outward to the edges. This method will cause the center of the plot to become a mound if plowed in the same way every year., 3. The headland plowing method (Figure 6c) begins by dividing the area in half along the length of the plot, leaving equal headland distances on both sides to allow for easy turning on both sides. Mark or aim the stakes to be clearly visible throughout the plowing process. Adjust the plow for the first time by rotating the middle arm so that the last plowshare digs a depth of about 10 cm, marking the first line. Drive the vehicle in low gear. When the vehicle reaches the designated end, lift the plow, turn around, and place the plow so that the left wheel of the vehicle is on the first line of the plowed soil. Adjust the arm to let the plow dig deeper into the soil. Drive the vehicle faster until the end of the field. Lift the plow and turn the vehicle around to plow the third line by placing the right wheel in the second line of the plowed soil. Adjust the middle arm of the plow and loosen the right arm to let the plow dig deeper into the soil. Plow at a slightly higher speed to ensure the plowed soil is smooth and not ridged. Follow the same steps for the fourth and fifth lines

until the area is fully plowed, then finish the task neatly [32].

Field test performance parameter

The performance indicators in this study are the working efficiency of the 7-disc rotary tiller attached to the tractor and the fuel consumption rate, using the following equations.
- *Finding the working speed of a tractor*
The method for determining the appropriate speed for tractor operation involves placing markers at the midpoint of the field, spaced 20 m apart. The speed is calculated by dividing the time taken for the tractor to travel the 20 m distance by the time taken to pass the 20 m markers [33,34]. The starting position was set at least 2 - 5 m away from the first marker to maintain a constant speed before the measurement and data recording.
- *Efficiency*
Theoretical field capacity (TFC) is defined as the maximum area that a machine can cover per unit of time under ideal conditions, without any operational losses. It is calculated using the following Eq. (3).

$$TFC = W \times V \qquad (3)$$

Where TFC is the theoretical field capacity (m²/hr or rai/hr), W is the working width of the implement (m), V is the forward speed of operation (km/h), to convert TFC from square meters per hour to rai per hour, the result is divided by 1,600 (since 1 rai = 1,600 m²) [35].

Effective field capacity (EFC) is the actual working capacity of agricultural machinery or equipment in the field, accounting for various factors that reduce ideal performance. These include reduced operating speed due to field obstacles, environmental conditions, headland turns, or machine downtime. It can be calculated using Eq. (4).

$$EFC = \frac{A}{T_P - T_l} \qquad (4)$$

Where EFC is the effective field capacity (m²/hr or rai/hr), A is total area worked (m²), T_p is time of equipment operation in the field (hr), T_l is the total lost time during field operation (hr).

Field efficiency (FE) is the ratio between actual working capacity and theoretical working capacity of the machine, expressed as a percentage, as shown in Eq. (5).

$$FE = \frac{EFC}{TFC} \times 100 \qquad (5)$$

- *Fuel consumption rate*
The amount of fuel that a machine needs to operate over a certain period or to cover a specific area, which can be calculated in units such as liters per hour or liters per rai. The procedure for measuring fuel consumption involves using a measuring cylinder

to refill the tractor's fuel tank when the work is completed. This can be determined as follows Eq. (6).

$$Fuel\ consumption\ (L.hr^{-1}) = \frac{V}{T} \qquad (6)$$

Where V is the amount of fuel (L), T is time of working (hr) [36].

RESULTS AND DISCUSSION

Effects of soil width and depth from plowing

The width of the plow marks and the depth of the soil are shown in Table 4. The experimental results indicate that the width of the plow marks and the soil depth from the three plowing methods did not differ significantly, with an average plow mark width of approximately 127 cm and soil depth ranging from 13.07 to 14.26 cm , which is consistent with previous studies by Janulevicius et al. [14] and Damanauskas and Janulevicius [17], who concluded that tool dimensions and soil engagement depth are influenced more by implement design and soil conditions than by plowing direction; this consistency in plow width and depth suggests good tool calibration and performance, although differences in soil turning direction among the methods may affect post-tillage soil uniformity and potentially influence subsequent field operations such as planting or fertilization.

Table 4 Results of plowing width and soil depth.

Tillage pattern	Width (cm.)	Depth (cm.)
T1	127.43±2.39	14.24±1.58
T2	127.16±2.31	14.26±1.95
T3	127.18±2.55	13.07±1.51

- *Tillage efficiency*

From the testing of the three tillage preparation methods, the efficiency of the work was calculated.

The test results are shown in Figure 7, which summarizes the average of TFC, EFC, and FE.
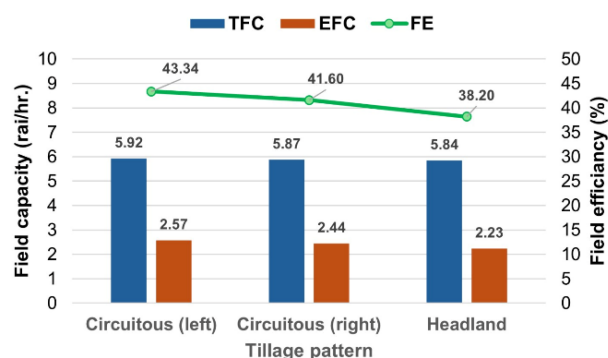

Figure 7 The work efficiency from the three types of land preparation.

Figure 7 shows the field capacity of the three tillage methods: the left-hand tilling method, the right-hand tilling method, and the skip-till method. The actual field capacities were 2.57, 2.44, and 2.23 rai/hr, respectively. When the test results were used to calculate the efficiency of spatial work, it was found that the left-turning plowing pattern had the highest efficiency, as it minimized turning time and maximized continuous tillage. This was followed by the right-turning plowing pattern and the skip-head plowing pattern, with values of 43.34%, 41.60%, and 38.20%, respectively. If a complete plow mark is desired, the entire plot must be plowed. In this case, the headland plowing method provides the most uniform working characteristics across the plot, as shown in the research by Janulevicius et al. [14], who reported that continuous plowing patterns reduce idle turning time at headlands, thus enhancing effective field capacity; the strength of this finding lies in the improved productivity and time savings offered by circuitous patterns, while the limitation remains in the potential for reduced plow uniformity in irregular fields.

Table 5 Results of average fuel consumption.

Treatment	Fuel consumption (L/hr)			Total	Mean
	P1	**P2**	**P3**		
Circuitous (left)	3.90	3.70	3.50	11.10	3.70
Circuitous (right)	3.50	3.90	4.00	11.40	3.80
Headland	4.50	3.95	3.80	12.25	4.08
Block total	11.90	11.55	11.30		
Block mean	3.97	3.85	3.77		
Total				34.75	
Grand mean					3.86

C.V. (%) = 8.59

The effect of fuel consumption rates

The analysis of variance of fuel consumption rates in Table 5 and Table 6 found that the fuel consumption rates of the three plowing methods were not statistically different ($p > 0.05$). When comparing the experimental results, it was shown that the left-turn plowing method had the lowest fuel consumption rate, with an average of 3.70 L/rai. The right-turn plowing method followed, with an average of 3.80 L/rai, and

the headland plowing method had the highest fuel consumption rate, with an average of 4.08 L/hr, respectively. This corresponds with the findings of Janulevicius et al. [14], who reported that headland turns requiring frequent lifting and repositioning of the implement significantly increase fuel consumption.

A notable advantage of the left-hand turning method is its lower energy usage, as it reduces idle motion. In contrast, the headland turning method presents limitations due to increased operational complexity and fuel demand caused by frequent turning and tool repositioning at field boundaries.

Table 6 Results of the variance analysis of fuel consumption rates.

Source of Variation	df	SS	MS	F	p-value
Tillage pattern	2	0.24	0.12	1.10	0.42^{ns}
Fuel consumption	2	0.06	0.03	0.28	0.77^{ns}
Error	4	0.43	0.11		
Total	8	0.73			

Remark: ns- not significant

CONCLUSIONS

The study of soil properties in the test plots, including soil moisture, bulk density, and penetration resistance, found that the soil properties in each plot studied were not significantly different. The average soil moisture test results ranged from 15-18 %db. The bulk density of the soil is 1.18-1.23 g/cm³, and the average penetration resistance is consistent with the moisture content. Which indicates dry soil conditions and increased depth, resulting in higher penetration resistance values. If the penetration resistance values are very high, it may affect work efficiency and increase energy consumption. Physical characteristics of the soil in the test plot after plowing were measured for the average width of the plow marks and the soil depth. In all three plowing methods, the width of the plow marks did not differ, which corresponds to the size of the tool, specifically a 7-disc plow, with a measured width of approximately 127 cm. However, the measured soil depths varied slightly. The left and right circular plowing methods had similar depths, which were greater than the depth of the headland plowing method. This difference may be due to the lifting of the plow when starting to plow at the headland of a new row. The efficiency test of the three tillage preparation methods showed that when the test results were calculated for spatial work efficiency, the left-hand tilling method had the highest efficiency, followed by the right-hand tilling method and the tilling method with headland skipping, with values of 43.34%, 41.60%, and 38.20%, respectively. The fuel consumption rates for the three tillage methods do not differ statistically. However, the method of tilling with headlands has the highest fuel consumption rate but provides the most consistent working conditions across the field.

ACKNOWLEDGEMENT

REFERENCES

1. Beyaert RP, Voroney RP. Estimation of decay constants for crop residues measured over 15 years in conventional and reduced tillage systems in a coarse-textured soil in southern Ontario. Can J Soil Sci. 2011;91:985-95.

2. Vasilenko VV, Vasilenko SV. Rational plough arrangement for plowing with turnover of the soil layer. IOP Conf Ser: Earth Environ Sci. 2021; 624:012105.

3. Al-Suhaibani SA, Ghaly AE. Effect of plowing depth of tillage and forward speed on the performance of a medium size chisel plow operating in a sandy soil. Am J Agri & Biol Sci. 2010;5(3): 247-55.

4. Raper RL. The influence of implement type, tillage depth, and tillage timing on residue burial. Trans ASAE. 2002;45(5):1281-6.

5. Garbout A, Munkholm LJ, Hansen SB. Tillage effects on topsoil structural quality assessed using X-ray CT, soil cores and visual soil evaluation. Soil Tillage Res. 2013;128:104-9.

6. Celik A, Boydas MG, Altikat S. A comparison of an experimental plow with a moldboard and a disk plow on the soil physical properties. Appl Eng Agric. 2011;27(2):185-92.

7. Tang H, Xu C, Xu W, Xu Y, Xiang Y, Wang J. Method of straw ditch buried returning, development of supporting machine and analysis of influencing factors. Front Plant Sci. 2022;13:967838.

8. Ghebrekidan BZ, Koroso AW, Olaniyan AM. Optimization of machine tractor outfit - case of disc plough. J Agric Educ Res. 2024;2(2):1-15.

8

Journal of
Applied **R**esearch on **S**cience
and **T**echnology

9. Seyyedhasani H, Dvorak JS. Reducing field work time using fleet routing optimization. Biosyst Eng. 2018;139:1-10.

10. Backman J, Piirainen P, Oksanen T. Smooth turning path generation for agricultural vehicles in headlands. Biosyst Eng. 2015;139:76-86.

11 Lacour S, Burgun C, Perilhon C, Descombes G, Doyen V. A model to assess tractor operational efficiency from bench test data. J Terramech. 2014;54:1-18.

12. Clough Y, Kirchweger S, Kantelhardt J. Field sizes and the future of farmland biodiversity in European landscapes. Conserv Lett. 2020;13: e1275.

13. Han X, Kim HJ, Jeon CW, Kim JH. Simulation study to develop implement control and headland turning algorithms for autonomous tillage operations. J Biosyst Eng. 2019;44:245-57.

14. Janulevicius A, Sarauskis E, Cipliene A, Juostas A. Estimation of farm tractor performance as a function of time efficiency during ploughing in fields of different sizes. Biosyst Eng. 2019;179: 80-93.

15. Bulgakov V, Ivanovs S, Adamchuk V, Nowak J. Theoretical investigation of steering ability of movement of asymmetric swath header-and-tractor aggregate. In: Proceedings of the 17th International Scientific Conference Engineering for Rural Development. 2018 May 23-25; Jelgava, Latvia. Jelgava: Latvia University of Life Sciences and Technologies; 2018. p. 301-08.

16. Julia ES, George K, Stefan EW, Michiel EDV, Fred AVE, Paul CS. Optimal plot dimensions for performance testing of hybrid potato in the field. Potato Res. 2022;65:417-34.

17. Damanauskas V, Janulevi CA. Validation of criteria for predicting tractor fuel consumption and CO2 emissions when ploughing fields of different shapes and dimensions. AgriEngineering. 2023;5:2408-22.

18. Raper RL, Reeves DW, Burmester CH, Schwab EB. Tillage depth, tillage timing, and cover crop effects on cotton yield, soil strength, and tillage energy requirements. Appl Eng Agric. 2000;16 (4):379-85.

19. Sarkar S, Sultan Mahmud MD, Hasanul Kabir ABM, Kamal Uddin SMD, Muhammad AM. Selection of suitable tillage pattern for fuel economy. Res J Agric For Sci. 2016;4(4):1-4.

20. Bekele ZM, Ayanie CG. Comparative evaluation of alternate ploughing pattern designs at Metahara sugar estate of Ethiopia. Afr J Agric Sci Technol. 2016;4(7):1024-831.

21. Purwoko HK, Halimah SBL, Krissandi W, Ropiudin, Arief S, Susanto BS. Analysis of fuel consumption rate of a rotary power tiller on various tillage patterns. J Teknik Pertanian Lampung. 2023;12 (4):886-98.

22. Ranjbarian S, Askari M, Jannatkhah J. Performance of tractor and tillage implements in clay soil. J Saudi Soc Agric Sci. 2017;16:154-62.

23. Rasheed MW, Tang J, Sarwar A, Shah S, Saddique N, Khan MU, et al. Soil moisture measuring techniques and factors affecting the moisture dynamics: a comprehensive review. Sustainability. 2022;14:11538.

24. Ampanmanee J, Usaborisut P. Compaction properties of silty soils in relation to soil texture, moisture content and organic matter. Am J Agric Biol Sci. 2015;10(4):178-85

25. Moacir TDM, Vanderlei RDS, Anderson LZ, Reimar C. Use of penetrometers in agriculture: a review. Eng Agric Jaboticabal. 2014;34(1):179-93.

26. ASABE Standards. Terminology and definitions for agricultural tillage implements. St. Joseph (MI): ASABE; 2004. S414.1.

27. Claassen SL. Management of tillage equipment on research farms. 3rd ed. Ibadan (Nigeria): International Institute of Tropical Agriculture (IITA); 1995. 33 p.

28. Rao G, Chaudhary H, Singh P. Optimal draft requirement for vibratory tillage equipment using genetic algorithm technique. IOP Conf Ser Mater Sci Eng. 2018;330:012108.

29. Barut ZB, Ozdemir S. A research on metal and metallurgical properties of chisel plough shanks. BIO Web Conf. 2024;85:01007.

30. Novara A, Novara A, Comparetti A, Rodrigo-Comino J, Gristina L. Effect of standard disk plough on soil translocation in sloping Sicilian vineyards. Land. 2022;11(2):148.

31. Tu X, Tang L. Headland turning optimisation for agricultural vehicles and those with towed implements. J Agric Food Res. 2019;1:100009.

32. International Rice Research Institute. Land preparation: plowing patterns [Internet]. Los Baños (Philippines): IRRI; 2025 Mar 25 [cited 2025 Apr 30]. Available from: http://www. knowledgebank.irri.org/ericeproduction/I.a_Plo wing_patterns.htm.

33. East African Community. Agricultural machinery-disc and moldboard ploughs-test methods. Arusha (Tanzania): East African Community; 2023.

34. Abed M, Al-Malik N, Al-Jarrah N, Aljuboori HA, Al-Jawadi RAM. Effect of soil moisture and distance of scraper in field performance of disk plow. Curr Appl Sci Technol. 2023;23(5):1-12.

35. Sriwongras P, Sayasoonthorn S, Maneewan S. Development of a novel sugar cane planter for bud chip as planting material. J KMUTNB. 2020; 30(1):4-15.

36. Ekemube RA, Nkakini SO, Igoni AH, Akpa JG. Evaluation of tractor fuel efficiency parameters variability during ploughing operations. J Newviews Eng Technol. 2021;3(4):88-98.

Evaluation of cylinder shape solar dryer on natural convection heat transfer

Sriwichai Susuk[1*], Rachain Visutthipat[1], Natsacha Inchoorrun[2] and Weerayuth Promjan[2]

[1]Biodiversity Research Center, Research and Development Group for Bio-Industries, Thailand Institute of Scientific and Technological Research (TISTR), Pathum Thani 12120, THAILAND

[2]Expert Center of Innovative Health Food (InnoFood), Research and Development Group for Bio-Industries, Institute of Scientific and Technological Research (TISTR), Pathum Thani 12120, THAILAND

[*]Corresponding author: sriwichai@tistr.or.th

ABSTRACT

This research supports that renewable energy sources were used to power the drying process for design in a solar dryer, leading to the preservation of agricultural products and suitable preservation systems. The drying system involves complex physical atmospheric mechanisms, with relations between the dry air and the moisture content of each product, which affect the performance of solar drying systems. Steady laminar natural convection heat transfer formulas that are accurate based on a boundary-layer have been used to evaluate the flow caused by nonuniform density in an air flow based on dimensionless equations, and natural flow (buoyancy) inside the indirect solar dryer. Results show the heat transfer coefficient for natural convection 5 – 6 $W/m^2 °C$, heat energy 25 - 65 J/s, collector efficiencies 29 - 40.6 % and drying rate 0.18 - 0.98 kg/hr. The heat and mass increased according to dry-air flow through the dryer under trends of solar radiation 312 - 513 W/m^2 and temperatures inside the indirect solar dryer 39.7 - 53.7°C, respectively, as ambient temperature 30.5 - 42.5°C, relative humidity 36 - 52% schedule 08:00 a.m. - 04:00 p.m. (daylight clear sky recorded). Experimentation, a test with a similar climate condition, with an initial moisture content of 85% to the final moisture content of 15% on a wet basis, showed a drying rate of 0.08 - 0.19 kg/hr.

Keywords: Renewable energy, Solar dryer, Laminar natural convection, Boundary-layer, Buoyancy

INTRODUCTION

The sun is an abundant energy source widely utilized, especially for preserving agricultural products, one of the oldest and traditional techniques. As the global world transitions towards green energy sources, solar drying has become an essential technology for sustainable agricultural production, offering a clean energy, more efficient alternative to conventional drying methods, and advantages over traditional methods, including faster drying rates and reduced energy costs. Solar drying is one of the renewable energy sources, desirable as compared to other fossil fuels that pollute the environment (greenhouse effect), not only contributes to a better environment but also gives a strong and sustainable boost to the economy through work opportunities, as well as encourages the safety of agricultural products through preservation systems. Moreover, it is a or rural societies living far from the electric grid. Traditionally solar drying techniques is one of oldest make use of an open space (open sun drying or direct sunlight) is the simplest and cheapest method of drying, However, open sun drying has a various limitation on the long drying time periods, (un control temperature and time), dependence on weather conditions, requires a large space area and physical changes in product such as shrinkage, deterioration of quality by overheating, hostile ambient may lead the products to burn instead of drying affects the color, texture, flavor, loss of nutrient and volatiles components, Furthermore contamination of products from the foreign materials and infestation by insects, birds, rodents and other animals. To overcome the limitation of open sun drying, the improvement and utilization of solar dryers is essential, which involves moisture content in the product, heat and mass transfer phenomenon that removes moisture from a product by passing hot-air flows around it to carry away the released vapor, continues until the vapor pressure of the product and ambient environment are equalized. The designs of solar drying systems include various solar collector configurations, dryer geometries, and air flow mechanisms, which are crucial for efficient drying. Heat transfer equations and dimensionless quantities are required to obtain the air flow rate, especially the heat transfer coefficient. Nevertheless, one of the issues in solar dryer designs is the lack of modeling and dimensionless heat transfer data for optimal process design [1-5].

The objective of this research is carried out calculate under the assumption of steady the boundary and incompressible constant fluid laminar flow conditions to evaluate the performance of the indirect solar dryer, using dimensionless quantities [6] as Nusselt Number, Rayleigh Number, Grashof Number, Graetz Number, Reynolds Number, Prandtl Number, Peclet Number, Pohlhausen and heat transfer equations to analyze heat collector on the vertical and horizontal solar dryer's surface (caused by air buoyancy with different temperatures) and compare the result with the experimental drying with the banana (represent agriculture products).

MATERIALS AND METHODS

Description of solar dryer

The cross-sectional view of the solar dryer uses materials easily obtainable from the local market. Figure 1 shows a diagram of the workflow analysis of the solar dryer vertical cylinder shape, the prototype of the solar dryer cylinder vertical shape, consisting of main parts, material Polycarbonate-bright white color plate 6 mm thick, diameter 0.80 m, and height 0.60 m. Contracture body cover and bottom plate made by SUS304 stainless steel (Food grade material), the cover plate is designed for protecting against overheating, preventing the food from burning instead of drying [5], and it can support the fan, blower, or heater utilized for drying continuously until the finished process. The tray made of SUS304 stainless steel had dimensions of 30 cm width, 30 cm depth, and 32.5 cm height. It has the capacity to accommodate 10 kg of material per batch. The door has been provided at the top, and hot air flows into the dryer through the inlet at the bottom, and leaves through the upper side. The solar radiation is absorbed by the surface and covers approximately 1.25 m^2 of the solar dryer approximately 1.25 m^2.
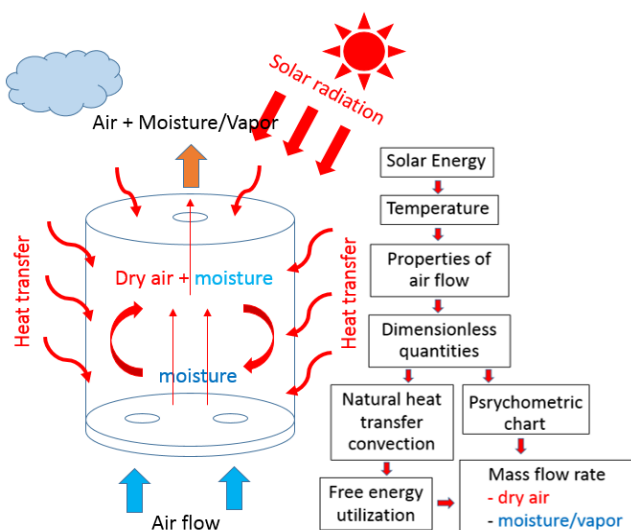

Figure 1 Diagram work flow analysis solar dryer vertical cylinder shape.

Equations and mathematics analysis

Mathematical equations governing natural convection flow and the heat transfer in a solar dryer (cylinder shape) are the dimensionless quantities (boundary conditions) and energy equations. A major problem in heat transfer is the estimation of heat transfer coefficients to be used for design purposes. These hc values must be determined from the fluid's properties and the system's geometry. Equations that describe systems with similar characteristics can be superimposed on each other to form a single expression suitable for all systems. The following dimensionless quantities have been identified and used in correlations involving the heat transfer coefficient equations (1)-(9). The quantity of air needed for drying: Using a psychrometric chart, it is a study of the physical and thermodynamic properties of moist air, i.e., a mixture of dry air and water vapor, and shows the humidity ratio to be kg water/kg dry air, corresponding from the gas laws [7-9].

Experimental set-up

Figure 2 Experimental setup test with a banana fruit.

The temperature profile of the dryer was determined by measuring the hourly temperature. Testing under no load conditions was carried out, measuring the hourly temperature, humidity, solar radiation, and air velocity by Solar power meter model SM206-SOLA, Anemometer model CBzSGHJ001, Temperature & Humidity model L563A, Temperature model TM 1803, Weighting scale model VIGO, and Moisture meter model OHAUS MB23. Experimental studies under no load conditions were conducted in Tambon Khlong Ha, Amphoe Khong Luang, Pathum Tani, Thailand, at a latitude of 14°0'48.46" North and a longitude of 100°31'49.76" East. The temperature profile of the dryer was determined by measuring the hourly temperatures collected between 08:00 a.m. and 04:00 p.m. Experimental studies set-up test with

banana fruit 5 kg (average diameter 3 cm. and length 8 cm.) was reduced from an average 85% to 15% wet basis (Figure 2), specific heat ranged from 1574.0-2506.8 J/kg°C. [10].

Equation of dimensionless

Nusselt Number (Nu) vertical analysis [5,11].

$$\overline{N}_u = 0.68 + \frac{\left(0.67 R_a^{1/4}\right)}{\left(1 + \left(0.492 / \mathrm{Pr}\right)^{9/16}\right)^{4/9}} \tag{1}$$

Nusselt Number (Nu) horizontal analysis [12].

$$\overline{N}_u = \frac{0.544 Ra^{1/5}}{\left(1 + \left(0.477 / \mathrm{Pr}\right)^{3/5}\right)^{1/3}} \tag{2}$$

The Pohlhausen Equation [13].

$$N_{ulam} = 0.664 \, \mathrm{Re}^{1/2} \, \mathrm{Pr}^{1/3} \tag{3}$$

Rayleigh Number (Ra).

$$R_a = \mathrm{P_r} \times G_r \tag{4}$$

Grashof Number (Gr).

$$G_r = \frac{L^3 g \beta \rho^2 \Delta T}{\mu^2} \;,\; \frac{d^3 g \beta \rho^2 \Delta T}{\mu^2} \tag{5}$$

Graetz Number (Gz).

$$G_z = \frac{\pi}{4}\left[\mathrm{Re} \times \mathrm{Pr} \times \left(\frac{d}{L}\right)\right] = \frac{\dot{m}}{k_v \times L} \times C_p \tag{6}$$

Reynolds Number (Re).

$$\mathrm{Re} = \frac{L \times v \times \rho}{\mu} \tag{7}$$

Prandtl Number (Pr).

$$\mathrm{P_r} = \frac{C_p \times \mu}{k} \tag{8}$$

Peclet Number (Pe).

$$P_e = \mathrm{R_e} \times \mathrm{P_r} \tag{9}$$

Heat transfer coefficient (h$_c$).

$$h_c = \frac{\overline{N}_u}{L} \times k_v \tag{10}$$

The quantity of air needed for drying: Using a psychrometric chart and taking input air temperature and relative humidity, it describes the physical and thermodynamic properties of moist air and the hot air drying process, i.e., Parameters for dry-air analysis Table 2. Most common dehydration processes use hot air as the drying medium, as the air delivers heat

to the product to evaporate moisture. The property data are usually provided in charts and tables. The assumption is that there is no heat loss between the collector and the drying. The physical properties of humid air can be determined using the following equation (11-14) [13-15].

$$C_v = 999.2 + 0.1434 T_i + 1.101 \times 10^{-4} T_i^2 - 6.7581 \times 10^{-8} T_i^3 \tag{11}$$

$$\mu_v = 1.718 \times 10^{-5} + 4.620 \times 10^{-8} T_i \tag{12}$$

$$K_v = 0.0244 + 0.6773 \times 10^{-4} T_i \tag{13}$$

$$\rho_v = \frac{353.44}{(T_i + 273.15)} \tag{14}$$

The total collected solar energy, efficiency, and mass flow; the energy input of the solar thermal collector area can be determined from equations (15-17) [16]. Solar collector received maximum solar radiation during test, equation (15), energy output of the solar thermal collector can be determined by equation (16), and efficiency of the solar thermal collector can be defined as the ratio between the useful outputs of energy to the input energy using equation (17). The evaluation of water to be removed from the product using equations (18-20).

$$E_i = I \times A \tag{15}$$

$$\dot{q} = h_c \times A \times \Delta T \; ; \text{The rate of energy collection} \tag{16}$$

$$\eta_c = \frac{\dot{q}}{E_i} \times 100 \tag{17}$$

$$P_A V_A = m_a R_A (T + 273.15) \; ; \text{Gas Laws of air} \tag{18}$$

$$P_w V_w = m_w R_w (T + 273.15) \; ; \text{Gas Laws of vapors} \tag{19}$$

$$\frac{m_w}{m_a} = \frac{0.622 P_w}{P_A} = \frac{0.622 P_w}{P - P_w} \; ; \text{Specific humidity} \tag{20}$$

A major part of energy utilization during drying is for liquid water's evaporation into its vapors (2258 kJ/kg at 101325 Pa), and the average specific heat capacities of drying processes are given as 1970 J/kg°K. A phenomenon of removing liquid by evaporation from a solid, mechanical methods for separating a liquid from a solid are not generally considered drying. The water may be contained in the solid in various forms, like free moisture or bound form, which directly affects the drying rate. These principles are applied, in general, to conventional mechanical drying and are concerned mainly with solar drying. However, it must be noted that conventional drying principles and phenomena are generally independent of the type of energy used [17, 18].

Table 1 Solar radiation, temperature and %RH.

Time	8 am	9 am	10 am	11 am	12 am	1 pm	2 pm	3 pm	4 pm
Solar radiation (W/m²)	312	371	419	465	497	513	494	456	416
Average ambient temp. (°C)	28.5	32.0	34.7	36.6	39.2	40.3	39.6	38.0	35.7
Average temp. (°C) inside dryer	36.7	42.2	46.8	50.3	54.7	56.8	54.5	49.6	43.8
%R.H. ambient outside dryer	52.2	46.7	44.1	40.0	39.9	36.2	38.0	39.5	42.6
%R.H. in dryer no load test	32.6	28.7	26.8	24.3	23.5	20.5	21.9	23.1	25.4

Table 2 Parameters for dry-air analysis.

Item	Average	Units	Equation
C_v	1006.4	J / kg °C	11
μ_v	0.0000194	kg/m.s	12
K_v	0.0277	W/m°C	13
ρ_v	1.103	kg/m³	14
β	0.00311	1/°K	-
P	101325	Pa	standard
P_A	89365	Pa	20
g	9.81	m/s²	standard
R_A	287.1	J/kg°K	standard
A	1.25	m²	-
Nu (vertical)	95.7	dimensionless	1
Nu (horizontal)	212.6	dimensionless	2
Ra (vertical)	0.18×10^{12}	dimensionless	4
Ra (horizontal)	24×10^{12}	dimensionless	4
Gr (vertical)	0.26×10^{9}	dimensionless	5
Gr (horizontal)	0.61×10^{9}	dimensionless	5
Gz	65	dimensionless	6
Re	0.26×10^{5}	dimensionless	7
Pr	0.706	dimensionless	8
Pe	18539	dimensionless	9
m_w/m_a	0.084	kg/kg	20
$\dot{q}$	87.6	J/s	16

RESULTS AND DISCUSSION

No load test (dry air analysis)

The first results described previously of the prototype solar dryer cylinder vertical shape utilized a natural, renewable energy source of heat energy that continuously changed from hour to hour, depending upon the time and sky cover of the day, making it difficult to control. Preliminary evaluation, the air is a gas, as if a medium that can absorb moisture from food products during the drying process by using a solar dryer (heats the air within the collector, raising its temperature and increasing vapor pressure, thus reducing its relative humidity). The information used to evaluate the system is presented in Table 1. The general trend in the profiles of solar radiation and temperatures obtained shows increases from 09:00 a.m. to between 01:00 p.m. and 03:00 p.m. followed by a decrease. On the other hand, relative humidity decreases from 09:00 a.m. to between 01:00 p.m. and 03:00 p.m., then increases, tested without trays and with no load. The hourly variation of the incident solar radiation is shown in Figure 3. During the test period, the test ranged from 312 to 513 W/m². It is clearly seen that the dryer is hottest around midday when the sun is usually overhead. The maximum solar radiation is observed at around 01:00 p.m., 497 to 513 W/m², and the average is 438 W/m², respectively (the dryer is hottest about midday when the sun is overhead). While ambient and inside dryer temperatures varied from 30.5 to 42.5°C and 39.7 to 56.6°C, respectively. Figure

4, the temperature information inside the dryer is within the safe range limit of the drying agricultural processes. (Prakash and Kumer, 2014) [4].
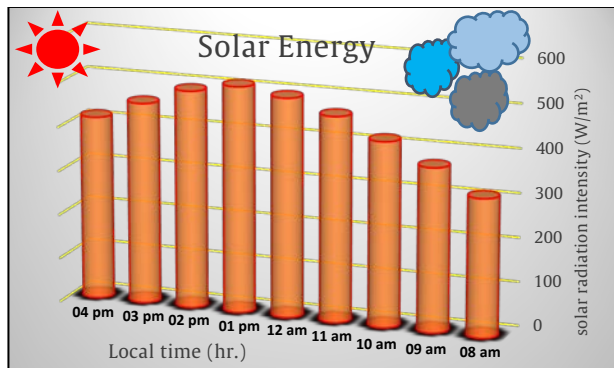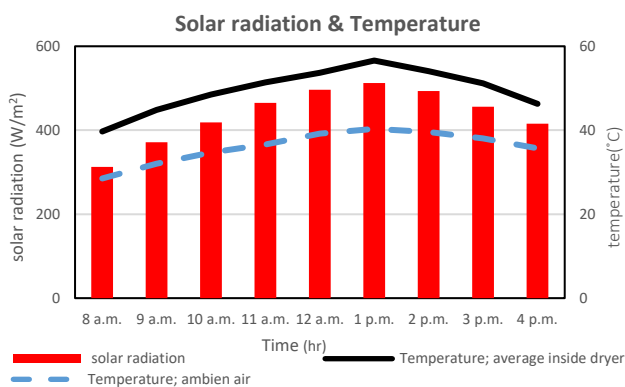

Figure 3 Solar energy radiation.
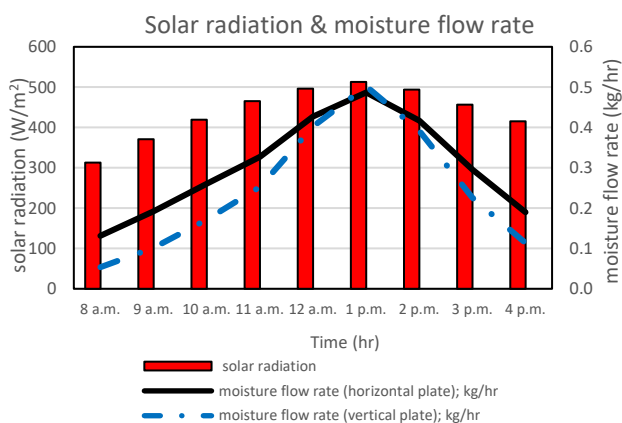

Figure 4 Solar radiation and temperature.

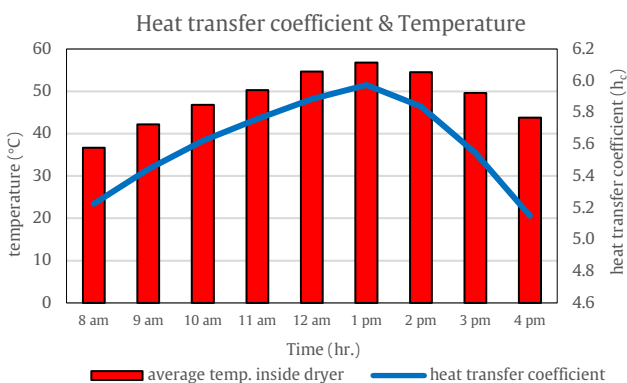**Figure 5** Variation of moisture flow rate.

Figure 6 Heat transfer coefficient and temperature.

The hourly variation of the mass flow rate (dry-air and water) is shown in Figure 5. It was observed that products in the dryer can be dried faster at around 01:00 p.m. because the moisture flow rate strongly depends on the solar radiation effect and the temperature. The effect of the moisture rate increases as solar radiation and temperature increase, and the moisture flow rate is between 0.1 and 0.5 kg/hr, with an average of approximately 0.55 kg/hr, respectively.
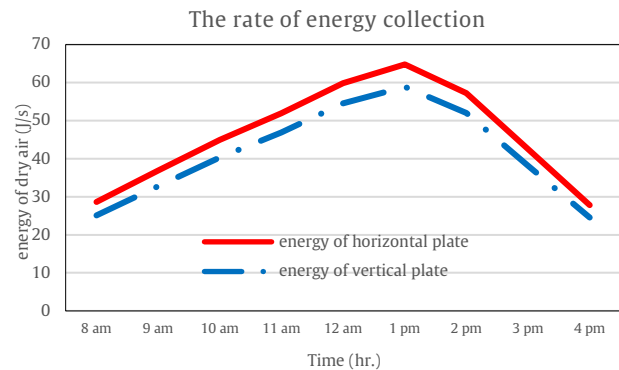

Figure 7 Rate of energy collection (horizontal and vertical plate).

The hourly variation of the heat transfer coefficient of drying is shown in Figure 6. The very heat transfer coefficient values for natural convection are 5.2 and 5.9, with an average of approximately 5.6 W/m² °C, respectively. It can be indicated that the high or low drying system depends on the solar radiation and the temperature effect. The high heat transfer coefficient can achieve high energy, as shown in Figure 7. The rate of energy collection is approximately 25 and 65 J/s, respectively, which can achieve more dry-air volume, leading to dehumidification (moisture removed from the dryer), as shown in Figure 5. This is clearly seen that the maximum heat transfer coefficient similar solar radiation and temperature at around 01:00 p.m.

The hourly variation of thermal (collector) efficiencies on the drying system. It increases as the solar radiation increases Figure 8. This clearly reveals the dependence of the dryer's performance on solar radiation and temperature throughout the system. The efficiency through the solar dryer during the test period was between 29 and 40.6 %. Similar to the previously shown figure at 01:00 p.m., the highest efficiency.

Test with load (banana fruit)

Compering the evaluation of mass flow rate between no load and with load in order to verify performance all information, Experiments banana fruits were dried and the results obtained in drying a banana sample, are shown in Figure 9, It was observed that products in dryer can be dried faster at around 01:00 p.m., testing were carried out drying of banana fruits 5 kg, similar condition no load items. The test

banana slices spent drying time about 27 hours, with an average testing four times per week based on the solar radiation effect on the dryer (08:00 a.m.-04:00 p.m.), beginning 85% was reduced to 15% the basis conditions.
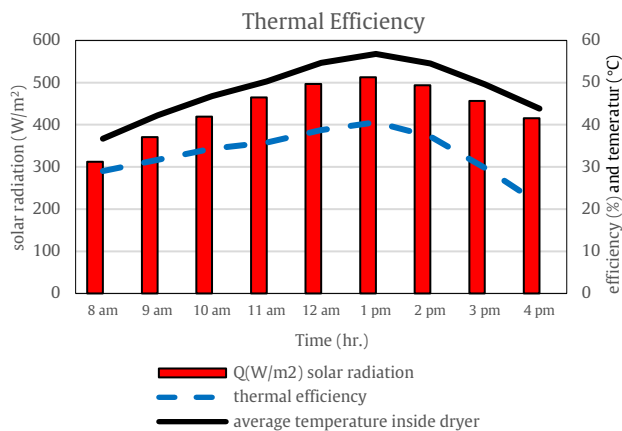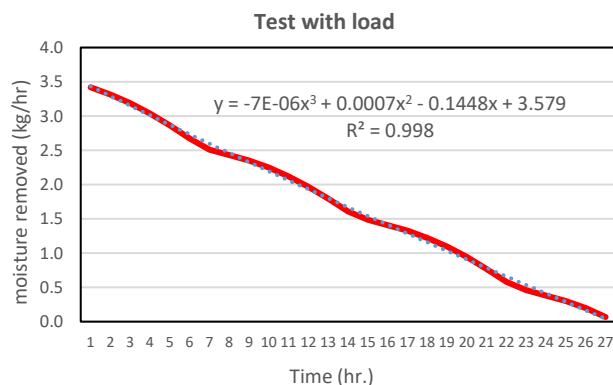

Figure 8 Thermal efficiency.

Figure 9 Experiment test with load (banana fruit).

CONCLUSIONS

This research demonstrates a practical way of cheaply and sanitarily preserving agricultural products by utilizing a solar dryer. The solar dryer does not require high technology, and the maintenance cost is minimal once installed. The evaluation of the solar dryer on natural convection heat transfer based on boundary-layer laminar air-flow has been to evaluate the flow caused by the dimensionless heat transfer correlating equation, which was applied to evaluate the heat transfer along with the cylindrical shape of the indirect solar dryer. Heat transfer equations were also used in this study to evaluate heat and mass transfer across the dryer. All equations and experiments show higher solar dryer and air-flow values were obtained with higher solar radiation values. However, solar dryers have a natural disadvantage; they require too long to dry agricultural products due to the buoyancy and insufficient dehumidification to dehumidify the dryer rapidly. An alternate energy source was used to power the drying process during cloudy days and at night. Improvement in efficiency more than this design can add a solar collector or other renewable heat source utilized for drying continuously during off-sunshine and at night or on rainy.

REFERENCES

1. Aditya A, Pravin A, Jaydeep S. Life cycle assessment and economic valuation of a natural convection solar greenhouse dryer in western maharashtra, India. Journal of Mechanical and Energy Engineering. 2022;6(1):99-106. doi: 10.30464/jmee.2022.6.1.99.

2. Onyinyechi N, Cyprian T, Godwin A, Murphy U, David U, Mathew I, et al. Solar dryers: A review of mechanism, methods and critical analysis of transport models applicable in solar drying of product. Green Energy and Resources. 2025;3(2):100118. doi: 10.1016/j.gerr.2025.100118.

3. Nicholas MM, Kosgei SK, Kiprop E, Dickson K, Yuichi N. Air-flow distribution study and performance analysis of a natural convection solar dryer. American Journal of Energy Research. 2017;5(1):12-22.

4. Eshetu G, Mulugeta AD, Nigus GH, Solomon WF, Maarten V, Petros DT. Importance of integrated CFD and product quality modeling of solar dryers for fruits and vegetables: A review. Solar Energy. 2021;220(466-468):88-110.

5. Habtay G, Buzas J, Farkas I. Heat transfer analysis in the chimney of the indirect solar dryer under natural convection mode. FME Transaction. 2020;48(3):701-06.

6. Romeo TT. Fundamentals of food process engineering. 2th ed. Maryland: Aspen Publishers; 1999.

7. Tonui KS, Mutai EBK, Mutuli DA, Mbuge DO, Too KV. Design and Evaluation of Solar Grain Dryer with a Back-up Heater. Research Journal of Applied Sciences, Engineering and Technology. 2014;7(15):3036-43.

8. Abbas KA, Saleh AM, Lasekan OO, Abbas HA. Significance and application of psychrometric chart in food processing: A review. J Food Agric Environ.2010;8(3):274-8.

9. Girija M. Sola dryer-psychrometry. In: International Conference on Advances in Engineering and

Technology (ICAET-2014); 2014 Oct 11-12; Singapore: International Institute of Engineers; 2014.

10. Bart-Plange A, Addo A, Ofori H, Asare V. Thermal properties of gros Michel banana grown in Ghana. ARPN Journal of Engineering and Applied Sciences. 2012;7(4):478-84.

11. Adelaja AO, Babatope B. Analysis and testing of a natural convection solar dryer for the tropics. Journal of Energy [Internet]. 2013; Available From: https://doi.org/10.1155/2013/479894.

12. Waltham MA. Natural convection heat transfer from an isothermal plate. Thermo. 2023;3:148-75.

13. Mehmet D, Erdem A, Ebru KA. Numerical and experimental analysis of heat and mass transfer in the drying process of solar drying system. Engineering Science and Technology an International Journal. 2021;24(4):236-46.

14. Kamil NÇ, Doğan BS, Ertaç H. Estimation of the experimental drying performance parameters using polynomial SVM and ANN models. European Mechanical Science. 2020;4(3):123-30.

15. Sansaniwal SK, Kumar M. Analysis of ginger drying inside a natural convection indirect solar dryer: An experimental study. Journal of Mechanical Engineering and Sciences (JMES). 2015;9:1671-85.

16. Maundu NM, Kosgei SK, Nakajo Y. Design and analysis of solar dryer for mid-latitude region. Energy Procedia. 2016;(100):98-110.

17. Ji YY, Hee JK, Eun JW, Chan JP. On solar nergy utilization for drying technology. Int J Environ Sci Dev. 2017;8(4):305-11.

18. Oko C, Diemuodeke EO. Analysis of air-conditioning and drying processes using spreadsheet add-in for psychrometric data. Journal of Engineering Science and Technology Review. 2010;3(1):7-13.

Nomenclature

Nu	dimensionless	Nusselt Number (mean value)
Nu$_{lam}$	dimensionless	Nusselt Number (laminar flow)
Ra	dimensionless	Rayleigh Number
Pr	dimensionless	Prandtl Numder
Gr	dimensionless	Grashof Numder
Re	dimensionless	Reynolds Number
Pe	dimensionless	Peclet Number
g	m/s^2	Acceleration due to gravity
β	1/°K	Coefficient of thermal expansion
ρ$_v$	kg/m^3	Density
ΔT	°C	Temperature difference ; (T$_i$ - T$_{am}$)
T$_{am}$	°C	Ambient temperature
T$_i$	°C	Temperature inside dryer
T	°C	Film temperature
v	m/s	Velocity of air
μ$_v$	kg/m.s	Dynamic viscosity
L	m	Length
C$_v$	kJ/kg°C	Specific heat of dry air, at constant pressure

K$_v$	W/m°C	Thermal conductivity
E$_i$	W	Solar energy
t	s	Time
I	W/m^2	Incident insolation
A	m^2	Total collector area
η_c	%	Thermal efficiency
m$_w$	g	mass of water to be dried
h$_{fg}$	kJ/kg	Latent heat of water vaporization
V$_A$	m^3	Volume of dry air
V$_w$	m^3	Volume of vapors
m$_a$	kg	Mass of air
m$_w$	kg	Mass of vapour
P	Pa	Atmospheric Pressure (101.325 kPa)
P$_s$	Pa	Pressure of steam
R$_A$	J/kg°K	Gas constant t = 287.1
R$_w$	J/kg°K	Moisture constant = 461.5
$\dot{q}$	J/s	Energy, rate of heat flow
$\dot{m}$	kg/s	air flow rate
h$_c$	W/m^2°C	Convective heat transfer coefficient

JOURNAL OF APPLIED RESEARCH ON SCIENCE AND TECHNOLOGY

JARST
INSTITUTE OF RESEARCH AND DEVELOPMENT
RAJAMANGALA UNIVERSITY OF TECHNOLOGY THANYABURI

A unified adaptive pure pursuit speed controller with EKF Sensor Fusion for real-world ackermann mobile robots

Nattapong Promkaew[1], Pasan kulvanit[2] and Somboon Sukpancharoen[1]*

[1]Department of Agricultural Engineering, Faculty of Engineering, Khon Kaen University, Khon Kaen 40002, THAILAND
[2]Department of Science Service, Ministry of Higher Education, Science, Research, and Innovation, Bangkok 10400, THAILAND
*Corresponding author: sombsuk@kku.ac.th

ABSTRACT

Accurate trajectory tracking is critical for autonomous mobile robots navigating in outdoor environments. This research presents an enhanced version of the Pure Pursuit algorithm, referred to as Pure Pursuit with Dynamic Steering Control (PP-DSC), which modulates the robot's velocity according to the magnitude of the steering angle while maintaining a fixed lookahead distance. The algorithm was implemented on a four-wheeled robot with Ackermann steering, and localization was achieved by fusing data from the Global Navigation Satellite System Real Time Kinematic (GNSS-RTK), Inertial Measurement Unit (IMU), and encoder data using an Extended Kalman Filter (EKF). Field experiments were carried out on three representative paths: straight line, S-curve, and loop at operational speeds ranging from 1.0 to 3.0 m/s. The results demonstrated that PP-DSC consistently reduced lateral deviation compared to fixed-speed Pure Pursuit. Root Mean Square Error (RMSE) was reduced to 0.9 cm on the straight-line path, and on the S-curve path, RMSE was reduced to 2.1 cm. The RMSE decreased to 1.9 cm for the loop path with PP-DSC, while the 1 m loo kahead configuration exhibited a higher RMSE of 2.7 cm. These findings confirm that steering-based velocity modulation effectively improves path-tracking precision under real-world outdoor conditions.

Keywords: Pure pursuit, Adaptive speed control, ROS 2 Jazzy, GNSS-RTK, Sensor fusion

INTRODUCTION

Getting robots to navigate outdoors reliably has proven harder than expected. Global Navigation Satellite System Real Time Kinematic (GNSS-RTK) should give us the centim-level accuracy achieving approximately ±10 cm precision when conditions are ideal [1, 2]. Unfortunately, real-world deployment rarely offers such luxury. Buildings create shadow zones where signals simply don't reach. Tree canopies scatter Global Positioning System (GPS) signals unpredictably, while atmospheric disturbances add their own errors [3, 4]. Weather conditions also matter; heavy rain or dense fog can significantly degrade signal quality. These problems compound quickly. A robot might lose position fix entirely at the worst possible moment, or see errors balloon far beyond that ±10 cm specification [5].

The obvious solution involves using multiple sensors together [6]. Extended Kalman Filters have become the standard tool for this job, and for good reason. Under normal GPS conditions, the Extended Kalman filter (EKF) provides marginal benefits, perhaps 3% improvement at best. But watch what happens when GPS degrades: suddenly, that same EKF system outperforms GPS-only navigation by 50%

[7]. The filter merges whatever Real Time Kinematic (RTK) data it can get with Inertial Measurement Unit (IMU) measurements (accelerations, rotation rates) and wheel encoder counts. Even if satellites vanish completely, the robot navigates [8, 9]. The mathematics behind EKF involves recursive Bayesian estimation, predicting states based on motion models, then correcting with sensor observations. Granted, the system still faces that fundamental ±10 cm RTK limit, not to mention delays from mechanical steering linkages and control loops. Still, the multi-sensor approach plays to each technology's strengths. GPS anchors the global position, IMUs track rapid movements, and encoders measure distance traveled regardless of satellite availability.

Beyond sensor fusion lies another problem entirely: path planning computation. Dijkstra's algorithm and A* guarantee optimal paths, which sounds great until you realize their computation time explodes with environmental complexity. Add moving obstacles or multiple optimization criteria, and these classical methods become computationally prohibitive for real-time control. Graph-based methods work well for structured environments, but outdoor navigation often involves continuous spaces with irregular obstacles.

This limitation has pushed researchers toward metaheuristic algorithms - optimization methods that mimic biological and physical processes [10,11]. Ant colonies, bird flocks, evolutionary selection - nature solved these problems long ago. These algorithms do not promise perfect solutions like A* does, but they find reasonable solutions much faster and rarely get trapped in local minima [12]. The exploration-exploitation balance proves crucial here; too much exploration wastes time, while excessive exploitation misses better solutions.

Promkaew's recent work makes a compelling case. Their Artificial Bee Colony algorithm found paths 7% shorter than A* while using just 10% of the computation time in indoor navigation tests [13]. The algorithm divides its artificial bees into scouts, workers, and onlookers, each playing different roles in the optimization process. For robots making split-second decisions, efficiency gain matters more than theoretical optimality.

When it comes to following paths, Pure Pursuit dominates the field - primarily because it's so straightforward [14, 15]. Point the robot at a spot ahead on the path, drive toward it, pick a new spot, repeat. Simple enough that basic microcontrollers can run it without breaking a sweat [16]. The geometric interpretation is elegant: the robot follows a circular arc connecting its current position to the lookahead point. The trade-offs become apparent quickly, however, Standard Pure Pursuit reacts sluggishly to sudden path changes and struggles when speeds vary [17, 18]. Various fixes exist: some researchers adjust lookahead distance dynamically [19, 20], others borrow ideas from animal locomotion [21]. Recent work has explored machine learning approaches to tune params automatically. Yet most still run at fixed speeds, which worsens tracking through curves and amplifies any positioning errors [22].

Physics tells us the solution: slow down for tight turns, speed up on straights. The relationship between curvature and safe speed isn't complicated; it follows from basic centripetal force considerations, but implementations rarely exploit it properly [23]. Consider that lateral acceleration equals velocity squared divided by turning radius; exceeding tire friction limits means losing control.

Ackermann-steered robots face extra complications. Unlike differential drive robots that pivot on the spot, Ackermann platforms have minimum turning radii dictated by their geometry [24]. The front wheels must turn at different angles to avoid tire scrubbing - the inner wheel turns sharper than the outer. Handle these constraints correctly and lateral tracking errors drop to 2.5 cm with 60% less computation - impressive gains, though still limited by positioning accuracy [25]. The kinematic model gets more complex too, involving wheelbase length, steering angle limits, and slip considerations. Speed

control deserves more credit than it gets. Yes, faster operation improves productivity, but strategic speed reduction through curves maintains both accuracy and stability [26, 27]. Field tests show that agricultural robots operating at variable speeds complete tasks with fewer path deviations than constant-speed systems. The steering angle directly indicates how much to slow down, making adaptive speed control straightforward to implement [28].

Modern navigation systems work best when sensor fusion, path planning, and control all support each other. Each layer solves specific problems: fusion handles sensor noise and failures, planning finds efficient routes through complex spaces, and adaptive control executes those plans smoothly. The integration challenges shouldn't be underestimated, though - getting these subsystems to communicate effectively requires careful software architecture.

Our contribution is straightforward: the modified Pure Pursuit to slow down based on steering angle while keeping the lookahead distance fixed. An EKF combines GNSS-RTK, IMU, and encoder data to squeeze the best possible performance from that ±10 cm RTK limitation. All experiments were conducted on an Ackermann-steered robot running ROS 2 Jazzy, chosen for its improved real-time capabilities and better hardware abstraction than ROS 1. Three main outcomes emerged from this work. First, the EKF-based navigation system improves raw RTK positioning by fusing complementary sensors. Second, scaling speed with steering demand (while maintaining constant lookahead) enhances Pure Pursuit (PP) tracking, which is particularly noticeable in S-curves and sharp corners. Third, tests across different paths at 1-3 m/s confirm better accuracy and smoother motion than fixed-speed methods. The improvement becomes more pronounced at higher baseline speeds, where the adaptive system prevents the overshooting common with constant-velocity controllers. Section 2 explains our system design, Section 3 details the experiments, Section 4 analyzes results, and Section 5 discusses implications and next steps.

MATERIALS AND METHODS

Hardware architecture and localization sensors

The mobile robot consists of a four-wheel platform with rear-wheel drive and front-wheel Ackermann steering, and its chassis measures 600 mm wide by 1000 mm long. DC motors provide traction, while a servo motor is responsible for steering. An industrial computer manages the robot's control system. Electrical power comes from a 24 V lithium battery (Figure 1).

A router makes wireless communication and system monitoring possible. For localization, the robot uses two GNSS antennas, with an approximate baseline of 1.2 m, antenna A integrated with a 9-axis

IMU (3-axis gyroscope, 3-axis accelerom, and 3-axis magnetom) to enhance positioning accuracy (Figure 2). The wheel encoders attached to both rear motors provide 1024 pulses per revolution, supplying velocity feedback to EKF.
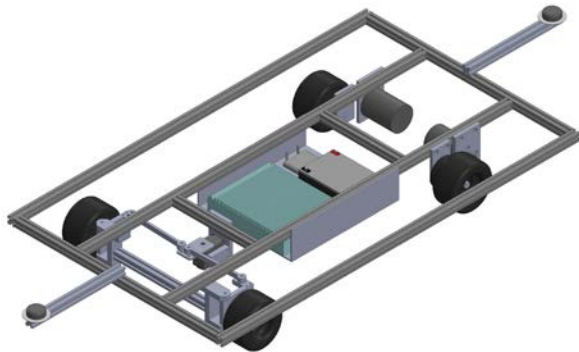

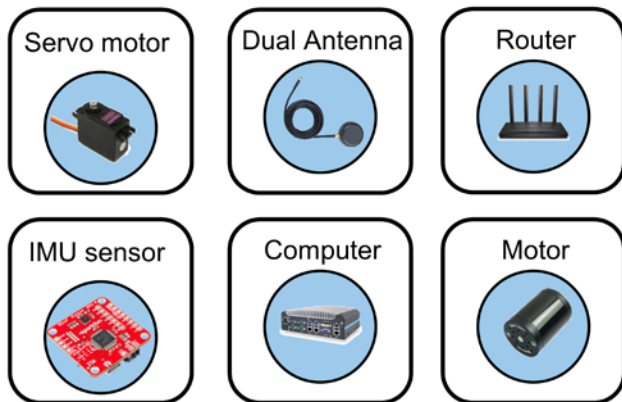**Figure 1** Autonomous Vehicle Component Layout.

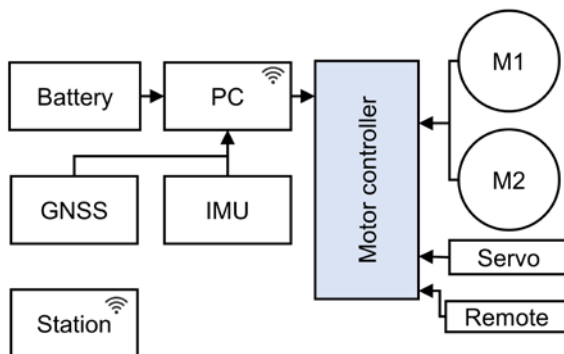**Figure 2** Hardware components of the autonomous vehicle.

Figure 3 Robot system wiring diagram.

The internal wiring layout of the robot is shown in the robot system wiring diagram (Figure 3). A 24 VDC 25 Ah lithium battery supplies power to the entire system, with a DC-DC converter stepping down the voltage to 12 VDC for components that require it. The motor controller connects to two DC motors equipped with encoders for feedback and a servo motor used for steering, which can be operated both automatically and through remote RC signals. Communication between the main computer, motor controller, IMU, and GNSS modules is established

through Controller Area Network (CAN) connections. The industrial computer processes sensor data, issues control commands, and is linked to the RTK receiver. The system communicates with a laptop and a base station via Ethernet and wireless networks. In addition, a 2.4 GHz wireless module is included to support remote operation and monitoring.

Robot development and integration

The robot development process diagram illustrates the steps involved in developing the autonomous robot (Figure 4). Development begins with system design, where the hardware is selected, the power system is planned, and wireless communication is set up. Once these foundations are established, focus shifts to integrating sensors and creating the software. At this stage, data from the GNSS-RTK, IMU, and encoders are combined using an EKF to give the robot an accurate estimate of its position. For navigation purposes, latitude and longitude data are converted into Universal Transverse Mercator (UTM) coordinates. All of these tasks are handled within the ROS 2 Jazzy environment. In the next phase, the robot's path-tracking algorithms are implemented, combining the Pure Pursuit approach with speed adjustment based on steering angle. The process concludes with field testing and a thorough evaluation to confirm that the robot performs as intended (Figure 4).
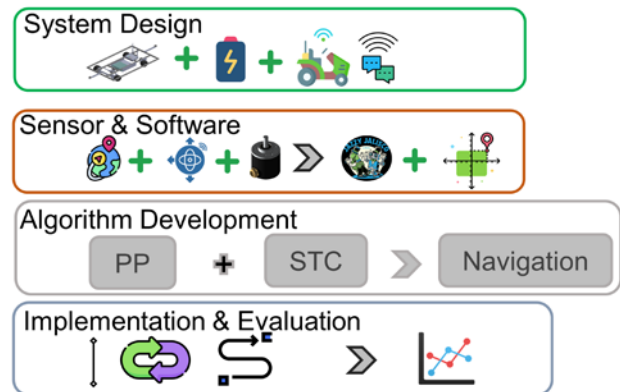

Figure 4 Robot Development Process.

Path tracking and velocity control algorithms

Path tracking for autonomous ground vehicles, most engineers tend to use a mix of geometric and kinematic models to figure out how the robot should steer and control its speed. The kinematic model, for example, is pretty straightforward, but it's proven to be a reliable foundation for many different control methods. One of the techniques that is often used is the Pure Pursuit algorithm. It's gained popularity mostly because it's simple to set up and tends to work well in real-time situations. But as just making the robot steer along the path usually isn't enough. There are plenty of times when the vehicle also needs to adjust its speed, especially if it's about to take a curve. Slowing down in tight turns can make a big difference

4

Journal of
Applied **R**esearch on **S**cience
and **T**echnology

in terms of stability and overall safety, while on straight sections, you can generally get away with going a bit faster. That's why, in many cases, speed is tied to either how much the path is curving or what the steering angle is at a given moment. Putting these strategies together helps make the navigation system more flexible and robust so that the robot can handle all sorts of path shapes and situations it might encounter.
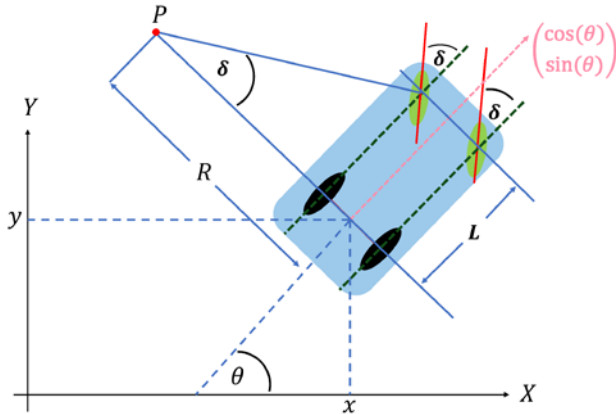

Figure 5 Kinematic bicycle model geometry.
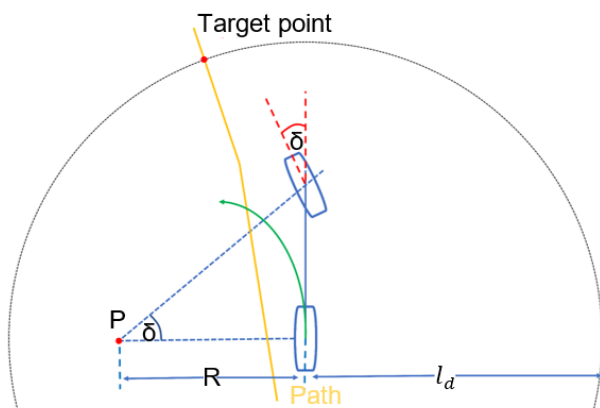
Figure 6 Pure pursuit tracking geometry.

The kinematic bicycle model provides the foundational framework for describing the motion of a car-like robot in the plane (Figure 5). The model is governed by the following continuous-time state-space equations (Eq. 1-4):

$$\frac{d}{dt}\begin{pmatrix} x \\ y \\ \theta \\ v \end{pmatrix} = \begin{pmatrix} v\cos(\theta) \\ v\sin(\theta) \\ v\tan(\delta)/L \\ a \end{pmatrix}$$

(1)
(2)
(3)
(4)

where x and y denote the global position of the rear axle, θ is the heading angle of the vehicle, v is the linear velocity, L represents the wheelbase, δ is the front wheel steering angle, and a is the longitudinal acceleration input. The relationship between the turning radius R and steering angle δ is given by (Eq. 5):

$$R = \frac{L}{\tan(\delta)}$$

(5)

This relationship ensures that changes in the steering angle directly affect the curvature of the vehicle's trajectory.

The Pure Pursuit algorithm is widely adopted for lateral control due to its simplicity and effectiveness (Figure 6).

The algorithm first defines the lookahead distance l_d as a function of the robot's linear velocity (Eq. 6):

$$l_d = K_{dd}v$$

(6)

where K_{dd} is a proportional gain param. To ensure stable tracking, the lookahead distance is constrained within minimum and maximum bounds (Eq. 7):

$$l_{d,min} \leq l_d \leq l_{d,max}$$

(7)

Given a reference path, a target point at lookahead distance is identified in the vehicle frame, and the heading error α is calculated according to (Eq. 8):

$$\alpha = arctan2(y_{tp}, x_{tp})$$

(8)

where (x_{tp}, y_{tp}) are the coordinates of the target point relative to the rear axle. The required turning radius to the target is then determined by the geometric relationship in (Eq. 9):

$$R = \frac{l_d}{2\sin\alpha}$$

(9)

Consequently, the steering angle command for the front wheel is obtained from the Pure Pursuit geometry, as given in (Eq. 10):

$$\delta = \arctan\left(\frac{2L\sin(\alpha)}{l_d}\right)$$

(10)

where L is the wheelbase of the vehicle (m), L_d is the look-ahead distance (m), and α is the geometric heading-error angle between the vehicle's current heading and the target point (rad). This equation determines the curvature of the circular arc that the robot must follow to reach the lookahead point. In practical navigation, stability and safety are further enhanced by dynamically adjusting the robot velocity according to the steering demand. The yaw rate ω is calculated as a function of the current velocity and steering angle (Eq. 3).

The normalized steering demand S is then defined as (Eq. 11):

$$S = \left|\frac{\omega}{\omega_{max}}\right|$$

(11)

where ω_{max} represents the maximum allowable yaw rate (rad/s) determined by the vehicle's kinematic limits. This normalization maps the instantaneous turning rate into the range [0,1], where $S = 0$ corresponds to straight-line motion and $S = 1$ indicates the sharpest turn achievable by the vehicle. The value of S is subsequently used in Eqs. (12) - (14) to

interpolate the commanded velocity between v_{min} and v_{max}.

$$\eta = \frac{S - S_{lower}}{S_{upper} - S_{lower}} \qquad (12)$$

when S lies between S_{lower} and S_{upper}, the interpolated velocity is given by Eq. 13:

$$v_{interp} = v_{min} + (v_{max} - v_{min})\,\eta \qquad (13)$$

Finally, the commanded velocity is expressed as the following piecewise function (Eq.14):

$$v = \begin{cases} v_{min} & S > S_{upper} \\ v_{max} & S < S_{lower} \\ v_{interp} & otherwise \end{cases} \qquad (14)$$

where v_{min} and v_{max} are the minimum and maximum speeds, respectively, and S_{lower} and S_{upper} are threshold values for speed adaptation. By sequentially applying Eqs. 6-14 at each control step, the robot dynamically determines the lookahead distance, computes the target heading and steering commands, calculates the yaw rate and normalized steering demand, and finally sets the appropriate speed for the current path curvature. A rate limiter was applied to the commanded speed to prevent abrupt velocity transitions and ensure smooth motion. The maximum acceleration and deceleration rates were limited to $a_{acc,\,max} = 0.8\ \text{m/s}^2$ and $a_{dec,\,max} = 1.2\ m/s^2$, respectively, based on empirical tuning from field experiments to prevent wheel slip and maintain stability during sharp turns. This integrated control strategy, summarized in Eq. 15 below, enables smooth and robust trajectory tracking:

$$\begin{cases} l_d = clip(K_{dd}v, l_{d,min}, l_{d,max}) \\ \alpha = arctan2(y_{tp}, x_{tp}) \\ \delta = \arctan\left(\dfrac{2L\sin(\alpha)}{l_d}\right) \\ \omega = \dfrac{v}{L}\tan\delta \\ S = \left|\dfrac{\omega}{\omega_{max}}\right| \\ v = \begin{cases} v_{min} & S > S_{upper} \\ v_{max} & S < S_{lower} \\ v_{interp} & otherwise \end{cases} \end{cases} \qquad (15)$$

In this formulation, the lookahead distance l_d is dynamically adapted to the robot's velocity (Eqs. 6, 7), while the target heading angle α and steering command δ guide the robot towards the reference path (Eqs. 8-10). The yaw rate ω and normalized steering demand S (Eqs. 3, 11) are used to interpolate the commanded speed, with η and v_{interp} defined in Eqs. 12 and 13, respectively. The resulting velocity command (Eq. 14) ensures that the robot decelerates smoothly in sharp curves and accelerates on straight or gentle paths, resulting in a comprehensive and unified control law for smooth, adaptive, and reliable path tracking in diverse environments.

Experimental Params and Controller Settings

The key experimental params and control settings used in all tests are summarized in Table 1. These values were kept constant across all experiments to ensure fair comparison and reproducibility.

Table 1 Experimental params and controller settings.

Parameter	Value
PurePursuit gain (K_{dd})	0.8 s
Lower steering threshold (S_{lower})	0.3
Upper steering threshold (S_{upper})	0.9
Minimum speed (V_{min})	1.0 m/s
Maximum speed (V_{max})	3.0 m/s
EKF process noise (Q)	diag (0.05, 0.05, 0.01)
EKF measurement noise (R)	diag (0.2, 0.2, 0.1)

These params were empirically tuned based on preliminary field tests and remained fixed for all subsequent trials.

RESULTS AND DISCUSSION

This section evaluates the performance of the proposed Pure Pursuit with Dynamic Steering Control (PP-DSC) algorithm against the conventional PP method. Experiments were conducted on various trajectories at 1 to 3 m/s using a four-wheeled Ackermann-steered robot (Table 2). Results show that PP-DSC significantly reduces lateral tracking errors and improves velocity stability, especially on curved paths. Compared to the standard PP, PP-DSC provides smoother speed transitions and more accurate path following, demonstrating its effectiveness for real-time autonomous navigation in outdoor environments (Table 3).

In the straight-line tracking experiment, the robot stayed well aligned with the target path. The controller achieved an average lateral error of about 0.7 cm and a maximum deviation below 1 cm during the test (Figure 7, Table 3). This outcome shows that the control system, supported by sensor fusion, can effectively counter minor disturbances and hardware inaccuracies, allowing the robot to navigate smoothly in simple field conditions.

Table 2 Experimental conditions.

Param	Value
Coordinate System	UTM
Control Format	Cartesian (x, y)
Test Scenarios	line path, s-curve path, loop path
Environment	Real-world conditions
Positioning Method	GNSS-RTK

Table 3 Comparison of tracking errors for different algorithms and paths.

Path	Algorithm	Mean (m)	RMSE (m)	STD
Line	PP + DSC	0.007	0.008	0.004
	PP L_d = 1 m	0.001	0.011	0.011
	PP L_d = 5 m	0.01	0.008	0.008
S-curve	PP + DSC	0.006	0.015	0.014
	PP L_d = 1 m	-0.004	0.021	0.021
	PP L_d = 5 m	0.01	0.023	0.021
Loop	PP + DSC	-0.001	0.019	0.019
	PP L_d = 1 m	-0.002	0.027	0.027
	PP L_d = 5 m	-0.001	0.019	0.019

Adjusting the lookahead distance in the Pure Pursuit algorithm noticeably influenced the robot's ability to follow the path accurately. When a 1 m lookahead was used, the robot reacted quickly to directional changes and stayed close to the reference trajectory, with a root mean square error (RMSE) of approximately 1.1 cm. In contrast, a 5 m lookahead resulted in slightly smoother motion but slower response, with an RMSE of about 0.8 cm and a maximum lateral error within 2 cm. These results, illustrated in the tracking comparison (Figure 8), highlight that both lookahead settings provided accurate performance, though the shorter distance yielded more responsive control.
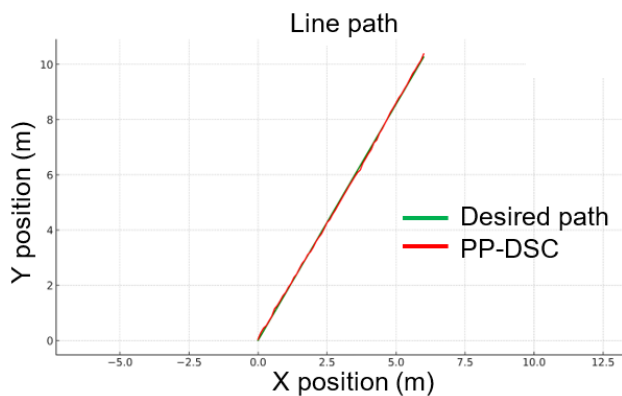
Figure 7 Tracking result on straight-line path.
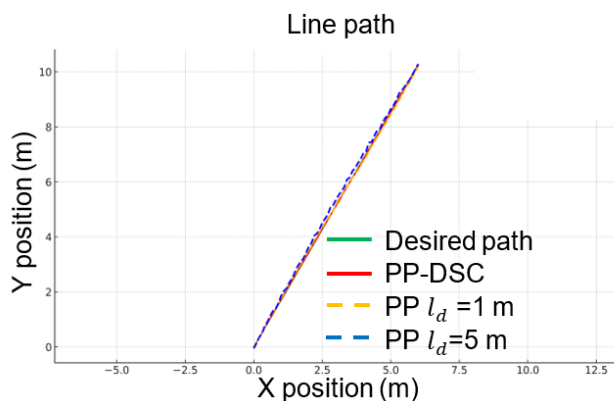
Figure 8 Line path tracking comparison with different lookahead distances.
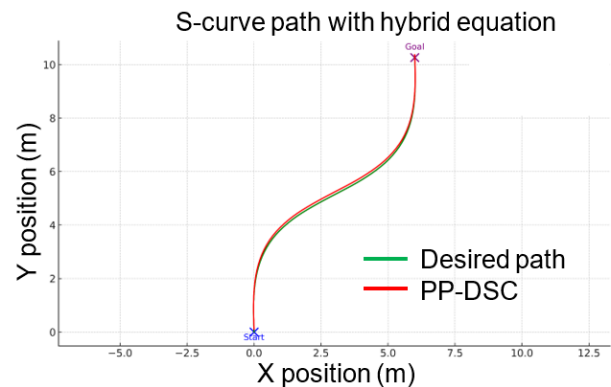
Figure 9 S-curve trajectory tracking using hybrid equation.
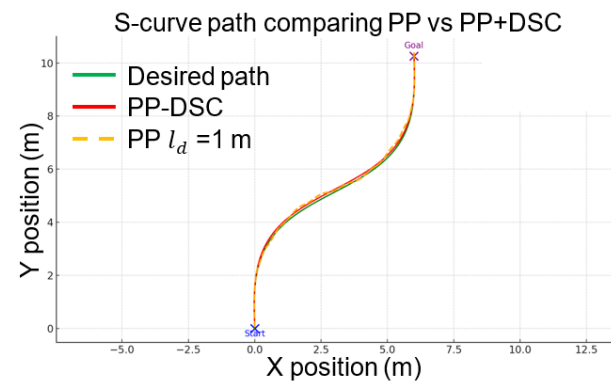
Figure 10 S-curve tracking comparison between PP and PP + DSC.

On the S-shaped trajectory, the robot managed to follow the desired path with steady performance. Despite the continuous change in curvature, the actual path stayed fairly close to the planned one, with lateral deviations mostly within 6-11 cm (Figure 9). These results show that the baseline control approach handles smooth curves reasonably well, though minor overshoot was observed during turning transitions.

To see whether adjusting speed based on steering demand could improve tracking, a comparison was made between standard Pure.

The pursuit and the version were enhanced with speed regulation (Figure 10). When the robot was allowed to slow down in curves, the tracking

line became more stable and stayed closer to the desired path especially in areas with tighter turns. The maximum lateral error was reduced by about 20% compared to the fixed-speed case, and the robot's motion appeared smoother overall.
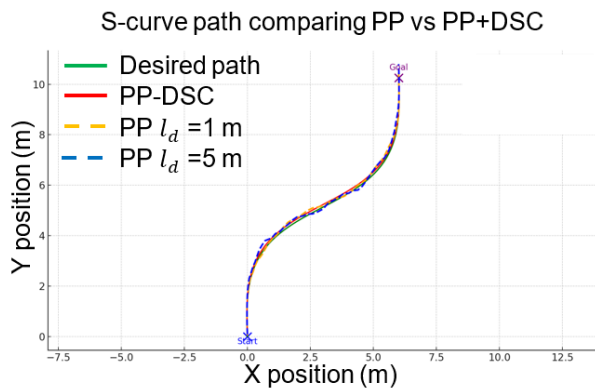

Figure 11 S-curve tracking: PP vs PP + DSC.

As the evaluation continued, both 1 m and 5 m lookahead distances were tested with the speed-adjusted controller (Figure 11). The robot successfully followed the S-curve in both cases. However, the shorter lookahead allowed it to stay slightly closer to the reference trajectory. The average tracking error with 1 m was approximately 2.1 cm, while the longer distance produced a comparable error of 2.3 cm. In addition, the 5 m setting resulted in smoother motion but slightly delayed responses near the curve transitions where quick steering corrections were required. These observations indicate that a shorter lookahead, combined with speed adaptation, provides marginally better responsiveness without sacrificing overall path smoothness.

As the evaluation continued, both 1 m and 5 m lookahead distances were tested with the speed-adjusted controller (Figure 11). The robot successfully followed the S-curve in both cases. However, the shorter lookahead allowed it to stay slightly closer to the reference trajectory. The average tracking error with 1 m was approximately 2.1 cm, while the longer distance produced a comparable error of 2.3 cm. In addition, the 5 m setting resulted in smoother motion but slightly delayed responses near the curve transitions where quick steering corrections were required. These observations indicate that a shorter lookahead, combined with speed adaptation, provides marginally better responsiveness without sacrificing overall path smoothness.

The robot was tested on a loop path to evaluate how well it could maintain accuracy through continuous curvature. As shown in the first plot (Figure 12), the actual path closely followed the planned one. Most of the lateral error remained within a 5-8 cm range, and there were no sharp oscillations or drift, even after multiple turns. The controller handled smooth transitions well without overcorrection or instability.
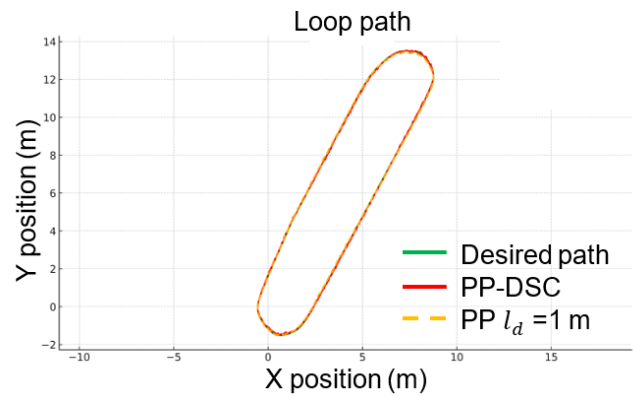

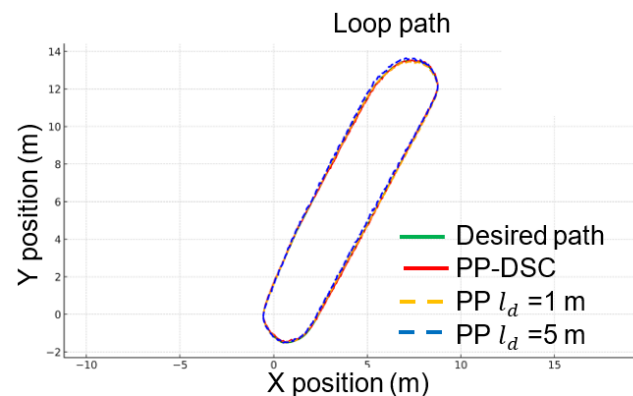**Figure 12** Loop path tracking using 1 m lookahead.

Figure 13 Loop path tracking with different lookahead distances.
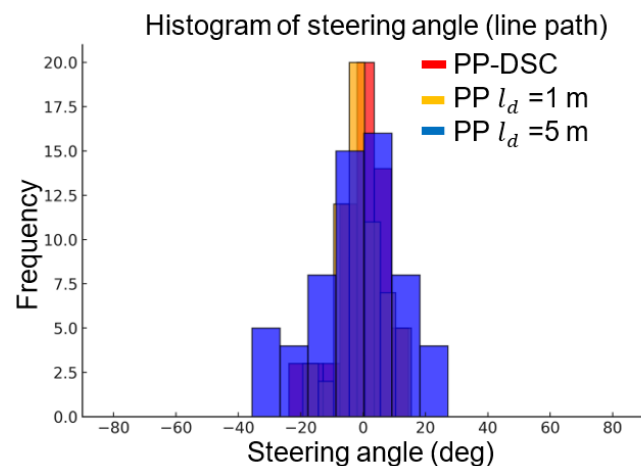

Figure 14 Steering angle distribution on line path.

To understand how the lookahead parameter influenced this behavior, both 1 m and 5 m settings were compared under the same conditions (Figure 13). Although both settings allowed the robot to complete the loop, the shorter lookahead kept the trajectory slightly tighter in curved segments. With the 1 m configuration, the RMSE was approximately 2.7 cm, while with the 5 m configuration it was 1.9 cm. The longer lookahead produced smoother steering and less oscillation, particularly near the top and bottom of the loop where heading corrections were more pronounced. Overall, the shorter lookahead yielded quicker response, whereas the longer distance

provided greater smoothness and stability through the curves.

In the straight-line test, steering angles remained close to zero throughout the trajectory, consistent with expectations for a path with no curvature (Figure 14). The actual robot data and both simulated cases using 1 m and 5 m lookahead distances showed similar results. Most values clustered tightly between -5 and +5 degrees, with minimal spread. Since the path did not require significant turning, all methods produced nearly identical steering behavior.

The loop path, which includes continuous curved segments, resulted in a wider range of steering angles (Figure 15). The actual steering values were concentrated mostly between ±20 degrees. When comparing the two lookahead settings, the 1 m configuration showed a narrower distribution, while the 5 m version introduced more variance and occasional steering commands that extended beyond ±30 degrees. This suggests that the longer lookahead led to less responsive adjustments, especially in curve entry and exit zones.
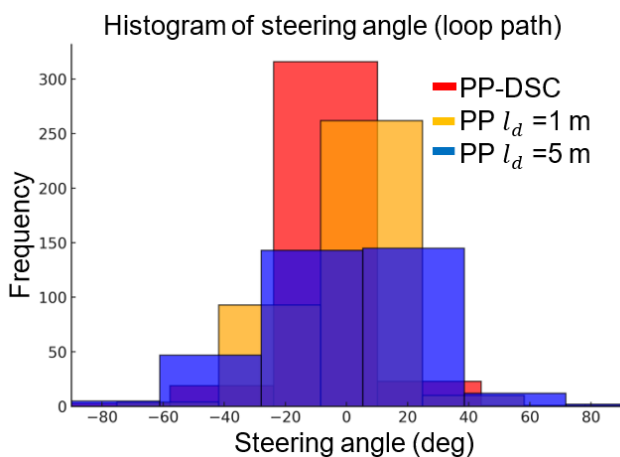

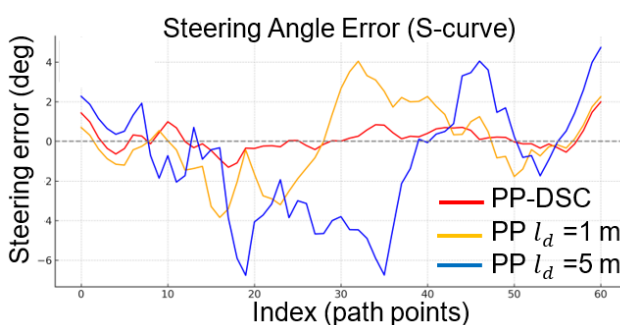**Figure 15** Steering angle histogram during loop tracking.

Figure 16 Steering angle error on the S-curve path.

For the S-curve path, steering angle error was analyzed over the entire trajectory to capture how the controller handled varying curvature (Figure 16). The robot's actual steering tracked the reference line steadily, with deviations staying mostly within ±3 degrees. The 1 m lookahead followed the same trend with only minor fluctuations.

On the other hand, the 5 m case produced larger swings, with peaks reaching up to ±6 degrees at curve transitions. This indicates that shorter lookahead distances tend to produce more stable and accurate steering, especially when the path includes frequent changes in direction.

After running the different tests, there are some differences in how well each method worked. It seems that the path-following got more accurate overall when the robot could change its speed and lookahead distance, like with the PP-DSC method. This was true whether the robot was moving along a straight line, weaving through an S-curve, or circling around a loop in Table 3.

Take the straight-line case first. Here, PP-DSC mean tracking error was 0.007 m, and the RMSE was 0.008 m. That's pretty tight tracking. Pure Pursuit, with a fixed lookahead of 1 m, was fairly close in terms of mean error, though its RMSE was a bit higher at 0.011 m. When the lookahead jumped to 5 m, the mean error increased to 0.010 m. Although the RMSE for that setting matched PP-DSC, the higher mean error might point to some drift or bias over time.

Things changed a bit when the robot followed a curvier path, like the S-curve. PP-DSC still gave better results: a mean error of 0.006 m and RMSE of 0.015 m. With a 1 m lookahead, Pure Pursuit had a negative mean error and the highest RMSE, at 0.021 m. It's interesting because a negative mean doesn't always mean better performance it can just mean errors are in the opposite direction. For the 5 m lookahead, The mean error was back up to 0.010 m, and the RMSE went even higher.

On the loop, PP-DSC mean error was close to zero, at -0.001 m, and RMSE was 0.019 m. Both fixed lookahead options did not quite match up, with either higher mean errors or higher RMSE, or sometimes both. These little gaps can matter, especially when you want the robot to follow a path as closely as possible.

One thing that stands out is that adjusting both speed and lookahead makes a real difference, especially on more complicated paths. When the robot's path curves or changes direction suddenly, it helps if the control algorithm can respond right away, instead of sticking to a single rule for all situations. The fixed lookahead strategies sometimes let errors build up, which is clear when you look at the bigger standard deviations or RMSE values.

Looking beyond the mean, you can see that RMSE and standard deviation tell more of the story. A low mean error could just result from errors canceling each other out, but a high RMSE suggests that big deviations are still happening. In these trials, PP-DSC generally kept both numbers lower, so the path-following was not only more centered, but also less erratic.

These results make a good case for using adaptive algorithms like PP-DSC for robots, especially

outdoors or in places where the route is unpredictable. This method seems to help the robot handle changes more smoothly and keep the tracking tight, which could be really valuable in real-world applications. There's still room to try these methods under even tougher conditions, but from what's here, the benefits of a flexible approach are already pretty clear.

CONCLUSIONS

In this work, the study set out to solve some persistent issues with path tracking for field robots, especially when GPS readings are not always stable. The approach used, called PP-DSC, is pretty straightforward. The main idea is to have the robot slow down when it needs to turn more sharply, rather than using the same speed everywhere. The study wanted to see if this would help, especially when GNSS-RTK alone isn't enough to keep the robot perfectly on track The proposed method was experimentally evaluated on three types of paths using a four-wheeled robot platform. The tracking error was very low for straight lines, with an RMSE of about 0.9 cm. On the S-curve, the error was higher at 2.1 cm, while on the loop path, RMSE reached 1.9 cm. For comparison, the regular Pure Pursuit algorithm with a 1 m fixed lookahead produced an RMSE of about 2.7 cm, highlighting the improvement achieved by the proposed method. PP-DSC worked because it automatically reduced speed as the steering angle increased. This allowed the control system more time to respond when the robot needed to turn sharply.

One thing that helped a lot was sensor fusion using an EKF. By combining GNSS-RTK, IMU, and wheel encoder data, the robot was able to keep a steady estimate of its position, even when the satellite signal wasn't great. This reliability is beneficial in real farming, where losing GPS for a few seconds can easily happen.

The significance of this precision is not merely theoretical; precision matters greatly for farming jobs. You don't want to overlap or miss spots if you're spraying. For planting, you need accurate spacing. When harvesting, the machine has to move carefully between rows or trees to avoid damaging the crops. An additional advantage of the proposed solution is that it works on regular computers and does not require expensive hardware. This means smaller farms could afford to use robots like this, not just large industrial farms.

Some challenges were encountered during the experiments. The optimal speed thresholds were determined through iterative testing and may require further tuning when applied to rougher terrain or muddy field conditions. The experiments were primarily conducted on flat terrain, and weather effects were not explicitly considered in this study. Also, the robot was not loaded with extra equipment. Adding tools for spraying, planting, or harvesting will change how it moves, so future tests should include that.

Several aspects remain for future work. Testing on real farms with different soil types and crops is important because corn fields and orchards present very different challenges. Soil itself can make a big difference, too, as loose sand is not the same as sticky clay. In the future, it might be possible to use machine learning to adjust parameters automatically or to use cameras to help the robot see and follow crop rows more precisely. Future research will also extend the comparison to other path-tracking controllers such as Stanley and MPC to benchmark the proposed method further and validate its advantages under more diverse control frameworks. Ultimately, it will be important to get feedback from farmers to see if the system is safe and practical to use at normal working speeds.

To sum up, making farm robots practical is more important than perfecting them. Farmers need reliable, affordable automation that supports routine agricultural operations. The results show that with some simple changes to a well-known algorithm, path-tracking performance can be significantly improved, even without top-level GPS or high-speed computers. As farm work gets more complex and labor shortages increase, this solution will become more valuable.

DECLARATION OF AI AND AI-ASSISTED TECHNOLOGIES IN THE WRITING PROCESS

The authors utilized ChatGPT-5 pro and Claude Opus 4.1 to improve the academic tone and language clarity of the manuscript during its preparation. All content was critically reviewed and edited by the authors, who assume full responsibility.

ACKNOWLEDGEMENT

REFERENCES

1. Radočaj D, Plaščak I, Jurišić M. Global navigation satellite systems as state-of-the-art solutions in precision agriculture: A review of studies indexed in the web of science. Agriculture. 2023;13:1417.

2. SIZA Robotics. SIZA Robotics launches autonomous robot for vegetable and beet crops. Future Farming; 2024.

3. Moeller R, Deemyad T, Sebastian A. Autonomous navigation of an agricultural robot using RTK GPS and pixhawk. In: Proceedings of 2020 Intermountain Engineering, Technology and Computing; IETC; 2020.

4. Advanced Navigation. Autonomous Agriculture, Precision Farming & Robotics. 2025.

5. Wang Q, Zhang Q, Rovira-Más F, Tian L. Stereovision-based lateral offset measurement for vehicle navigation in cultivated stubble fields. Biosyst Eng. 2023;109:258-65.

6. Ning X, Wang F, Fang J. Sensor Fusion of GNSS and IMU Data for Robust Localization via Smoothed Error State Kalman Filter. Sensors. 2023;23(7):3676.

7. Kaczmarek A, Rohm W, Klingbeil L, Tchórzewski J. Experimental 2D extended Kalman filter sensor fusion for low-cost GNSS/IMU/Odoms precise positioning system. Measurement. 2022;193:110963.

8. Zhang A, Atia MM. An efficient tuning framework for Kalman filter param optimization using design of experiments and genetic algorithms. NAVIGATION: Journal of the Institute of Navigation. 2020;67(4): 775-93.

9. Moore T, Stouch D. A generalized extended kalman filter implementation for the robot operating system. In: Intelligent Autonomous Systems 13: Proceedings of the 13th International Conference IAS-13; 2015 Sep 3; Cham: Springer International Publishing; 2015. p. 335-48.

10. Liu Y, Jiang Y. Motion planning of differential driven robot based on tracking. Control Decis. 2023;38:2529-36.

11. Dorigo M, Birattari M, Stutzle T. Ant colony optimization. IEEE computational intelligence magazine. 2007;1(4):28-39.

12. Yang XS. Nature-inspired metaheuristic algorithms. Luniver press; 2010.

13. Promkaew N, Thammawiset S, Srisan P, Sanitchon P, Tummawai T, Sukpancharoen S. Development of metaheuristic algorithms for efficient path planning of autonomous mobile robots in indoor environments. Results in Engineering. 2024;22: 102280.

14. Coulter RC. Implementation of the pure pursuit path tracking algorithm. 1992.

15. Samuel M, Hussein M, Mohamad MB. A review of some pure-pursuit based path tracking techniques for control of autonomous vehicle. Int J Comput Appl. 2016;135(1):35-8.

16. Baltazar JD, Coelho AL, Valente DS, Queiroz DM, Villar FM. Development of a Robotic Platform with Autonomous Navigation System for Agriculture. AgriEngineering. 2024;6(3).

17. Wang L, Chen Z, Zhu W. An improved pure pursuit path tracking control method based on heading error rate. Industrial Robot: the international journal of robotics research and application. 2022; 49(5):973-80.

18. Jiang X, Kuroiwa T, Cao Y, Sun L, Zhang H, Kawaguchi T, et al. Enhanced Pure Pursuit Path Tracking Algorithm for Mobile Robots Optimized by NSGA-II with High-Precision GNSS Navigation. Sensors. 2025;25(3):745.

19. Ge LI, Yu WA, Liufen GU, Junhua TO. Improved pure pursuit algorithm for rice transplanter path tracking. Nongye Jixie Xuebao/Transactions of the Chinese Society of Agricultural Machinery. 2018;49(5).

20. Xu L, Yang Y, Chen Q, Fu F, Yang B, Yao L. Path tracking of a 4WIS-4WID agricultural machinery based on variable look-ahead distance. Applied sciences. 2022;12(17):8651.

21. Zhao S, Zhao G, He Y, Diao Z, He Z, Cui Y, et al. Biomimetic adaptive pure pursuit control for robot path tracking inspired by natural motion constraints. Biomimetics. 2024;9(1):41.

22. Ding H, Liu H, Zhuang Y, Kan M, Xia D, Ding S. Multi-robot path planning based on four-wheel differential speed model. Control Eng China. 2023;30:730-8.

23. Rajamani R. Vehicle dynamics and control. Boston, MA: Springer US; 2006.

24. Carpio RF, Potena C, Maiolini J, Ulivi G, Rosselló NB, Garone E, et al. A navigation architecture for ackermann vehicles in precision farming. IEEE Robotics and Automation Letters. 2020;5(2): 1103-10.

25. Lei C, Li J, Deng Y, Tan X. RRT* ASV: Improved RRT* path planning method for Ackermann steering vehicles. Expert Systems with Applications. 2025;279:127349.

26. Yan J, Zhang W, Liu Y, Pan W, Hou X, Liu Z. Autonomous trajectory tracking control method for an agricultural robotic vehicle. International Journal of Agricultural and Biological Engineering. 2024;17(1):215-24.

27. Mahmud MS, Abidin MS, Mohamed Z, Abd Rahman MK, Iida M. Multi-objective path planner for an agricultural mobile robot in a virtual greenhouse environment. Comput Electron Agric. 2019;157:488-99.

28. Kiani F, Seyyedabbasi A, Nematzadeh S, Candan F, Çevik T, Anka FA, et al. Adaptive metaheuristic-based methods for autonomous robot path planning: sustainable agricultural applications. Applied Sciences. 2022;12(3):943.